CORRELATION AND COHERENCE

IN QUANTUM-DOT CELLULAR AUTOMATA

A Dissertation

Submitted to the Graduate School

of the University of Notre Dame

in Partial Fulfillment of the Requirements

for the Degree of

Doctor of Philosophy

by

Géza Tóth, M. S.

_____

Prof. Craig S. Lent, Director

Department of Electrical Engineering

Notre Dame, Indiana

July 2000

CORRELATION AND COHERENCE IN QUANTUM-DOT CELLULAR AUTOMATA

Abstract

by

Géza Tóth

In this thesis we investigate the role of correlation and coherence in two possible realizations of Quantum-dot Cellular Automata (QCA): realizations as a semiconductor multi-quantum-dot structure and as a metal-island single electron tunneling circuit. The two are different from the point of view of the underlying physics. The metal island circuits are very strongly connected to the heat bath and they can be modeled semiclassically, using classical quantities such as charging energy and capacitance. To model the semiconductor realization, a quantum mechanical treatment is necessary. The quantum mechanical state of the cells evolves coherently, at least for time scales smaller than the decoherence time. In the first part of the thesis the theory of metal island circuits is used to design a cell structure permitting adiabatic clocking. It is also used to analyze the conductance suppression of coupled double-dots and reproduce the corresponding experimental results from the theory by modeling coherent electron motion inside the QCA cell. In the second part the semiconductor QCA realization is studied. Using Hartree-Fock approximation the basic phenomena in the one dimensional QCA array (large and small amplitude polarization wave propagation and collision) is investigated.

The approach is also used to define Quantum Cellular Neural Networks. In the last part of the thesis intermediate approximations are constructed between the Hartree-Fock and the exact model. An alternative of the density matrix description, the coherence vector formalism is reviewed and used to investigate possibility of quantum computing with QCA. Using the coherence vector formalism as a basis an approximation is presented that includes all two-point correlations while neglects the higher order correlations. Another approach is shown for improving the self-consistent Hartree-Fock model for a majority gate by including correlation effects. The method fixes the qualitatively wrong results obtained if the length of the input legs are very different.

TABLE OF CONTENTS

LIST OF TABLES

LIST OF FIGURES

ACKNOLEDGEMENTS

I would like to thank my advisor, Prof. Craig S. Lent, for his steady help and support in my work. It was distinguished pleasure to learn from and collaborate with Dr. I. Amlani, Prof. I. Bigi, Dr. E. Cannon, Dr. I. Daruka, Prof. G. J. Iafrate, Dr. A. Orlov, Prof. W. Porod, Dr. J. Reynolds, Prof. G. L. Snider, and J. Timler. I am also grateful to Prof. Á. Csurgay and his wife, I. Csurgay for thoughtful discussions and for their support during the past years. I benefited a lot from the research and collaboration done in the group lead by Prof. Roska at the Analogical and Neural Computing Systems Laboratory.* I thank D. Sc. A. G. Radványi, from whom I got my first serious research problem when I worked on my Master's thesis under his supervision. I am indebted to Dr. T. Szirányi, D. Sc. P. Szolgay, Dr. M. Csapodi, P. Földesi, Dr. L. Kék, K. Keserû, K. László, Dr. L. Nemes, Dr. Cs. Rekeczky, and I. Szatmári for the professional experience I gained from them, and for their support. My work was also helped much by the immense love and sacrifice of my parents.

CHAPTER 1

INTRODUCTION

The Quantum-dot Cellular Automata is a new transistorless computing paradigm at the nanoscale. Its three fundamental realizations, the metal island, the semiconductor and the molecular implementations are different from the point of view of coherence and correlation. *Coherence* means that the quantum mechanical system evolves according to the Schrödinger wave equation. *Decoherence*, on the contrary, denotes the case where the time evolution deviates from the wave equation. The *correlation* of A and B, in general, can be given as

$$C = \langle AB \rangle - \langle A \rangle \langle B \rangle, \tag{1.1}$$

where $\langle \ldots \rangle$ denotes the expectation value. C is zero when A and B are *uncorrelated*.

In the classical case of a system which contains two subsystems, the correlation between two dynamical variables of each subsystem is simply a function of these same two dynamical variables. If the time evolution of the subsystem dynamical variables are known then their correlation can be computed. In the quantum mechanical case, on the contrary, the correlation of two operators cannot be expressed as a function of the subsystem dynamical variables. Thus when uniting two systems into one, additional degrees of freedom are created by the correlation.

1

If a QCA array is realized with *metal islands (dots) and tunnel junctions*, it is modeled as a classical capacitive system, with the additional property of interdot tunneling. Since the two extra electrons in a QCA cell interact as classical charges, it is not necessary to use a two electron wave function and the Schrödinger equation to describe this system.

In the case of the *semiconductor* implementation, the system must be modelled by the Schrödinger equation. If the cells are isolated from the environment, then the system is fully coherent, and the dynamics of the cells can be modeled by the many-electron Schrödinger equation. Unfortunately, it is not computationally feasible to model more than a couple of cells this way. Approximating the cells as coupled two-state systems and modeling the QCA circuit with a Schrödinger equation and an Ising spin chain-like Hamiltonian raises the size limit to 10-15 cells.

The method that really makes it possible to model large QCA circuits is the *Hartree-Fock approximation*. This approach models the intracellular dynamics quantum mechanically and the intercell Coulombic interactions classically. For a system of N cells, it involves N coupled Schrödinger equations. The number of state variables scales linearly with the system size, in contrast to modeling with a many-body Hamiltonian in which case it scales exponentially. The price of the simpler (smaller) model is less accuracy. A large portion of the error in the Hartree-Fock approximation is introduced by a failure to model the time-dependent dynamics correctly because it does not consider the *intercell correlations*.

Our goal is to create an intermediate approximation between the Hartree-Fock approximation and the exact model. To do that, the *coherence vector formalism* seems to be ideal. In this approach, the dynamics of the coherence vector of each cell (i.e., the "state" of the individual cells) and their intercell correlation matrices are given by differential equations. The differential equations have a hierarchical system that can be truncated keeping correlation terms up to a certain order. Truncating at the level of the two-point correlations leads to the Hartree-Fock approximation. Truncating at the level of the three-point correlations leads to an intermediate approximation between the Hartree-Fock and the exact method.

Other possible intermediate model could be a hybrid method between modeling by a many-body Hamiltonian and the Hartree-Fock intercellular approximation. The regions where the correlations are important can be modeled by the Schrödinger equation with a many-body Hamiltonian while the rest can be modeled by Hartree-Fock.

In the case of semiconductor realization, the system evolves according to the Schrödinger equation only in special circumstances. In general, there is always some connection to the environment. While the Schrödinger equation fails, the description of the *dissipative* case is also possible with the coherence vector formalism, by including further dissipative terms in the dynamical equations.

Chapter 2 reviews QCA briefly. In Chapter 3 the metal-island QCA implementation is discussed. It is explained how adiabatic switching can be realized with metal island cells. Concerning the *conductance suppression* in

couple double dots, a master equation approach is shown that can be used for modeling correlated electron motion in QCA cells in the finite temperature regime. In Chapter 4 the semiconductor realization is investigated. Beside the exact method using the many-body Hamiltonian, a model based on the Hartree-Fock (or mean-field type) intercellular approximation is presented. It is used to study fundamental phenomena in a one-dimensional array of QCA cells. It is also used to derive the differential equation of the Quantum Cellular Neural Networks (QCNN). The Hartree-Fock approximation neglects the intercellular correlations. In Chapter 5 a model is presented (the coherence vector formalism) that explicitly contains the so far neglected correlation terms. It is used to investigate the possibility of quantum computing with QCA. Chapter 6 is about the realization of an intermediate approximation between the Hartree-Fock and the exact model. Based on the coherence vector formalism, a model is introduced neglecting third and higher order correlations. By keeping the two-point correlations, its results are closer to the exact method than that of the Hartree-Fock model's. In the second subsection of Chapter 6 a particular example, the majority gate with unequal input legs, is shown, where leaving out correlations leads to qualitatively wrong results. A method is shown how incorporate in the model the correlations which are important from the point of view of the dynamics.

CHAPTER 2

REVIEW OF QUANTUM-DOT CELLULAR AUTOMATA (QCA)

In recent years the development of integrated circuits has been essentially based on scaling down, that is, increasing the element density on the wafer. Scaling down of CMOS circuits, however, has its limits. Above a certain element density various physical phenomena, including quantum effects, conspire to make transistor operation difficult if not impossible. If a new technology is to be created for devices of nanometer scale, new design principles are necessary. One promising approach is to move to a transistor-less cellular architecture based on interacting quantum dots, Quantum-dot Cellular Automata (QCA, [1-5]).

The QCA paradigm arose in the context of semiconductor quantum dots, usually formed by using metallic gates to further confine a two-dimensional electron gas in a heterostructure. The quantum dots so formed exhibit quantum confinement effects and well separated single-particle eigenstates. The QCA cell consists of four (or five) such dots arranged in a square pattern. The semiconductor implementation has significant advantages in that both the geometry of the dots and the barrier-heights between the dots can be tuned by adjusting gate potentials. QCA switching involves electrons tunneling through interdot barriers to reconfigure charge in the cell. Information is encoded in the arrangement of charge within the cell.

2.1 Semiconductor Quantum-dot Cellular Automata

The semiconductor Quantum-dot Cellular Automata(QCA[1-8]) cell consists of four quantum dots as shown in Fig. 2.1(a). Tunneling is possible between the neighboring dots as denoted by lines in the picture. Due to Coulombic repulsion the two electrons occupy antipodal sites as shown in Fig. 2.1(b). These two states correspond to polarization +1 and -1, respectively, with intermediate polarization interpolating between the two.

In Fig. 2.1(c) a two cell arrangement is shown to illustrate the cell-to-cell interaction. Cell 1 is a driver cell whose polarization takes the range -1 to 1. It is also shown, how the polarization of cell 2 changes for different values of the driver cell polarization. It can be seen, that even if the polarization of the driver cell 1 is changing gradually from -1 to +1, the polarization of cell 2 changes abruptly from -1 to +1. This *nonlinearity* is also present in digital circuits where it helps to correct deviations in signal level: even if the input of a logical gate is slightly out of the range of valid "0" and "1" voltage levels, the output will be correct. In the case of the QCA cells it causes that cell 2 will be saturated (with polarization close to -1 or +1) even if cell 1 was far from saturation.

A one-dimensional array of cells[3] can be used to transfer the polarization of the driver at one end of the cell line to the other end of the line. Thus the cell line plays the role of the wire in QCA circuits. Moreover, any logical gates (majority gate, AND, OR) can also be implemented, and using these as basic building elements, any logical circuits can be realized[4].
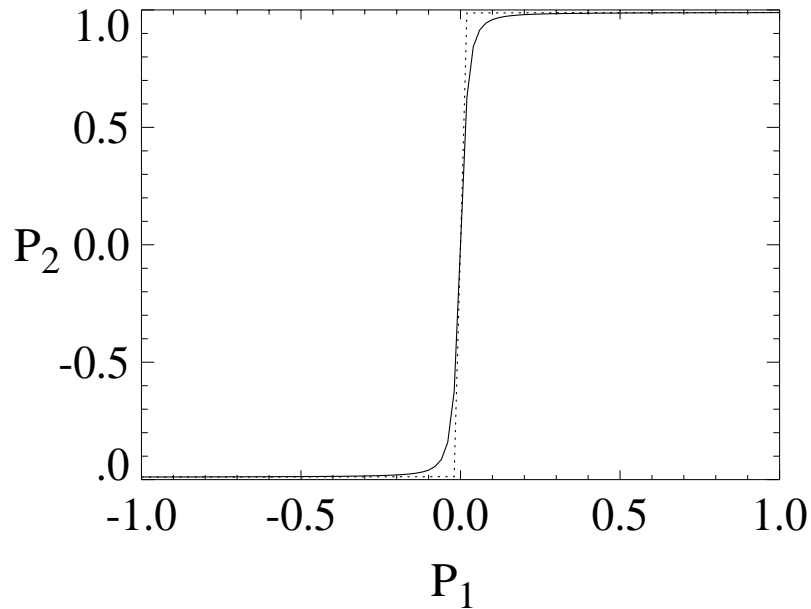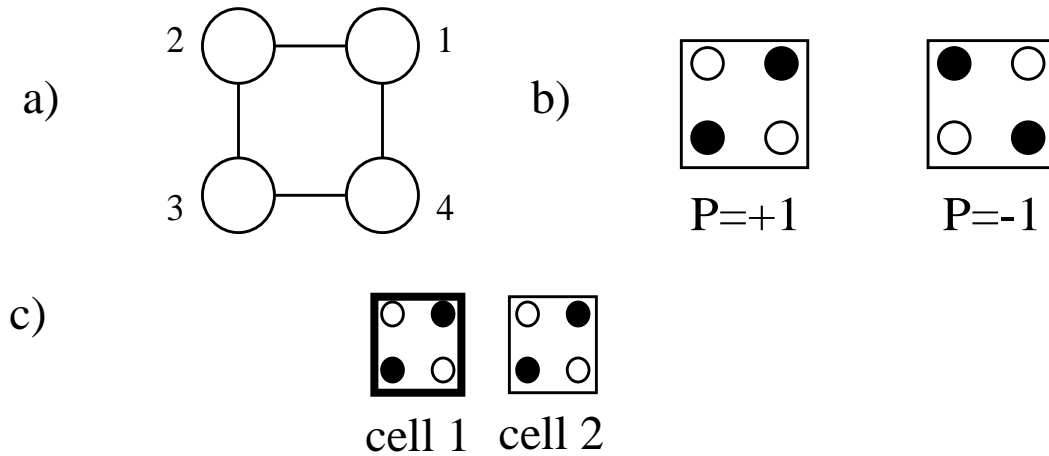
FIGURE 2.1.   Schematic of the basic four-site semiconductor QCA cell. (a) The geometry of the cell. The tunneling energy between two sites (quantum dots) is determined by the heights of the potential barrier between them. (b) Coulombic repulsion causes the two electrons to occupy antipodal sites within the cell. These two bistable states result in cell polarization of P=+1 and P=-1. (c) Nonlinear cell-to-cell response function of the basic four-site cells. Cell 1 is a driver cell with fixed charge density. In equilibrium the polarization of cell 2 is determined by the polarization of cell 1. The plot shows the polarization P_2 induced in cell 2 by the polarization of its neighbor, P_1. The solid line corresponds to antiparallel spins, and the dotted line to parallel spins. The two are nearly degenerate especially for significantly large values of P_1.

2.2 Adiabatic switching with semiconductor QCA

In this paradigm of ground state computing, the solution of the problem has been mapped onto the ground state of the array. However, if the inputs are switched *abruptly*, it is not guaranteed that the QCA array really settles in the ground state, i.e., in the global energy minimum state. It is also possible, that eventually it settles in a *metastable* state because the trajectory followed by the array during the resulting transient is not well controlled.

This problem can be solved by adiabatic switching [3] of the QCA array, as shown schematically in Fig. 2.2. Adiabatic switching has the following steps: (1) before applying the new input, the height of the interdot barriers is lowered thus the cells have no more two distinct polarization states, P=+1 and P=-1. (2) Then the new input can be given to the
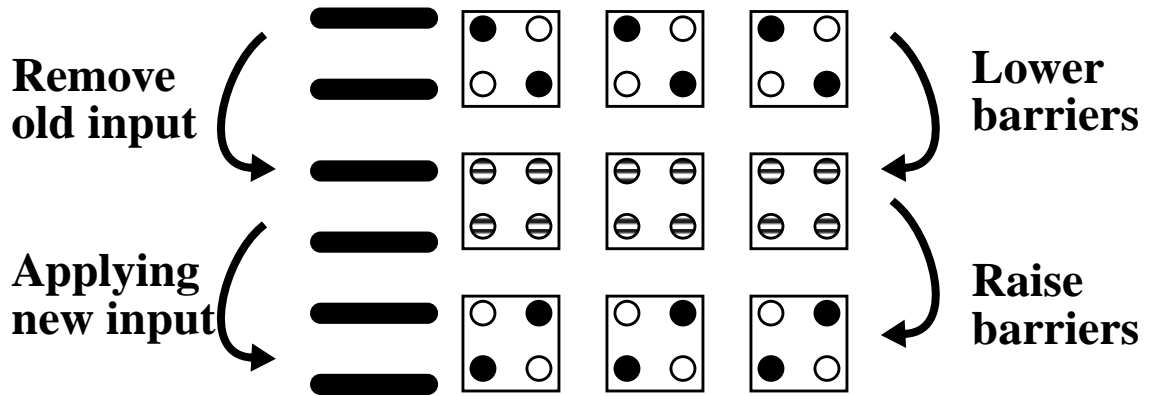
FIGURE 2.2. The steps of the quasi-adiabatic switching are the following: (1) before applying the new input, the height of the interdot barriers are lowered thus the cell have no more two distinct polarization states, P=+1 and P=-1. (2) Then the new input can be given to the array. (3) While raising the barrier height, the QCA array will settle in its new ground state. The adiabaticity of the switching means that the system is very close to its ground state during the whole process. It does not get to an excited state after setting the new input, as it happened in the case of non-adiabatic switching. Since the system does not get to an excited state from the ground state the dissipation decreases a lot.

array. (3) While raising the barrier height, the QCA array will settle in its new ground state. The quasi-adiabaticity of the switching means that the system is very close to its ground state during the whole switching process. It does not reach an excited state after setting the new input, as happens if the input is simply switched abruptly. Since the system does not get to an excited state from the ground state the dissipation to the environment is minimal. On the other hand, to maintain quasi-adiabaticity the time over which the barrier height is modulated must be long compared to the tunneling time through the barrier. Typically a factor of 10 reduces the non-adiabatic dissipation to very small levels.

The previous structure can be used for processing a series of data, as shown in Fig.2.3. While changing the input, the barrier is low therefore the cells do not have a definite polarization. Then the barrier height is increasing, until it reaches the value, where the cell polarization is fixed. This means that the barriers are so high that the interdot tunneling is not possible, the polarization of the cells keeps its value independent of the effects of the external electrostatic fields. At that point the output can be read out. Then the barriers are lowered again, and the next input can be given to the array. Fig. 2.3(c) shows the input and output flow for this case.

a)

Input → QCA Array → Output

Clock signal

b)

Low barriers
No definite cell polarization

High barriers
Fixed cell polarization

Barrier height

Time

c)

Barrier height	H	M	L	M	H	M	L	M	H	M	L

Input	I1	I2	I3	

Output	O1	O2	O3	
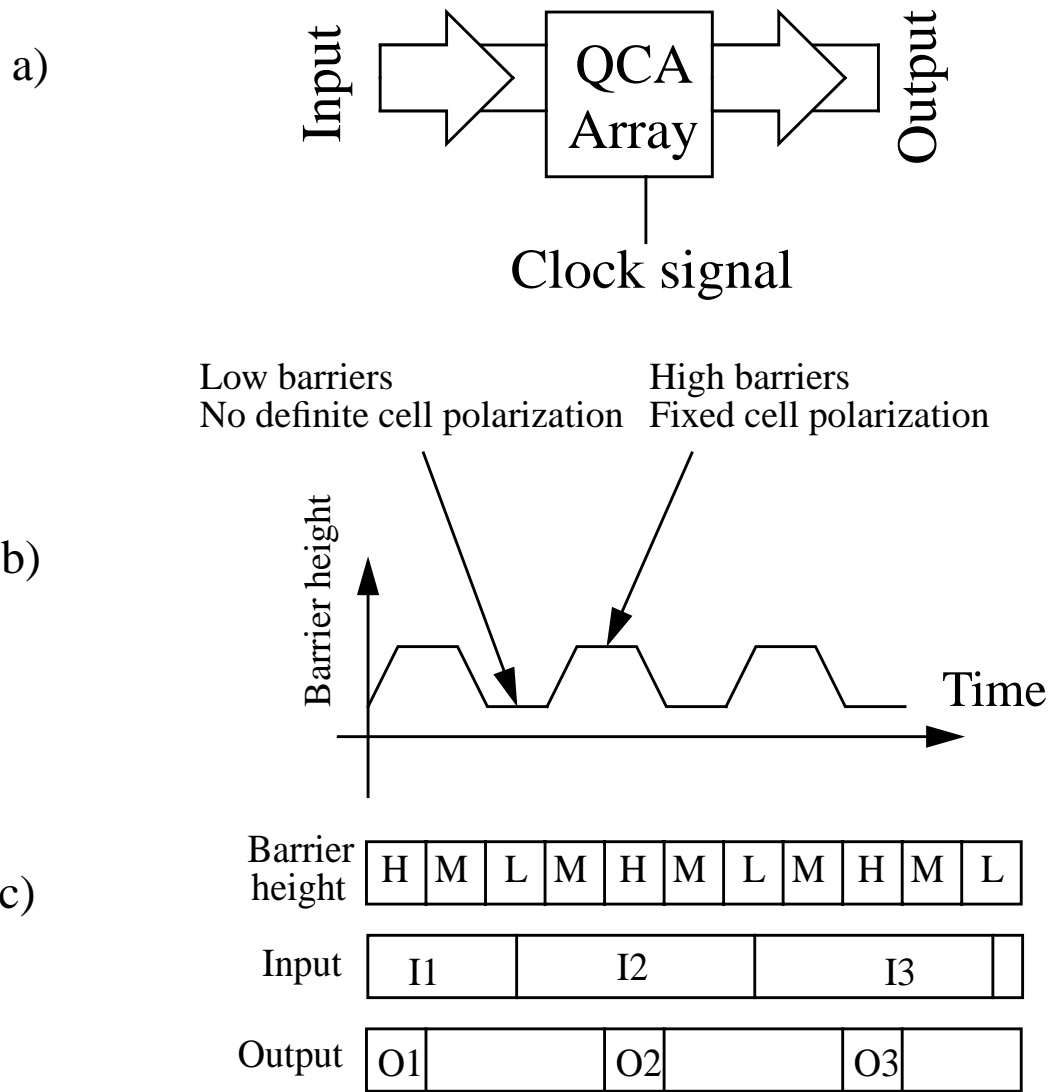
FIGURE 2.3. QCA structure for the processing of data series. (a) The schematic of the structure. (b) The clock signal given to the cells to control their interdot barrier height. (c) The input and output data flow. The new input is given to the array when the barriers are low and the output is read out of the array when the barriers are high, and the polarization of the cells is fixed. (H, M and L stand for 'high', 'medium' and 'low', respectively.)

The cells of such a QCA array have three *operational modes*: if the barriers are low then the cell does not have distinct polarization. This can be called the *null operational mode*. If the barriers are high then the polarization of the cells does not change. This can be called the *locked operational mode*. In case of intermediate barrier heights, the *active mode*, the cells have two distinct polarization states: P=+1 and P=-1, however, external electrostatic field (due to the effects of the neighboring cells) can switch it from one polarization to the other. The operational modes are summarized in Fig. 2.4. Thus the cells periodically go through the null→active→ locked→active→null sequence.

Operational mode	Barrier height	Cell polarization
Active	Medium	Between +1 ⊡ and -1 ⊡
Locked	High	+1 ⊡ or -1 ⊡
Null	Low	Indefinite ⊡

FIGURE 2.4. The three operational modes of the QCA cell in the case of adiabatic switching. In the active mode, the cells have two distinct polarizations: P=+1 and P=-1, and the external electrostatic field can switch cells from one polarization to the other. In the locked mode, the interdot barriers are high therefore the polarization of the cell cannot be switched, it is fixed. In the null mode, the barriers are low thus the cell does not have a definite polarization.

The arrangements shown in Fig. 2.3 can be expanded for more QCA sub-arrays

working in a *pipeline* structure as shown in Fig. 2.5. Now each sub-array reads the output

a)

b)
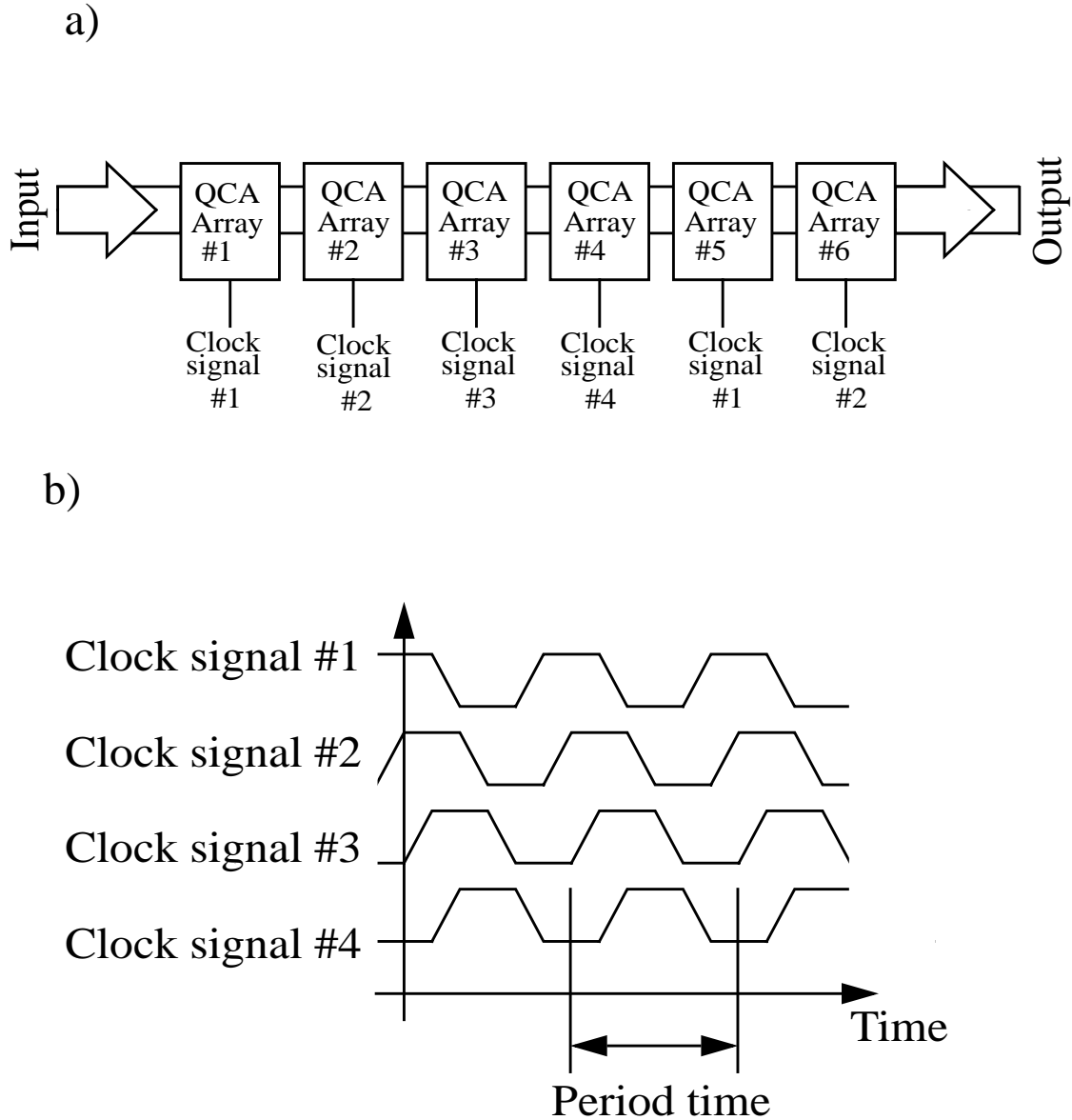
FIGURE 2.5. Pipeline architecture with QCA arrays. (a) All of the arrays get the input from the left neighbor and give the output to the right neighbor. (b) The clock signals used for the control of the interdot barrier height. Each array gets the clock signal delayed by 1/4 period time relative to its left neighbor. Even more sophisticated structures containing logical gates and flip-flops need no more than four different clock signals.

of the left neighbor when the neighbor is in locked state and begins to write into their right neighbor when it is in null state. The main advantage of the pipeline architecture is that the computations with the new input start before the computations with the old input are finished. Each unit gives its subresult to the following unit and then begins to process the subresult of the previous unit. The barrier heights of the arrays are controlled by four different clock signals. The clock signal given to an array is delayed by 1/4 period time relative to the clock signal of its left neighbor. With only these four clock signals, even more sophisticated pipeline structures containing logical gates and flip-flops can be realized [8].

2.3 Metal-island QCA

QCA cells can be also built from metallic tunnel junctions and very small capacitors[5]. There are two main differences between the semiconductor and the metal dot QCA's. (1) Capacitively coupled metal islands are used rather than Coulombically coupled quantum-dots. Unlike the quantum dot, the metal island contains many conduction band electrons. (2) A classical capacitive model can be applied instead of a Schrödinger-equation model.

The only non-classical phenomenon is the tunneling of electrons between metal islands through tunnel junctions. The metal islands have a special feature: they are connected to the other islands through tunnel junctions. If these tunnel junctions were replaced by capacitors the island charge would be zero; however, through the tunnel junction an integer number of electrons can tunnel into or out of the island. Thus the charge of an island is an integer multiple of the elementary charge.

In the case of the metal island cell it is helpful to first consider a double-dot, two of the islands as the basic building element rather than a four dot cell. The two metal islands ("dots") connected by a tunnel junction give a *bistable circuit element* (See Fig. 2.6(a), framed double dot). Depending on the input voltages, the excess electron will show up

Two-island bistable element
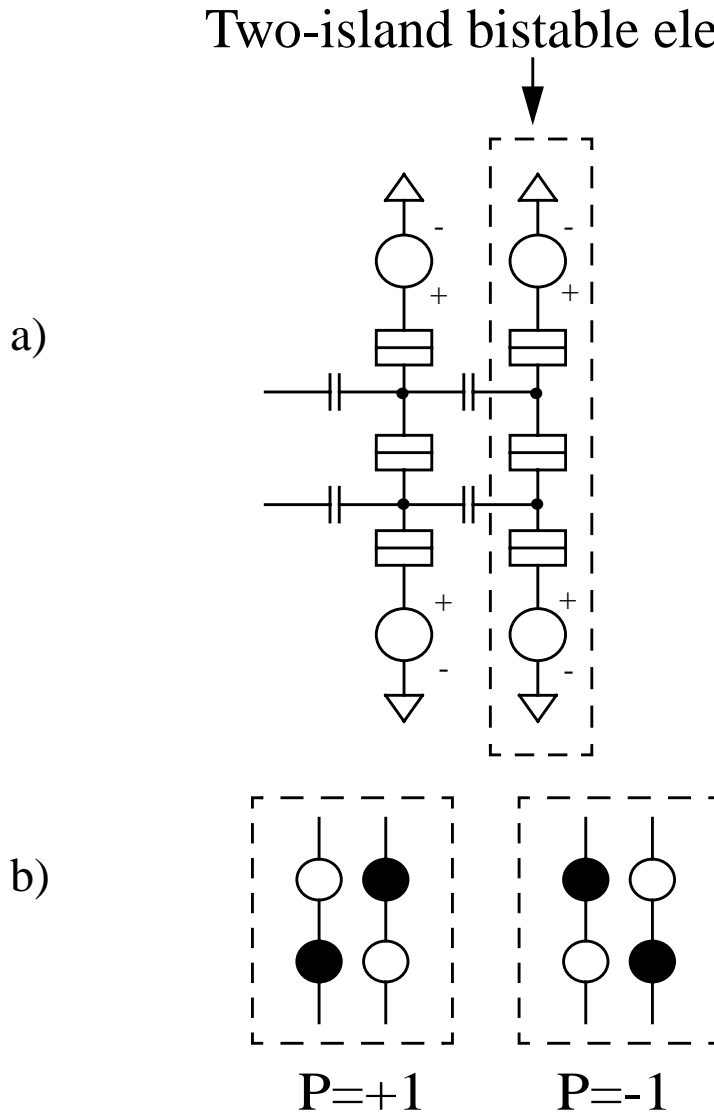
FIGURE 2.6. Metal-island QCA cell. (a) The QCA cell consists of two capacitively coupled bistable elements. Such a bistable element consists of two metal islands. The excess electron can be either in the top or in the bottom island, giving the two possible charge configurations. (b) Symbolic representation of the two possible polarizations of the QCA cell.

either at the upper dot or at the lower dot. By setting the input voltages the occupancy of these dots can be determined, that is, we can set the "polarization" of this bistable element. (Let +1 and -1 denote the two possible polarizations.)

As shown in Fig. 2.6(a), a *QCA cell* consists of two of these bistable elements or *half cells*. It can have two polarizations: +1 if the two excess electrons are in the upper right and lower left islands, -1 if they are in the other two islands (Fig. 2.6(b)). If several of these cells are placed in a line and they are coupled capacitively then by switching the input voltage of the first cell a polarization change will be transmitted along the cell line as in the case of the semiconductor cell. Logical and computational structures which can be implemented with the semiconductor QCA can also be realized with the metal island cells.

CHAPTER 3

QUASI-CLASSICAL QCA DYNAMICS

Quite early in the development of QCA ideas it was realized that the quantization of energy levels in the dots, is not crucial to QCA operation. All that is really required is (approximate) charge quantization on the dot, and quantum-mechanical tunneling to enable switching. The robustness of the QCA scheme is due in large measure to the fact that the information is contained in classical degrees of freedom, while quantum effects simply provide the "grease" that enables switching to occur. It was shown theoretically that in principle, metallic islands connected by capacitive tunnel junctions could also be used to realize QCA cells [5].

The first section of this chapter reviews the theory of metal-island circuits. In the second section quasi-adiabatic switching is implemented with metal-island QCA. The operation of the proposed three-island structure is explained in terms of phase diagrams. The third section analysis the conductance lowering that occurs in the case of coupled double-dots when both are conducting. The correlated electron transport is modelled with master equations.

Unlike the semiconductor quantum-dot QCA, the metal island realization is modelled quasi-classically. The circuits is described in terms of classical notions: charging energy, capacitance, and occupancy. The only non-classical phenomenon is the interdot tunneling. The dynamics are described by master equations instead of the Scrödinger equation. Correlated electron motion takes place in the classical sense as the correlation of dot occupancies.

16

3.1 Theory of metal-island circuits

A metal island system is composed of gate electrodes and metal islands, coupled by tunnel junctions and capacitors. A tunnel junction can be described intuitively best as a "leaky" capacitor which lets electrons tunnel through. A metal island is connected to the environment through only tunnel junctions and capacitors (and not through ohmic resistors) thus its charge is constrained to be (at T=0 K) an integral multiple of the fundamental charge.

The free energy of a configuration can be expressed in terms of the voltages and charges on gate electrodes and metal islands:

$$F = \frac{1}{2} \begin{bmatrix} q \\ q' \end{bmatrix}^T C^{-1} \begin{bmatrix} q \\ q' \end{bmatrix} - v^T q' = E_{electrostatic} - W_{sources}. \qquad (3.1)$$

Here C is the capacitance matrix that describes the structure of the circuit, the v vector gives the voltage of the leads, and q and q' are the island charge vector and the lead charge vector, respectively. The first term of the energy expression describes the electrostatic energy stored in the capacitors and tunnel junctions. The second term is the work done by the sources transferring charge to the leads.

The equilibrium charge configuration for T=0 K temperature minimizes the free energy. For T>0 K, higher energy configurations must also be included in computing thermal expectation values. The measured island charge is then no longer strictly an integer multiple of the elementary charge; it is rather the statistical average of the island charge over accessible configurations.

In modeling tunneling events the *orthodox theory* [15-18] of single electron tunneling was used, and *co-tunneling*[21-22,30-31] was neglected. The dynamics of the

system are governed by the following equation which gives the tunneling rate of an electron in a tunnel junction[20]:

$$\Gamma_{ij} = \frac{1}{e^2 R_T} \times \frac{\Delta F_{ij}}{1 - e^{-\frac{\Delta F_{ij}}{kT}}},$$ (3.2)

where ΔF_{ij} is the difference between the free energy of the initial and final states, and R_T is the tunneling resistance of the junction. In most cases the change in free energy equals the difference of the free energies of the initial and final charge configurations ($\Delta F_{ij}=F_i-F_j$), except for the transitions when the electron enters to or arrives from a voltage source. In these cases $\Delta F_{ij}=F_i-F_j\pm eV_D$, where V_D is the source voltage. The energy eV_D is the work done by the voltage source to raise the potential of an elementary charge from ground to V_D.

If there are no voltage sources connecting through tunnel junction to the circuit (only grounding through tunnel junctions connects the circuit to the environment) then $\Delta F_{ij}=F_i-F_j$ for all the transitions and the tunneling rate depends only on the free energy difference of the initial and final configurations.

The tunneling rates will be used for a *master-equation*[15-17,32] model. The alternative approach would be the Monte Carlo method[41-42]. The master equation method is preferable here since the system is near equilibrium so the number of states (charge configurations) required for modeling is not large. For the master equation model, the accessible charge configurations and the transition rates between them must be known.

The master equation has the form:

$$\frac{dP}{dt} = \Gamma P,$$ (3.3)

where P is the vector containing the probabilities of occurrence of the states and Γ is a matrix describing the state transitions. This equation can be easily solved for the stationary state.

If there are no voltage sources connecting through tunnel junctions to the circuit (for example, V_D is such a voltage source in Fig. 3.1) then the $P_{st,i}$ stationary solutions are given by the Boltzmann distribution:

$$P_{st,\,i} \;=\; \frac{e^{-\frac{F_i}{kT}}}{\displaystyle\sum_k e^{-\frac{F_k}{kT}}}, \tag{3.4}$$

where F_i is the free energy of state i. In this case the current is of course zero.

If the voltages of the generators connecting through tunnel junctions to the circuit are small then the $P_{st,i}$ stationary solutions can be approximated with the probabilities given by the Boltzmann distribution. The results are similar to those obtained from the master-equations. However, the Boltzmann distribution cannot be used to compute the current which is an inherently non-equilibrium phenomenon. Therefore the master equation approach is necessary for conductance computations.

Knowing the probability of occurrence for each state and the transition probabilities, the current through a hypothetical current meter can be computed as

$$I \;=\; e\sum_{i,\,j} c_{ij} P_{st,\,i}\Gamma_{i\to j}, \tag{3.5}$$

where e is the elementary charge, $\Gamma_{i \to j}$ is the transition rate from state i to state j, $P_{st,i}$ is the *ith* element of stationary solution of the (3.3) master equations. The coefficient c_{ij} is zero if the transition from state i to state j does not involve current through the current meter, and it is +1 (-1) if during this transition an electron exits (enters) through the current meter.

The expectation value of a quantity A can be computed as

$$\langle A \rangle = \sum_i P_{st,\,i} A_i, \qquad (3.6)$$

where A_i is the value of the quantity A for the ith charge configuration. If there are no voltage sources connecting through tunnel junctions to the circuit, then the Boltzmann distribution can be used for averaging:

$$\langle A \rangle = \frac{\sum\limits_i e^{-\frac{F_i}{kT}} A_i}{\sum\limits_k e^{-\frac{F_k}{kT}}}. \qquad (3.7)$$

The master equation approach can also be used to compute the average transition rate between two charge configurations, even if there is not a direct transition between them. For example the transition time from state i to state j *(i<j)* can be given in closed form as

$$\langle t_{i \to j} \rangle = r''_j \tilde{\Gamma}^{-2} \begin{bmatrix} 0 & \dots & 0 & \overset{i}{1} & 0 & \dots & 0 \end{bmatrix}^T, \qquad (3.8)$$

where the matrix $\tilde{\Gamma}$ and the row vector r''_j are related to Γ. $\tilde{\Gamma}$ is obtained from Γ omitting its *jth* row and *jth* column. r''_j is obtained from the *jth* row of Γ, leaving out its *jth* element.

In the last part of this section the formula for average transition time from state i to state j ($i<j$) will be deduced. The computations are based on the following model. First all the systems of the ensemble are in state i. Then the ensemble is allowed to evolve according to the master equation describing its behavior. (Discussed later.) Eventually all the systems arrive at state j ($P_j(\infty)=1$). The average transition time can be computed as

$$\langle t_{i \to j} \rangle = \int_0^\infty t \frac{dP_j}{dt} dt,$$
(3.9)

where $\frac{dP_j}{dt} \times \Delta t$ gives the ratio of systems which reach state j during the Δt time interval.

When measuring transition time from state i to state j the systems already arrived in state j should stay in state j and should not leave it. Thus the Γ' coefficient matrix used for average transition time computations is different from the original Γ matrix of the system. It can be obtained from Γ by setting the elements of its *jth* column to zero. (This corresponds to the inhibition of all the transitions from state j.) The master equation with the modified Γ' coefficient matrix is:

$$\frac{dP}{dt} = \Gamma'P.$$
(3.10)

The P solution of this equation can be written in an exponential form. From this solution the $\frac{dP_j}{dt}$ can be expressed and substituted into (3.9); however, the integration cannot be done symbolically because Γ' is not invertible. (To compute the integral given in (3.9) we need the inverse of Γ'.) Thus, before making the steps just mentioned, some additional matrix manipulations are needed to make Γ' invertible.

One way to make Γ' invertible is to eliminate P_j from (3.10). P_j can be easily eliminated because in the *jth* column of the coefficient matrix there are only zeros. The elimination of P_j corresponds to changes in the coefficient matrix and the P vector. The new coefficient matrix, $\tilde{\Gamma}$, is obtained from Γ' omitting its *jth* row and *jth* column. It can be obtained from Γ' as well with the same transformation, because Γ' and $\tilde{\Gamma}$ differ only in the *jth* the column that was just omitted. $\tilde{P}$ is formed by leaving out the *jth* element of P.

After the elimination of P_j the following master equation is obtained:

$$\frac{d\tilde{P}}{dt} = \tilde{\Gamma}\tilde{P}.$$

(3.11)

The initial value of $\tilde{P}$ corresponds to the case when all the systems of the ensemble are in state *i*:

$$\tilde{P}(0) = \begin{bmatrix} 0 & \ldots & 0 & \overset{i}{1} & 0 & \ldots & 0 \end{bmatrix}^T.$$

(3.12)

The time dependence of $\tilde{P}$ can be given as the solution of the (3.11) master equation:

$$\tilde{P}(t) = e^{\tilde{\Gamma}t}\tilde{P}(0) = e^{\tilde{\Gamma}t} \begin{bmatrix} 0 & \ldots & 0 & \overset{i}{1} & 0 & \ldots & 0 \end{bmatrix}^T.$$

(3.13)

For (3.9) we need the time derivative of P_j but (3.11) does not contain it because it was obtained after eliminating P_j. The time derivative of P_j can be found in (3.10). This master equation represents a differential equation system. The *jth* line of the equation system that gives the required time derivative is:

$$\frac{dP_j}{dt} = r'_j P,$$

(3.14)

where r'_j is the *jth* row of Γ'. Knowing that the *jth* element of r'_j is zero (the *jth* column of Γ' is zero) this can be written with $\tilde{P}$ as

$$\frac{dP_j}{dt} = r''_j \tilde{P}, \tag{3.15}$$

where r''_j is the *jth* row of Γ' (and also of Γ) omitting its *jth* element. Substituting first (3.15) and then (3.13) into (3.9), the average transition time from state *i* to state *j* is:

$$\langle t_{i \to j} \rangle = \int_0^\infty tr''_j \tilde{P} dt = r''_j \int_0^\infty t\tilde{P} dt = r''_j \int_0^\infty te^{\tilde{\Gamma}t} dt \begin{bmatrix} 0 & \dots & 0 & 1 & 0 & \dots & 0 \end{bmatrix}^T. \tag{3.16}$$

Using

$$\int_0^\infty te^{-\alpha t} dt = \alpha^{-2}, \tag{3.17}$$

the transition time in a closed form is obtained as (3.8). The right hand side of (3.17) can be computed because $\tilde{\Gamma}$ is invertible. The infinite integral can be evaluated because $\tilde{\Gamma}$ has only negative eigenvalues.

EXAMPLE 3.1

In this example the theory of modelling of the statics and dynamics of metal island circuits will be explained using the example of a double-dot. The circuit under study can be seen in Fig. 3.1. Electrons can tunnel between the voltage source and the top island, between the top and the bottom island, and between the bottom island and the current meter. Both islands are capacitively coupled to external leads. Controlling the V_1 and
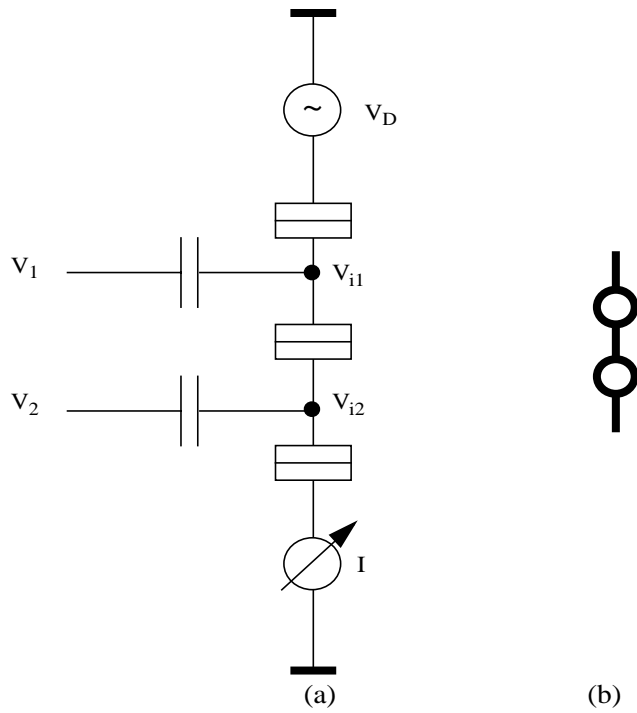
FIGURE 3.1. (a) The double-dot used in these section as an example. (b) Symbolic representation of the double-dot.

V_2 lead voltages, the dot voltage and the occupancy of the dots can be controlled. The more positive the dot voltage, there are more extra electrons on the dot.

Our model involves all the 4 charge configurations having 0 or 1 dot occupancies (00, 01, 10 and 11) and all the possible transitions connecting them. These configurations and transitions are shown in Fig. 3.2. Notice that there is no direct transition between state 3 and state 4. Current flow through the double-dot if an electron exits to or enters from the environment. Gray arrows are indicating the transitions where an electron leaves from or enters to the bottom dot through the current meter.
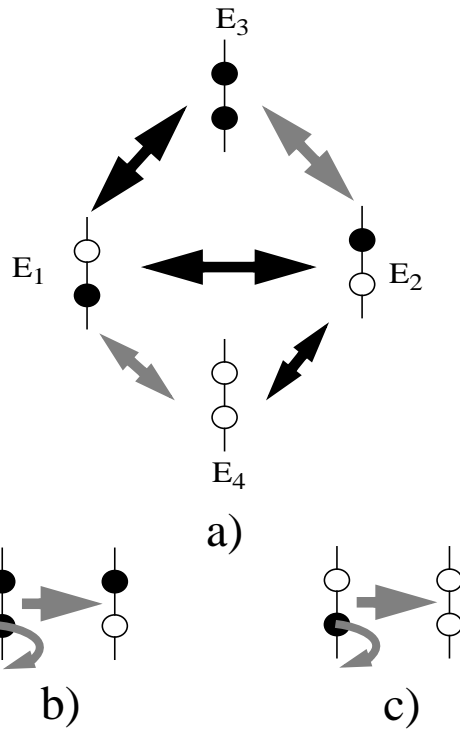
FIGURE 3.2. Transitions between the charge configuration of a double-dot. If the 01 and 10 charge configurations turn into each other directly then current does not occur, however, current flows if these two states turn into each other through the intermediate 11 and 00 states. In these cases an electron leaves the system through the current meter connected to the bottom dot as depicted on (b) and (c).

In modelling the circuit, the first step is to determine the free energy of the four charge configurations. This can be done with (3.1) if we know all the capacitances in the circuit. From the free energies of the charge configurations the Γ_{ij} tunneling rates from one configuration to the other can be computed using (3.2).

The next step is to set up the (3.3) master equation. The P probability vector has four elements corresponding to the four configurations:

$$P = \begin{bmatrix} P_1 & P_2 & P_3 & P_4 \end{bmatrix}^T. \tag{3.18}$$

The coefficient matrix of the master equation can be obtained based on Fig. 3.2 is:

$$\Gamma = \begin{bmatrix} -(\Gamma_{12} + \Gamma_{13} + \Gamma_{14}) & \Gamma_{21} & \Gamma_{31} & \Gamma_{41} \\ \Gamma_{12} & -(\Gamma_{21} + \Gamma_{23} + \Gamma_{24}) & \Gamma_{32} & \Gamma_{42} \\ \Gamma_{13} & \Gamma_{23} & -(\Gamma_{31} + \Gamma_{32}) & 0 \\ \Gamma_{14} & \Gamma_{24} & 0 & -(\Gamma_{41} + \Gamma_{42}) \end{bmatrix}.$$

$$\tag{3.19}$$

Here the Γ_{ij} transitions rates were computed according to (3.2).

The $P_{i,st}$ stationary probabilities can be obtained taking the time derivatives to be zero in (3.3). The following system of four equations can be obtained:

$$\begin{bmatrix} -(\Gamma_{12} + \Gamma_{13} + \Gamma_{14}) & \Gamma_{21} & \Gamma_{31} & \Gamma_{41} \\ \Gamma_{12} & -(\Gamma_{21} + \Gamma_{23} + \Gamma_{24}) & \Gamma_{32} & \Gamma_{42} \\ \Gamma_{13} & \Gamma_{23} & -(\Gamma_{31} + \Gamma_{32}) & 0 \\ \Gamma_{14} & \Gamma_{24} & 0 & -(\Gamma_{41} + \Gamma_{42}) \end{bmatrix} \begin{bmatrix} P_1 \\ P_2 \\ P_3 \\ P_4 \end{bmatrix} = 0. \tag{3.20}$$

Notice that the four lines are not linearly independent since adding them together one obtains zero. An additional constraint is needed:

$$P_1 + P_2 + P_3 + P_4 = 1. \tag{3.21}$$

Replacing the last of the four lines of equation system (3.20) by (3.21) one obtains:

$$\begin{bmatrix} -(\Gamma_{12}+\Gamma_{13}+\Gamma_{14}) & \Gamma_{21} & \Gamma_{31} & \Gamma_{41} \\ \Gamma_{12} & -(\Gamma_{21}+\Gamma_{23}+\Gamma_{24}) & \Gamma_{32} & \Gamma_{42} \\ \Gamma_{13} & \Gamma_{23} & -(\Gamma_{31}+\Gamma_{32}) & 0 \\ 1 & 1 & 1 & 1 \end{bmatrix} \begin{bmatrix} P_1 \\ P_2 \\ P_3 \\ P_4 \end{bmatrix} = \begin{bmatrix} 0 \\ 0 \\ 0 \\ 1 \end{bmatrix}.$$

(3.22)

This can be easily solved for the stationary probabilities since the coefficient matrix is invertible.

After having the stationary probabilities of the four charge configurations, the expression for current must be obtained. Current comes from the transitions when an electron exits (enters) through the current meter. These transitions are summarized in the following table:

Initial state (i)	Final state (j)	c_{ij}
3	2	+1
1	4	+1
2	3	-1
4	1	-1

c_{ij} is zero for all the other transitions. Substituting the c_{ij} values into (3.5) one obtains the current

$$I = \{(\Gamma_{32}P_{3st} - \Gamma_{23}P_{2st}) + (\Gamma_{14}P_{1st} - \Gamma_{41}P_{4st})\}e.$$

(3.23)

The average transition time from state 1 to state 3 can be computed according to (3.8):

27

$$\langle t_{1 \to 2} \rangle = \begin{bmatrix} \Gamma_{12} \\ \Gamma_{32} \\ \Gamma_{42} \end{bmatrix}^T \begin{bmatrix} -(\Gamma_{12} + \Gamma_{13} + \Gamma_{14}) & \Gamma_{31} & \Gamma_{41} \\ \Gamma_{13} & -(\Gamma_{31} + \Gamma_{32}) & 0 \\ \Gamma_{14} & 0 & -(\Gamma_{41} + \Gamma_{42}) \end{bmatrix}^{-2} \begin{bmatrix} 1 \\ 0 \\ 0 \end{bmatrix}.$$

$$(3.24)$$

Next an example will be shown how to compute the expectation value of a quantity. Let us define P_{DD} polarization for the double dot as

$$P_{DD} = N_{top} - N_{bottom}, \qquad (3.25)$$

where N_{top} and N_{bottom} are the occupancies of the top and the bottom dots.

According to (3.6), the expectation value of P_{DD} can be computed as

$$\langle P_{DD} \rangle = \sum_i P_{st,i} P_{DDi} = P_{st,1}(-1) + P_{st,2}(1) + P_{st,3}(0) + P_{st,4}(0).$$

$$(3.26)$$

Here P_{DDi}'s are the polarizations for the four charge configurations. (3.26) leads to

$$\langle P_{DD} \rangle = P_{st,2} - P_{st,1}. \qquad (3.27)$$

3.2 Quasiadiabatic switching with metal-island QCA [9]

The semiconductor QCA implementation has remained the focus of development as the theory has been extended to large arrays of devices and computer architecture questions. A key advance was the realization that by periodically modulating the inter-dot barriers, clocked control of QCA circuitry could be accomplished. The modulation could be done at a rate which is slow compared to inter-dot tunneling times, thereby keeping the switching cells very near the instantaneous ground state. This quasi-adiabatic switching [8] paradigm has proven very fruitful. Quasi-adiabatic clocking permits both logic and addressable memory to be realized within the QCA framework. It allows a pipe-lining of computational operations.

Recently, the first experimental realization of a functioning QCA cell has been reported. This was accomplished in the metal-dot system. The bistable behavior and full cell operation were confirmed. This experimental success raises the question as to whether the quasi-adiabatic switching can be implemented in the metal-dot system. The barriers between dots in this system are typically very thin slices of oxide. While there have been some promising experiments involving the modulation of such barriers[39], in general it is much harder to accomplish than in the semiconductor case. In this section we demonstrate a scheme for quasi-adiabatic switching of metallic QCA cells. The modulated barrier is basically replaced by another dot, whose potential can be altered.

The circuit for the metallic half-cell is shown in Fig. 3.3(a). It contains three metallic islands. The occupancy of the three islands is represented by a triple of integers [n1 n2 n3]. During operation its occupancy can be [100], [010] or [001], as shown in Fig. 3.3(b). The [100] charge configuration corresponds to the polarization +1 case, the [001]

charge configuration corresponds to the polarization -1 case, while [010] represents a null polarization.

The top and bottom islands are biased with respect to ground through (non-leaky) capacitors. The bias voltage raises the electrostatic potential of these islands (lowering electron potential energy) so that an electron is attracted from ground into the three-island chain. The top and bottom islands can be viewed as a double well system with the middle island acting as a controllable barrier.

Each of the three islands has a corresponding gate electrode. A differential input is applied to the gate electrodes for the top and the bottom islands. The half cell can be switched from one polarization state to the other by this input voltage. The input can be supplied externally or from another half-cell (as discussed in the next section). The voltage on the gate electrode for the middle island is used as a control. The three operational modes of the half cell (active, locked and null) can be selected by setting this voltage to one of three discrete levels corresponding to the three modes.

The three operational modes are shown schematically in Fig. 3.4(a-c). The switching in active mode is illustrated in Fig. 3.4(a). First the pictorial representation of the process can be seen, then the energies of the [100], [010] and [001] configurations are given during the switching. The differential input bias changes from positive to negative. Initially, the top electrode is at a positive potential while the bottom electrode is negative resulting in the [100] configuration having the lowest energy. As V decreases, the energy of the [100] configuration increases and will be higher than that of the [010] configuration. Thus the electron tunnels from the top island to the middle island, and the three-island system is in the [010] configuration. Decreasing V further, the [001] will be the minimal
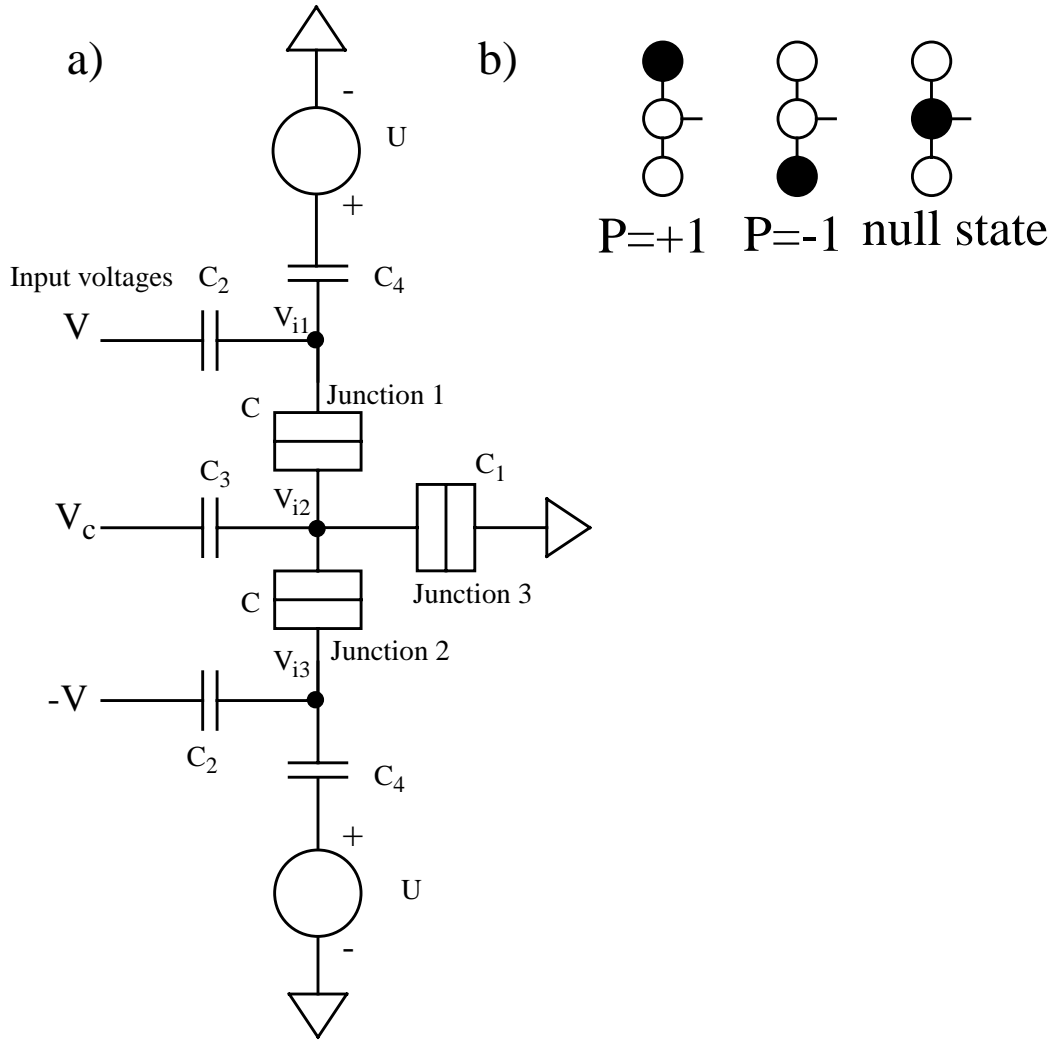
FIGURE 3.3. Metal island half-QCA structure permitting adiabatic switching. (a) The circuit consists of three metal islands connected to each other by tunnel junctions. Each island has a capacitively coupled electrode. Applying the V differential input bias and the Vc control voltage the occupancy of the dots can be determined. The middle island is grounded in order to provide an excess electron in the three island system that is necessary to realize the [100]/[010]/[001] charge configurations. The two voltage sources are used to increase the potential of the top and bottom islands to make the switching more abrupt. (b) The symbolic representation for the three island system. The occupancies corresponding to the P=+1, P=-1 polarizations and the null state (indefinite polarization) are shown.

energy configuration, and therefore the electron tunnels to the bottom island. In Fig. 3.4(b)

the locked operational mode is illustrated. The control electrode has a lower potential

(higher electron potential energy) than in active mode, so the electron cannot get to the

middle island from the top one. In null mode the control electrode is at a higher potential (lower electron potential energy) than in active mode thus the electron stays in the middle island regardless of the applied differential input bias as shown in Fig. 3.4(c). (The approach to quasi-adiabatic switching is similar to that reported in another context by in [19].)

3.2.1 The physical background of the operation

We can model the quasi-static behavior of the circuits described by considering only the energy of the various charge configurations of the system. We treat here only the zero temperature situation. The system is composed of gate electrodes and metal islands, coupled by tunnel junctions and capacitors[15-18]. The gate electrode voltages are fixed by external sources, and the charge on each metal island is constrained to be an integral multiple of the fundamental charge. The electrostatic energy of a configuration can be expressed in terms of the voltages and charges on gate electrodes and metal islands.

$$E = \frac{1}{2} \begin{bmatrix} q \\ q' \end{bmatrix}^T C^{-1} \begin{bmatrix} q \\ q' \end{bmatrix} - v^T q' \qquad (3.28)$$

Here C is the capacitance matrix for the islands and electrodes, v is a column vector of voltages on the gate electrodes, q and q' are the column vectors of the island charges and the lead charges, respectively. The first term of the energy expression describes the electrostatic energy stored in the capacitors and tunnel junctions. The second term is the work done by the sources transferring charge to the leads. The equilibrium charge configuration for T=0 K temperature minimizes this electrostatic energy.

For a QCA cell to be switched quasi-adiabatically, input and clock voltages are varied smoothly enough so that the cell is very close to its equilibrium ground state
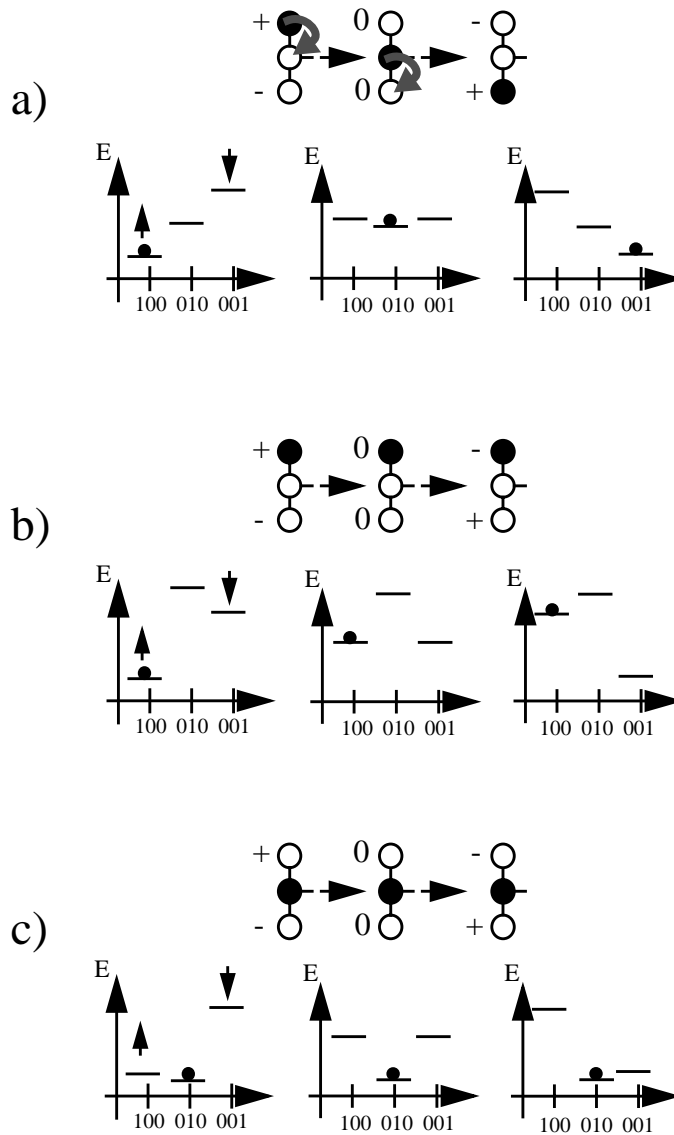
FIGURE 3.4. The three operational modes. (a) Active operational mode. The electron tunnels from the top island to the bottom island through the middle island, if electrode voltages change. First the pictorial representation of this process is shown. '+', '-' and '0' refers to the sign of the electrode voltages. Then the energies of the [100], [010] and [001] charge configurations can be seen during the switching. The dot refers to the charge configuration the system occupies. (b) Locked operational mode. The electron is locked in either the top or the bottom island, because the [010] configuration has much higher energy than the others. (c) Null operational mode. The electron is locked in the middle island, because the [010] configuration has much lower energy then the other two.

configuration during the time it is switching. Thus during the *active* mode of cell operation, the cell should be in the configuration which minimizes the total electrostatic energy for the cell. The same is true for the *null* mode.

The *locked* mode, by contrast, is designed to provide a short-term memory, *i.e.*, the cell configuration is held to what it was in the immediate past so that the locked cell can be used as a fixed input for another cell which is being switched. Thus it is by design not necessarily in the minimum energy configuration but may be in a metastable state. To model this requires knowing not just the minimum energy configuration, but also the allowed transitions between various configurations. For the QCA half-cell, the six basic *allowed transitions* are summarized in Fig. 3.5.
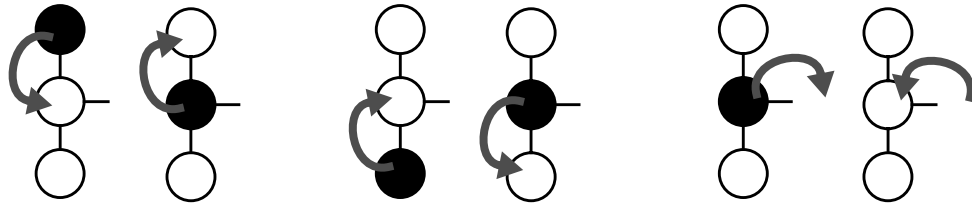
FIGURE 3.5. The six basic tunneling events that can happen in the three-island structure shown in Fig. 3.3

Notice that there is no transition directly from the top island to the bottom island. This is important for the operation of the locked mode. Suppression of this transition is the reason that there is no direct tunneling path between either the top or bottom electrode and ground.

We can treat all these modes using a single modeling algorithm. As the input voltages are changed in small steps, at each step we examine whether an allowed transition could decrease the energy of the system. If so then the tunneling event takes place

instantaneously and the dot occupancies change. This approach is only applicable to the quasi-adiabatic situation we consider here. Refinements which would extend these calculations to high-frequencies would include specific tunneling rates in a Monte Carlo [41-42] or master-equation[15-17,32] approach and would include co-tunnelling[21-22,30-31] rates.

3.2.2 Operational modes

For simulations shown below parameters for capacitors and voltage sources were chosen in the range of practically realizable values for metal islands fabricated with Dolan shadow-evaporation techniques. They are also chosen in the design space to fulfill the requirement for a reasonable range for the input and control voltages. We have performed numerical simulations of the switching of a half-cell using the model described above. The specific parameter values used were: C=420aF, C_1=300aF, C_2=25aF, C_3=80aF, C_4=200aF and U=0.36mV. With this set of parameters the control voltages corresponding to locked, active and null operational modes are V_c = -0.18, 0.18 and 0.68mV, respectively. The input bias changes in the range of -0.3 and +0.3mV.

In Fig. 3.6 the transfer characteristics of this half cell can be seen in active mode, that is, for V_c=0.18mV. It is piecewise linear, and the abrupt change in value and slope is due to tunneling events, thus the nonlinearity of the transfer characteristics comes from the charge quantization on the metal island.

It is instructive to construct a diagram of the system state as a function of the input voltage and V_c. Fig. 3.7 shows the equilibrium ground state "phase diagram" for the system as a function of these two voltages. For the null and active mode, this is sufficient
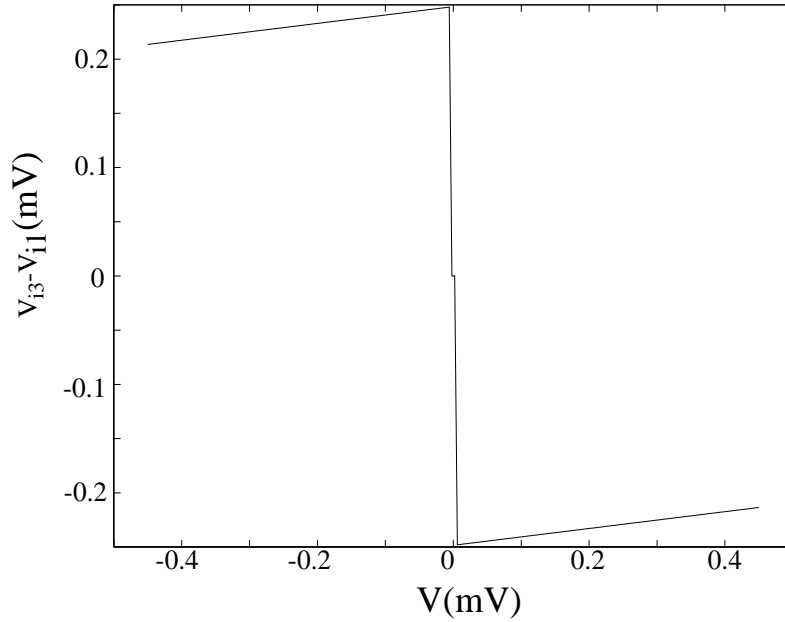
FIGURE 3.6. Transfer characteristics of the half cell structure given in Fig. 3.3 for active mode. It is piecewise linear, and the abrupt change in value and slope are due to tunneling events. In case of a metal island QCA the nonlinearity comes from the charge quantization. Replacing the tunnel junctions with linear capacitors the circuit would also be linear.

information to characterize the switching behavior. However for the locked mode, we must assume a particular starting point. Fig. 3.8 shows this state diagram for the case when the input voltage is increasing from -0.45 mV to +0.45mV. For V_c chosen to keep the system in the locked mode, this means that the system is initially in the [001] state and is kept there. The opposite situation is depicted in Fig. 3.9, where the system starts with a positive input voltage and is thus in the [100] case. The locked mode keeps it there because the [100]$\rightarrow$[001] transition is suppressed.

The three operational modes will be analyzed using the state diagram shown in Fig 3.8. Taking V_c=0.18mV the circuit is in active operational mode. Following the arrow belonging to the 0.18mV level, the change of the charge configurations as V changes from
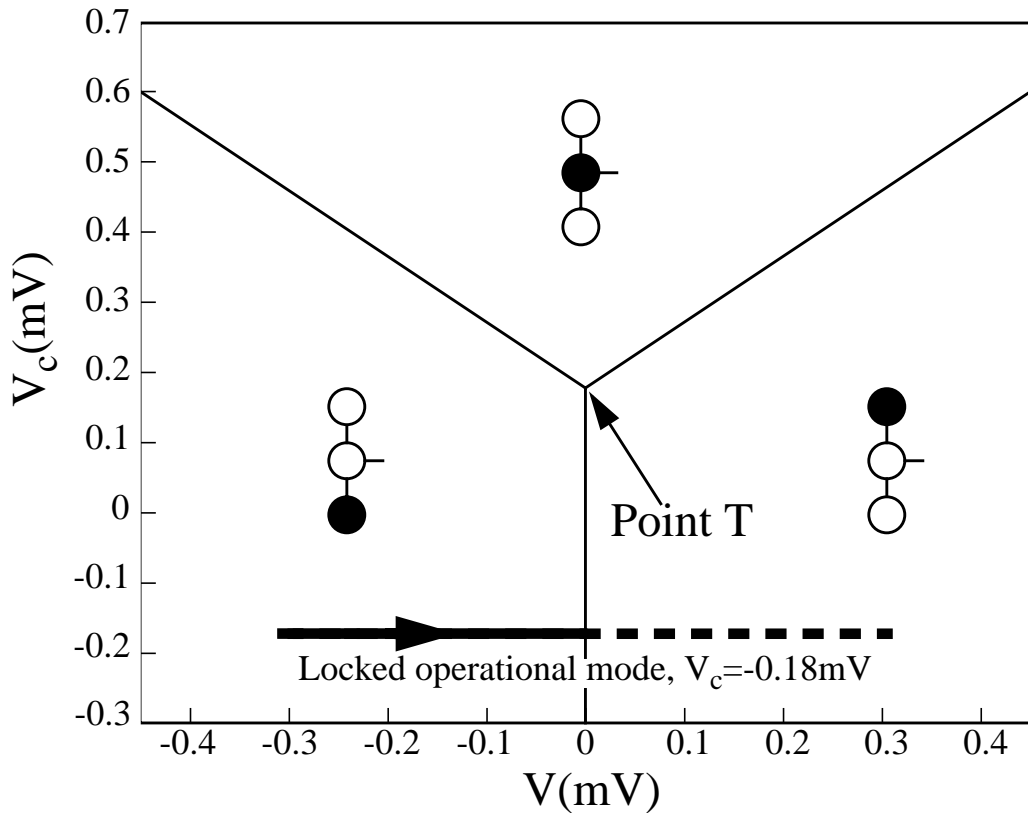
FIGURE 3.7. Phase diagram of the half cell structure permitting adiabatic switching. The minimal energy configuration is shown as a function of the differential input bias V and the control voltage V_c. The control voltage level of the locked operational mode is also shown.

+0.3 to -0.3mV can be read from the graph. The transition series belonging to this case is

[001]→[010]→[100]. The electron tunnels from the third island to the second island, and

then moves further to the first island.

If V_c is decreased to -0.18mV, the potential of the middle electrode also decreases and the

electron from the islands on the sides can not get to the middle island. This is the locked

operational mode, the occupancy does not change even if the V bias voltage is changed, as

can be seen following the bottom arrow in Fig. 3.8.
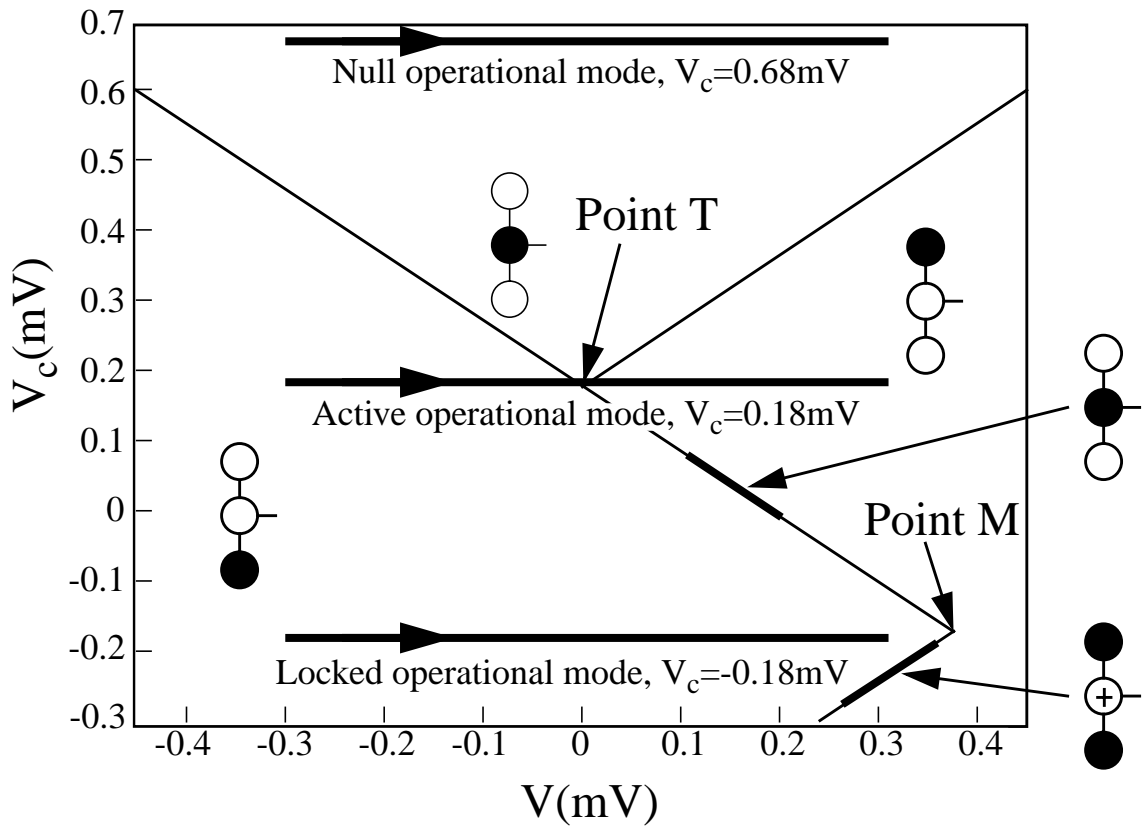
FIGURE 3.8. State diagram of the half cell for switching. It shows the occupancies of the three islands as the V differential input bias *increased* from -0.45 to +0.45mV for a V_c range of -0.3 and 0.7mV. The voltage levels for the three operational modes are also shown. The charge configuration is also given for each region of the diagram. Note, that the [001] and the [100] phases seem to have a common border, but there is a very "thin line" of [010] or [1,-1,1] phase between them. (The direct transition from [001] to [100] is not possible.) The dots with a "+" sign refer to -1 electron on the dot that is an excess positive charge.

If V_c is increased from the value it had in case of active mode to 0.68mV, then the electron will be drawn to the middle island. It will stay there independent of the input voltages, as can be seen if one follows the top arrow in Fig. 3.8. This is the null operational mode.
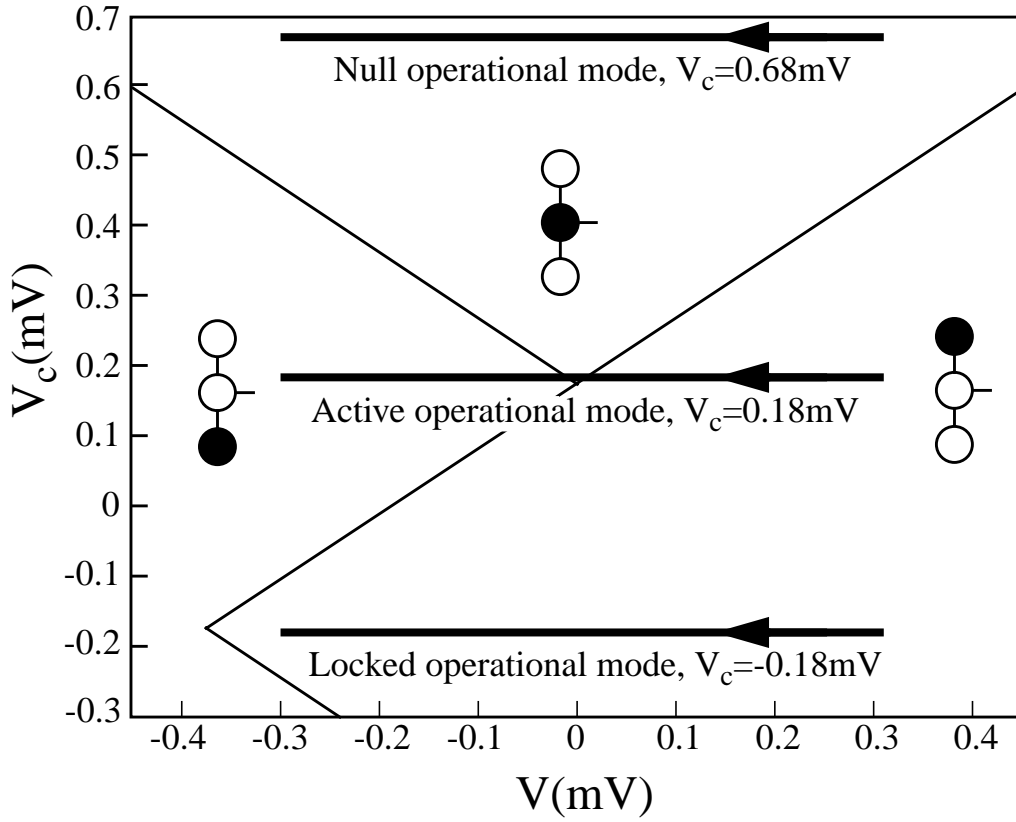
FIGURE 3.9. State diagram of the half cell for switching. The diagram shows the occupancies of the three islands as the V differential input bias *decreased* from +0.45 to -0.45mV for a V_c range of -0.3 and 0.7mV. The voltage levels for the three operational modes are also shown. The charge configuration is also given for each region of the diagram. Comparing with Fig. 3.8, the differences are due that V changes in the opposite direction.

The critical points on these state diagrams are labeled T and M. The values of V and V_c for these points can be given analytically in terms of the circuit parameters. If we let

$X = C + C_2 + C_4$ and $Y = 2C + C_2 + C_3$, then

$$V^T = 0, \qquad (3.29)$$

$$V_c^{\ T} = \frac{e}{2C_3}\left(\frac{\frac{Y}{C}\left(2\frac{UC_4}{e}-1\right)-4\frac{UC_4}{e}+\frac{X}{C}+\frac{C}{X}}{\frac{X}{C}-1}\right), \qquad (3.30)$$

39

$$V^M = \frac{e}{2C_2}\left(\frac{\left(\frac{X}{C}-1\right)^2}{\frac{XY}{C^2}-2}\right), \tag{3.31}$$

$$V_c{}^M = \frac{e}{2C_3}\left(\frac{\frac{Y}{C}\left(2\frac{UC_4}{e}-1\right)-4\frac{UC_4}{e}+2}{\frac{X}{C}-1}\right). \tag{3.32}$$

It is worthwhile to note that for higher V_c values similar graph to Fig. 3.8 could be drawn, except for that the [100], [010] and [001] phases would be replaced by the [110], [020] and [011] phases, respectively. If V_c is increased further, then the [120], [030], phases [021] can be found in the diagram. Thus the only difference in the system behavior for higher (lower) V_c values is that the population of the middle island is increased (decreased) by a constant. In this way it can be said that the system behavior is periodic in V_c, and it is not more informative to draw a graph for a wider range of control voltages. The ΔV_c periodicity of the phase diagram in the V_c direction is:

$$\Delta V_c = \frac{e}{C_3}. \tag{3.33}$$

3.2.3 QCA shift register

We construct a simulation of a cell line acting as a shift register, that is a 1D array of capacitively coupled QCA cells. A QCA cell consists of two half cells as depicted in Fig. 3.10(a). It can have three different occupancies: [001 100] for P=+1 polarization, [100 001] for P=-1 polarization and [010 010] for the null state as shown in Fig. 3.10(b). The adiabatic switching is realized with four different clock signals as it is shown in Fig. 3.11.

Due to these clock signals the operational mode of a half-cell in the line changes periodically: active→locked→active→null.
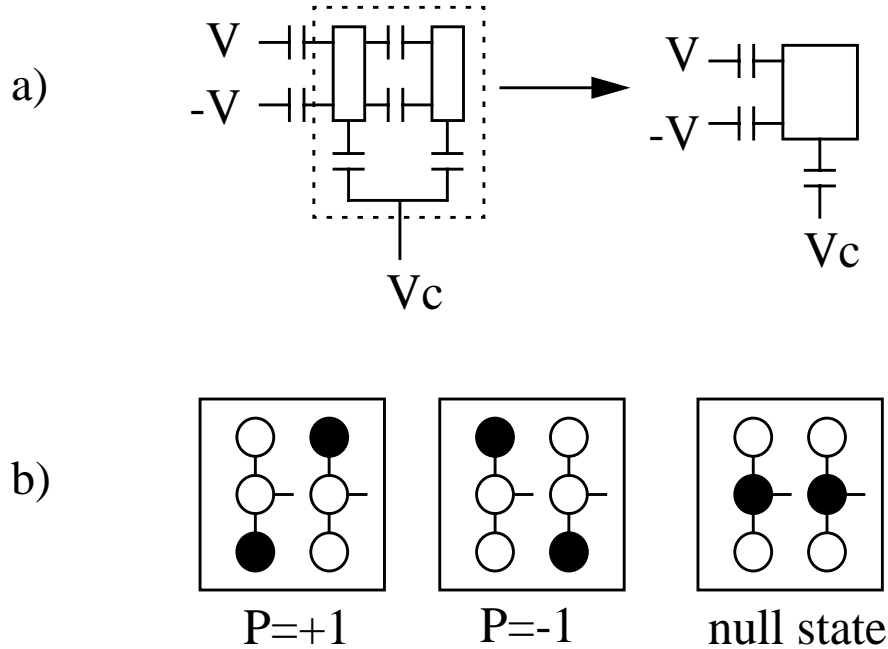
FIGURE 3.10. Metal-dot QCA cell. (a) It consists of two half cells that get the same control voltage. (b) The occupancies corresponding to the P=+1, P=-1 polarizations and the null state.

The operation of a line of four cells can be seen in Fig. 3.11. Each line of the graph shows the polarization of a cell as a function of time. In the figure the parts are framed where the cells are in locked operational mode. The state of the cell can be considered valid only in this state, that is, it is supposed to be read externally only during this time.

The shift register is instructive because in principle each element could be replaced by a more complex computational unit. This is how more sophisticated processing could be achieved in this paradigm. The designs of larger-scale functional units as reviewed in Reference [3] can now just be taken over with this new cell design.
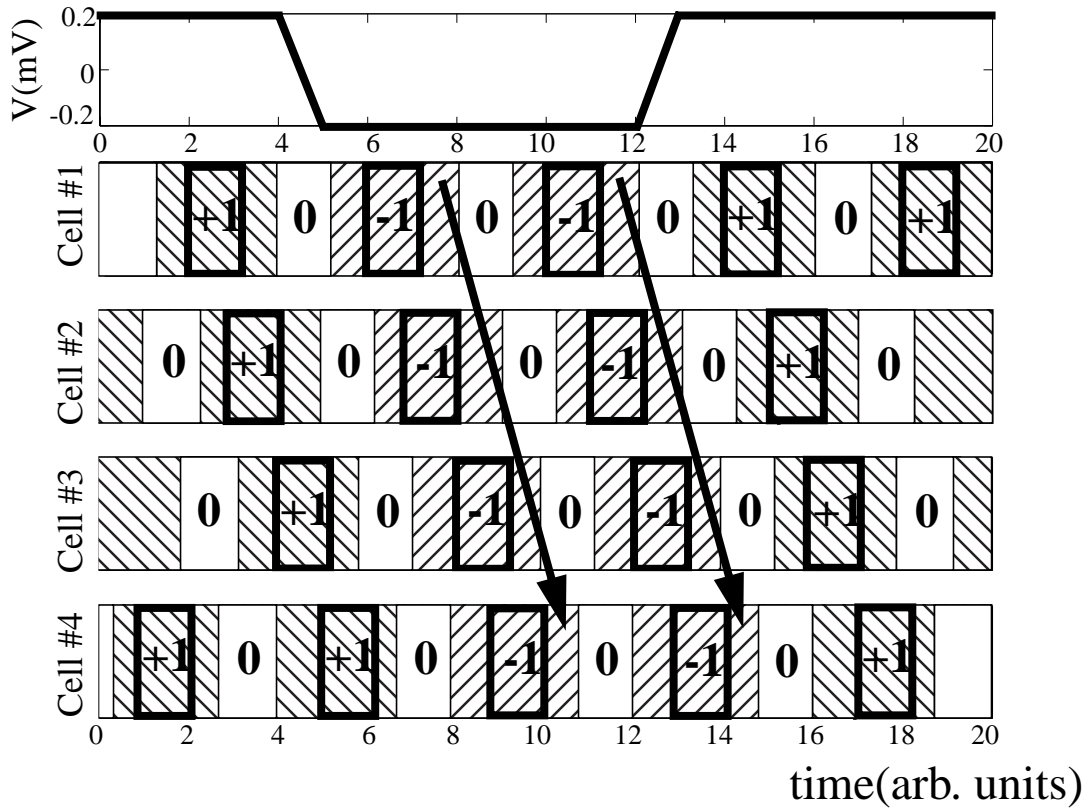
FIGURE 3.11. Simulation of a QCA line of four cells. The top plot shows the V differential input bias of the first cell as the function of time, the other four graphs are the polarizations of the cells. ("0" refers to the null state.) The polarization of a cell is valid if it is in the locked operational mode. In this case the polarization is shown in the frame in the graph. Each cell follow their left neighbor's polarization with a delay.

3.2.4 Conclusions

A structure was proposed to realize the adiabatic switching with metal-island QCA cells. Adiabatic switching provides a solution for the crucial problem of ground state computing, namely, that a larger system may settle in a metastable state instead of the ground state. It also makes pipelining and constructing large, digital-like QCA circuits possible.

The core of the proposed QCA cell is a bistable element consisting of three metal islands, tunnels junctions, and capacitors. Its operation was presented in a simulation example, on the basis of phase diagrams. Beside an individual half cell the operation of a cell line was also shown.

3.3 Conductance suppression in coupled double-dots [45]

The electrostatic interaction between two capacitively-coupled metal double-dots is studied at low temperatures. Experiments show that when the Coulomb blockade is lifted by applying appropriate gate biases to both double-dots, the conductance through each double-dot becomes significantly lower than when only one double-dot is conducting. A master equation is derived for the system and the results obtained agree well with the experimental data. The model suggests that the conductance lowering in each double-dot is caused by a single-electron tunneling in the other double-dot. Here, each double-dot responds to the instantaneous, rather than average, potentials on the other double-dot. This leads to correlated electron motion within the system, where the position of a single electron in one double-dot controls the tunneling rate through the other double-dot (Correlated transport has also been discussed in the literature. Refs. 24, 27 and 36 analyze the transport of electron-hole pairs (excitons) through arrays of capacitively-coupled double-dots[49].)

The four metal (aluminum) dot system used in this experiment can be seen in Fig. 3.12(a). The voltage sources, V_{Dleft} and V_{Dright}, apply small biases, and currents I_{left} and I_{right} are measured. A symbolic representation of the four dots is shown in Fig. 3.12(b). The circles denote the dots, and the lines indicate the possibility of interdot tunneling.

In measuring the conductance through one double-dot (DD) a significant (35-40%) conductance lowering was observed if the other DD was also conducting. This will be referred to as *conductance suppression* in this paper. Our analysis reveals that the cause of the conductance suppression is correlated electron transport in the whole two-DD system; that is, one DD responds to the instantaneous position of the electron in the other DD, and
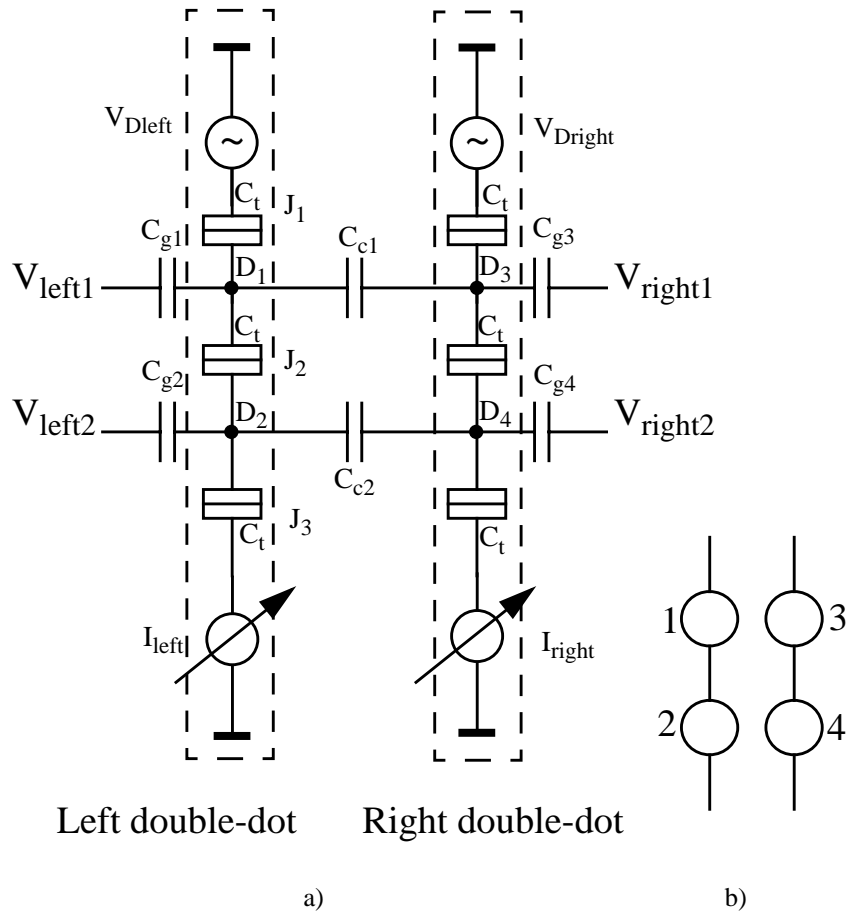
FIGURE 3.12. (a) Two-DD system. The D_1, D_2, D_3 and D_4 denote the four metal islands (dots). The V_{Dleft}/V_{Dright} voltage sources and the I_{left}/I_{right} current meters are used for double-dot conductance measurements. (b) The symbolic representation of the system. The circles and the lines represent metal islands and tunnel junctions, respectively.

not to the average potential caused by the alternation of the charge configurations in the other DD. In the latter case, the conductance lowering would not happen.

In the first subsection the experiments are explained in detail. In the second subsection the experimental results and those obtained from the model are compared. The Appendix gives some details about the computation of the current and the average P=+1/ P=-1 transition time.

3.3.1 Experiment

Fig. 3.13 is a micrograph of the four-dot structure. D_1 and D_2 are the left DD; D_3 and D_4 are the right DD. The Al/AlO$_x$/Al tunnel junctions were fabricated on an oxidized Si substrate using electron beam lithography and shadow evaporation[46]. The area of the junctions was about 50x50 nm^2. Measurements were performed in a dilution refrigerator with a base temperature of 10 mK. The electron temperature during the experiment was
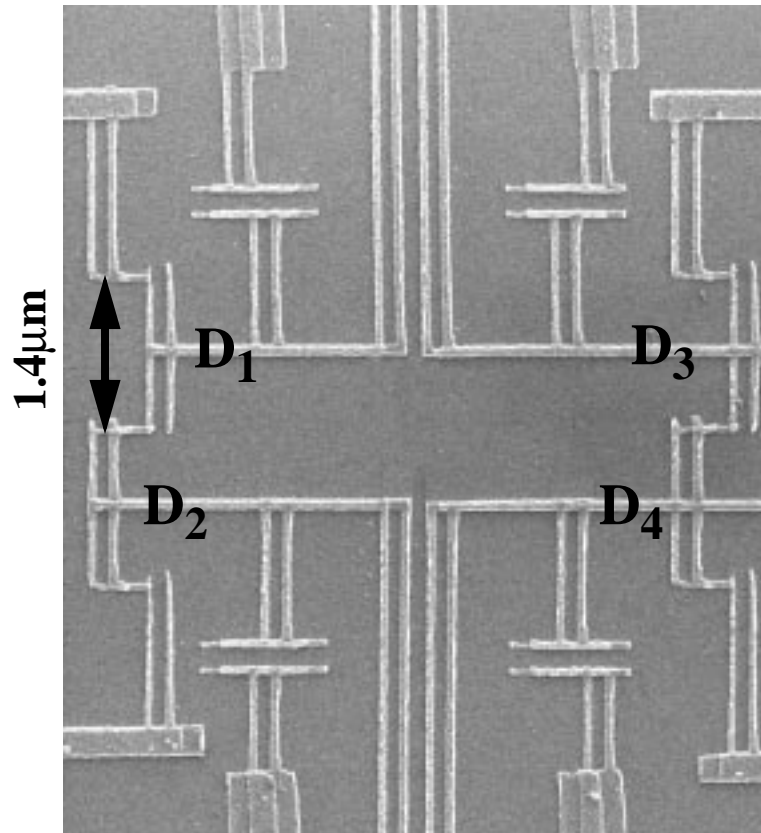
FIGURE 3.13. Micrograph of the device which consists of four metal islands (dots) denoted by D_1, D_2, D_3 and D_4.

70 mK, according to independent temperature measurements[51]. The conductance of each DD was measured simultaneously using standard AC lock-in techniques with 5 μV excitation, and a magnetic field of 1 T applied to suppress the superconductivity of

aluminum. Capacitances in the circuit ($C_t \approx 1.44$ e/mV, $C_{ci} \approx 0.9$ e/mV, $C_{gi} \approx 0.45$ e/mV; See Fig. 3.12.) were determined from periods of Coulomb blockade oscillations and I-V measurements[47]. To nullify the effect of parasitic cross-talk capacitances between dots and nonadjacent gates, a charge cancellation technique, described elsewhere[48], was used.

In the experiment we considered the behavior of a QCA cell, consisting of the two double-dots, to determine the best conditions for QCA operation. The signs of the gate biases were chosen to allow movement of an electron within a double-dot while keeping the total number of electrons constant. We noticed that conductance decreased in both DDs whenever both were conducting.

To understand the experiment we need to examine the charging processes of a two-DD system. The behavior of one DD can be described by the so-called *honeycomb*[15-17,33] graph. This is a phase diagram giving the minimum energy charge configurations as the function of the two electrode voltages. For the whole two-DD system, the electrode voltages of both DDs must also be included in the full description; however, this would mean that the ground state charge configuration must be given as a function of four parameters. In our experiment symmetric input voltages were applied for the DDs. This reduces the number of parameters to two and the occupancy can now be given as a function of $V_{left}=V_{left1}=-V_{left2}$ and $V_{right}=V_{right1}=-V_{right2}$.

Fig. 3.14(a) shows the phase diagram of the two-DD system if there is no coupling ($C_{ci}=0$) between the left and right DD. The phases corresponding to different minimum energy charge configurations are separated by lines, similar to the usual honeycomb graph. However, a phase is now described by the occupancy of all four dots. (The overline
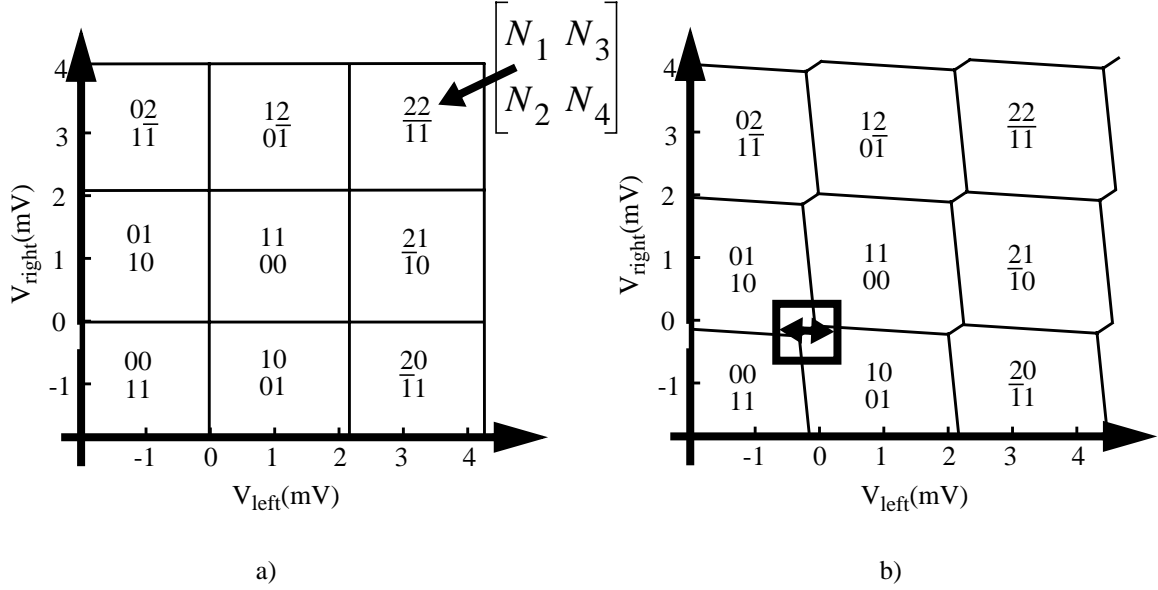
FIGURE 3.14. (a) The phase diagram of the two-DD system if there is no coupling ($C_{ci}=0$) between the left and right DDs. The figure shows the $[N_1N_2;N_3N_4]$ most probable charge configuration as the function of the input voltages. (b) The phase diagram of the two-DD system when the left and right DDs are capacitively coupled. The framed part of the phase diagram is studied in this paper. At the phase borders one of the DDs (e.g., [01;10]/[01;01]) or both of them (e.g., [01;10]/[10;01]) conduct. The arrow corresponds to QCA operation.

denotes negative sign in the figure, e.g., $\overline{1}$=-1.) The left two numbers belong to the left DD, and the right two belong to the right DD. We denote the occupancy by $[N_1N_2;N_3N_4]$ where N_i is the occupancy of the dot D_i. Note, that for the phase around $V_{left}=V_{right}=0$ we choose the [01;01] occupancy of our reference instead of [00;00]. It corresponds to simply a rigid shift of the operating point. In Fig.4(a) the two DDs are independent of each other. By increasing the V_{left} (V_{right}), only the occupancy of the left DD (right DD) changes. The occupancy of one dot of the DD increases by one, the other dot's occupancy decreases by one.

Fig. 3.14(b) shows the phase diagram for non-zero coupling between the DD's. The points where four phase borders meet are now split into two triple points. The square-

48

shaped phase regions turn into hexagons. In Fig. 4(b) the crucial region of the phase

diagram, which we examine experimentally, is framed. There are four phases in this

region: [01;01], [01;10], [10;01] and [10;10]. During QCA operation the V_{right} voltage is

kept constant and V_{left} changes sign. The system moves on a horizontal line in the phase

diagram (shown by the arrow). By choosing an appropriate V_{right}, this horizontal line will

cross the phase border between the [10;01] and [01;10] phases, corresponding to a

transition from one polarization state to the other.

Figs. 3.15(a) and (b) show the phase borders where the left DD and the right DD,

respectively, conduct. The experimental results of the conductance measurement

a)   b)
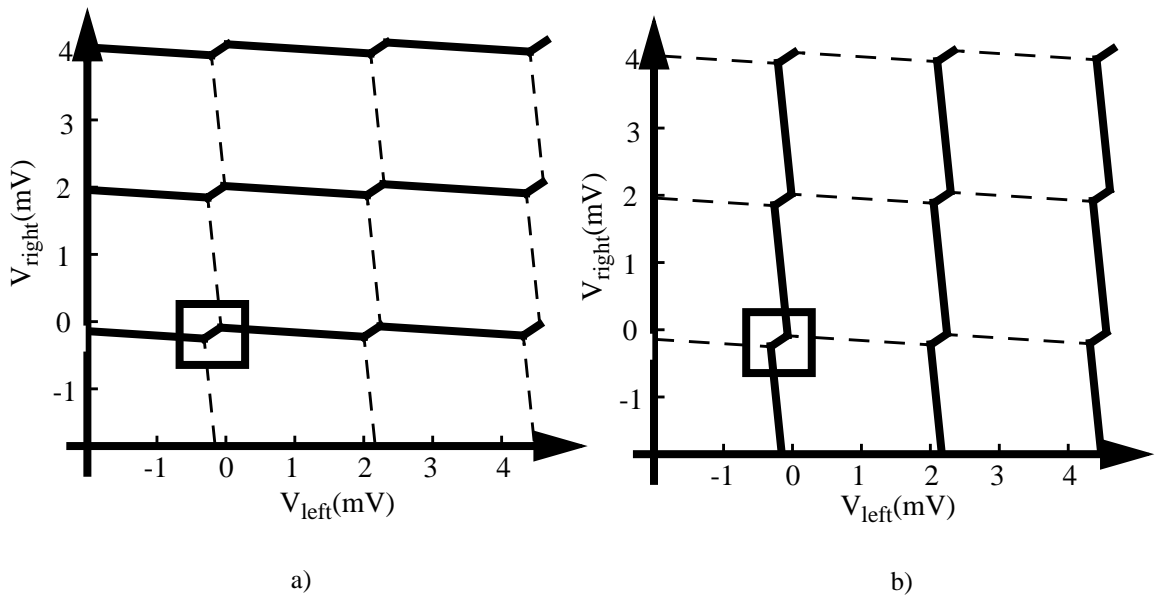
FIGURE 3.15. The phase borders where the (a) left and the (b) right DD conduct. The
conductances for the framed part are shown in Fig. 3.16 magnified.

corresponding to the framed parts of Figs. 3.15(a) and (b) are shown in Figs. 3.16(a) and

(b). When only one DD conducts, the height of the conductance peak at the border is

almost independent of the applied input voltages. However, at the phase borders, where

both DD conduct, the conductance is significantly (up to 35-40%) decreased. The conductance lowering in the left and right DDs is clearly visible in the center of the corresponding conductance graphs of Figs. 3.16(a) and (b). The conductance lowering can
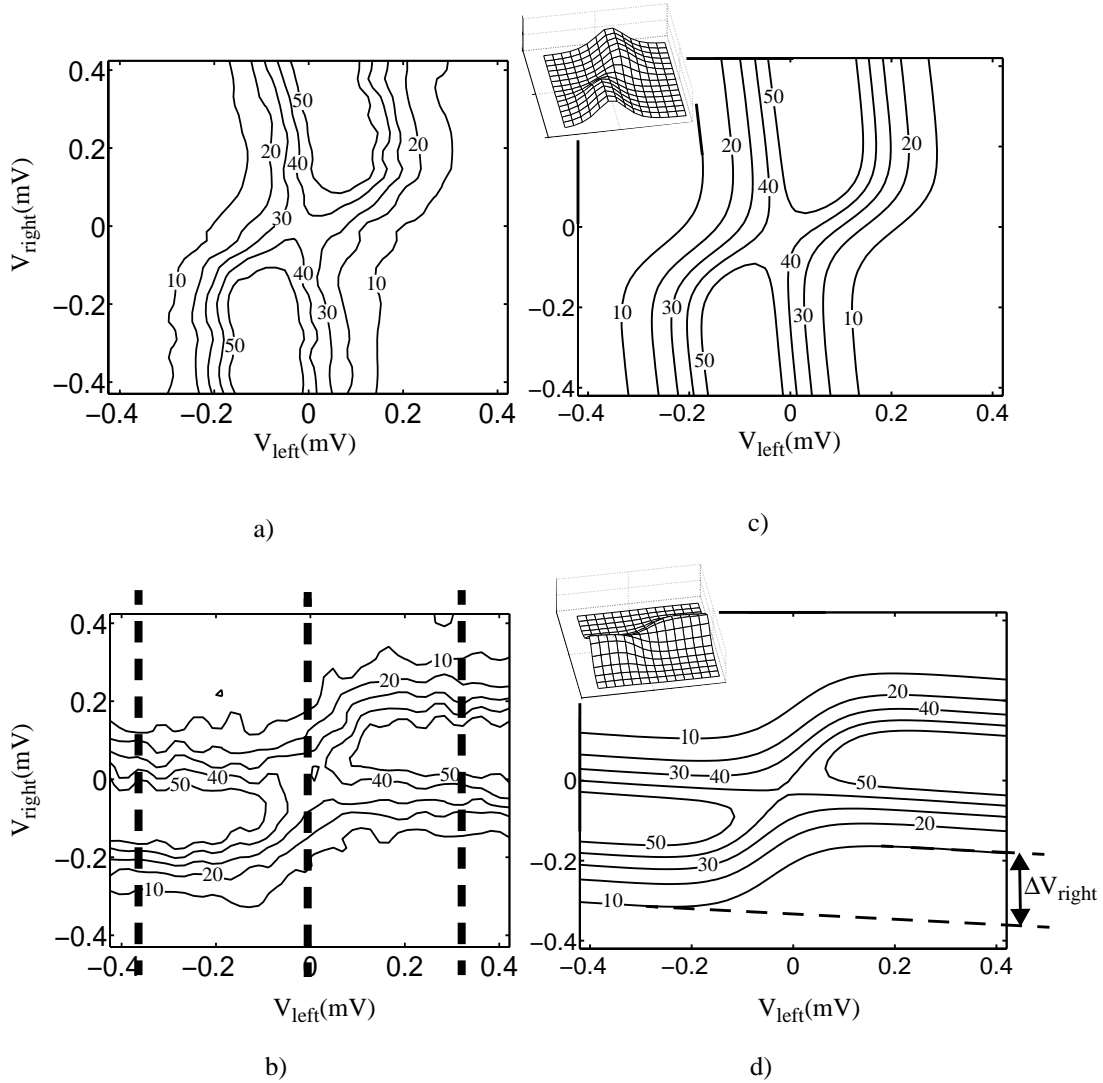
FIGURE 3.16. Comparison of the (a-b) measured and the (c-d) calculated conductance curves of the left and right double-dots. The conductances are given as a function of V_{left} and V_{right}. In (d) the ΔV_{right} voltage shift is the effect of the change of occupancy in the left DD. The 10, 20, 30, 40 and 50 nS contours are shown. The conductance suppression is clearly visible in the center of the graphs. For (c) and (d) the insets show the three-dimensional conductance plots. The curves corresponding to the three vertical lines in (b) are given in Fig. 3.17.

be also seen in Fig. 3.17, where the conductance of the right DD is given as a function of V_{right} for three different V_{left} voltages. It is this lowering which the theoretical analysis of the next two sections will explain.
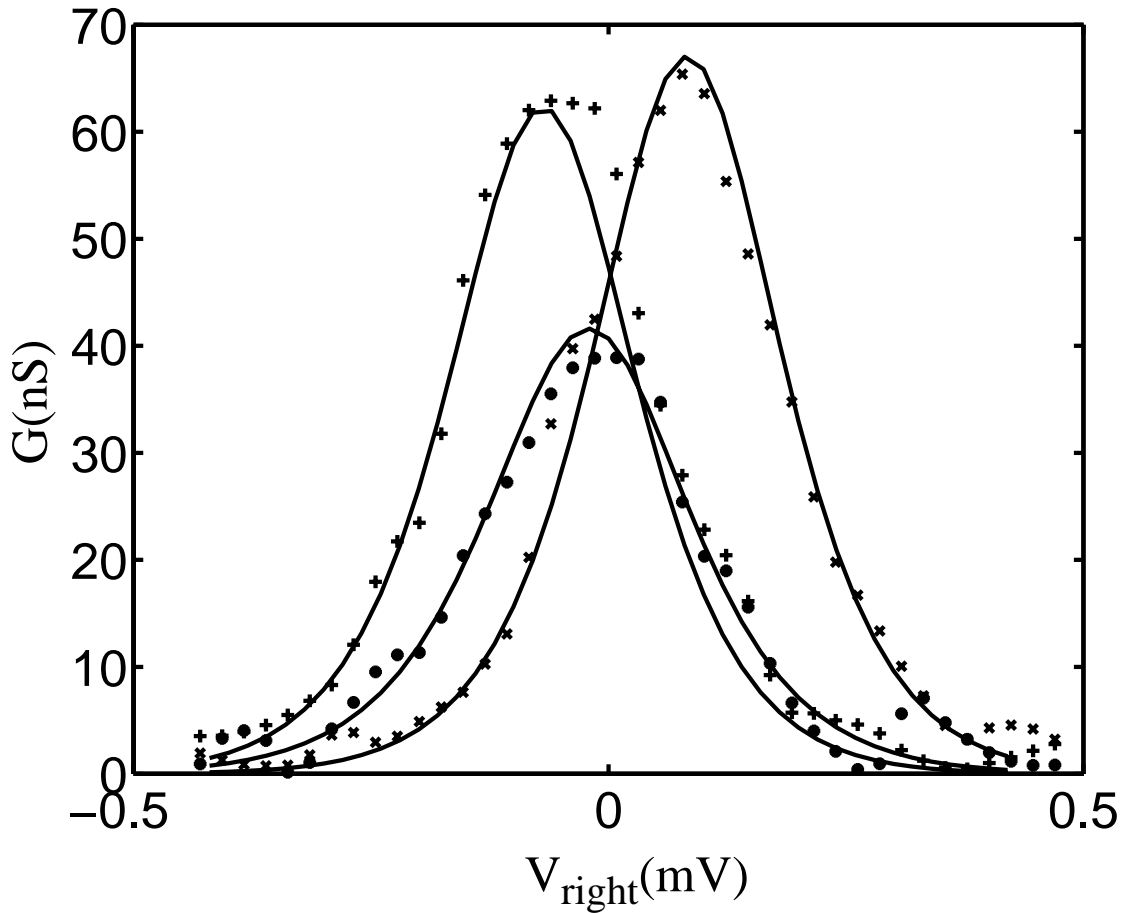
FIGURE 3.17. The measured (crosses and dots) and computed (solid line) conductance curves as the function of V_{right} for three different V_{left} voltages. The curves correspond to the three vertical lines in Fig. 3.16(b).

3.3.2 Results and discussion

Based on the numerical solution of the master equations, Figs. 3.16(c) and (d) show the calculated conductances of the left and right double-dots as the functions of V_{left}

and V_{right}. (Compare with the experimental graphs shown in Figs. 3.16(a) and (b).) In Fig. 3.17 the computed conductance (solid line) and the measured conductance (crosses and dots) curves are shown as the function of V_{right} for three different V_{left} voltages. For the temperature the measured T=70 mK was taken[51]. Due to the unknown background charge, the conductance curve was allowed to shift rigidly in the V_{left} and V_{right} plane for fitting. The model uses the tunneling resistance as fitting parameter. The results of the calculations agree with the experiment upon taking R_T=430 kΩ. (The measured room temperature resistance of the tunnel junctions varied between 400 and 550 kΩ.) It can be observed that the conductance is lower on the phase border where both DDs conduct (in the center of the graphs in Figs. 3.16(c) and (d)), which matches the experiments.

We have shown that the solution of the master-equations for the two-DD system quantitatively agrees with the measured data. The master-equation model describes the correlated electron transport through the two DDs. This statement can be supported by computing the correlation between the charge polarization of the two DDs. The charge polarization of a DD is defined with the occupancy of the top and bottom dots as

$$P_{DD} = N_{top} - N_{bottom}. \tag{3.34}$$

It is +1 and -1 for the [10] and the [01] double-dot charge configurations, respectively. We define the correlation function between the double-dots as:

$$C_{pp} = \langle P_{left}P_{right}\rangle - \langle P_{left}\rangle\langle P_{right}\rangle, \tag{3.35}$$

where $\langle \dots \rangle$ denotes the thermal expectation value. This correlation function would be zero if each DD only responded to the average charge on the other. In Fig. 3.18 the dependence of the correlation function is shown on the input voltages. C_{pp} has a peak at the origin, where the conductance lowering occurs. Further from the origin its value is
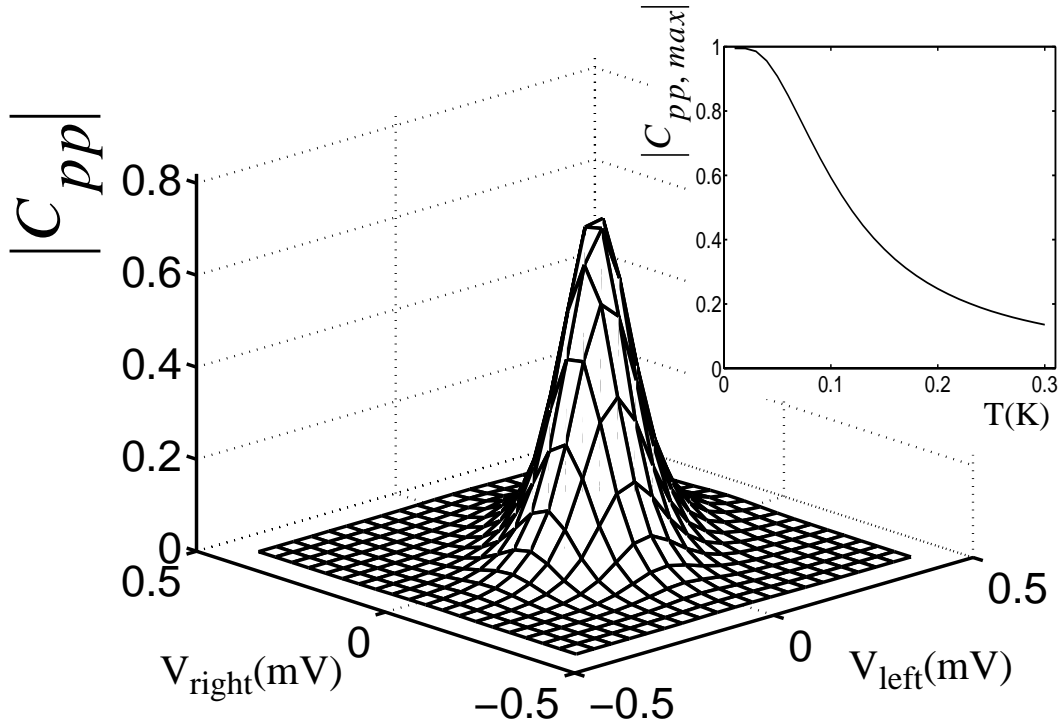
FIGURE 3.18. The correlation between the top dots of the two DDs as a function of V_{lef} and V_{right} for T=70 mK. The correlation is maximum at the origin where the conductance lowering occurs. The inset shows the temperature dependence of the correlation peak. I decreases with increasing temperature.

zero, indicating that there is no correlation between the double-dots there. The inset shows the temperature dependence of the correlation peak. The correlation between the double-dots decreases with increasing temperature. At the experimental temperature, the height of the correlation peak is $\left| C_{pp} \right| \cong 0.75$.

Correlated electron transport through the two DDs means that one DD responds to the instantaneous electron position in the other DD. It is instructive to examine what would happen if one DD responded only to the *average* charge density of the other DD. Fig. 3.19 shows the calculated conductance of the right DD in this case. (See Fig. 3.16(d)
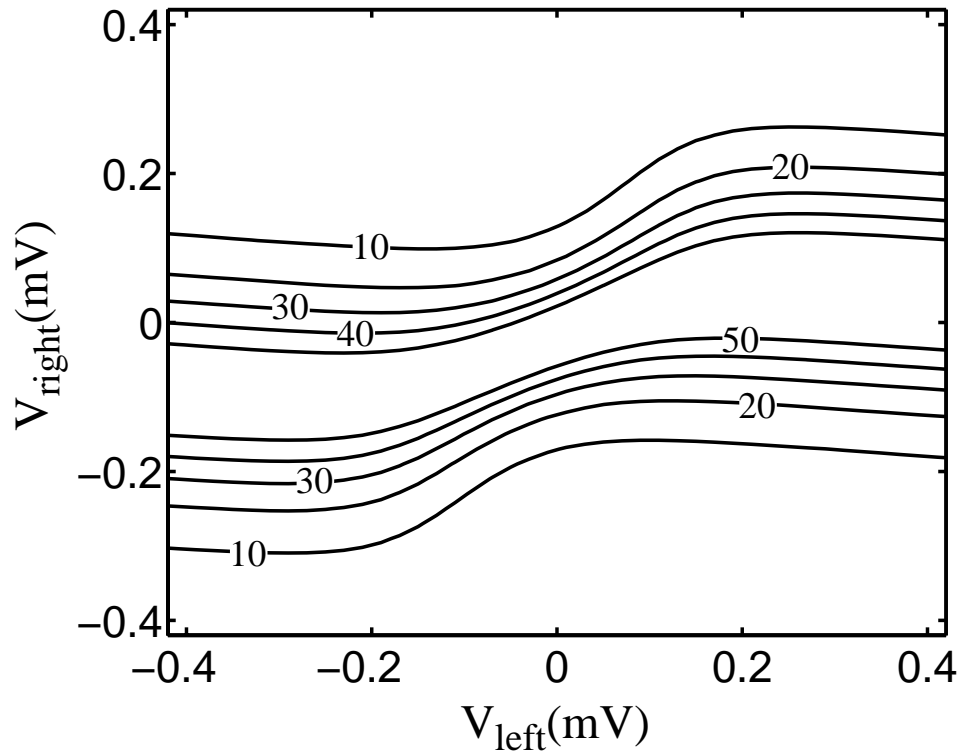
FIGURE 3.19. The calculated conductance of the right DD for the case if the right DD responded to the average charges on the left DD. In the graph, the 10, 20, 30, 40 and 50 nS contours are shown. The conductance lowering is not seen in this figure. (Compare with Fig. 6(d).)

for comparison.) The conductance of the right DD was computed placing static charge in the left DD, corresponding to its time averaged charge density. The conductance lowering cannot be seen, and this also implies that the electron transport through the two DD is correlated.

In Fig. 3.16(d) ΔV_{right} denotes the voltage shift in the conductance graph of the right DD due to the change of occupancy in the left DD. If the coupling capacitance is higher between the two double-dots, this voltage shift and the conductance lowering will be larger[50]. However, if the two double-dots are coupled with smaller capacitances, ΔV_{right} and the conductance lowering decreases. In the limit of uncoupled DDs, conductance lowering does not occur and ΔV_{right}=0.

We can use this analysis to estimate the P=+1/P=-1 transition rate. The results of the computations give 50MHz for this particular two-DD structure. During the P=+1/P=-1 transition the input voltage of the left DD is changed, while the input voltage of the right DD is kept constant. The input voltage of the left DD is changed in such a way that it mimics the switching of an adjacent cell[44].Modifying the capacitances, especially the coupling between the two DDs, and decreasing the resistance of the tunnel junctions can increase the transition frequency[50].

3.3.3 Conclusions

In this section electron transport through coupled double-dots has been analyzed. Experimentally, a suppression of conductance in one double-dot was observed when the second double-dot was conducting. This is explained theoretically in terms of the correlation of electron motion in the system. A model has been developed which rather accurately reproduced the experimental data. The straightforward interpretation of this model is that the electron in one double-dot responds not just to the time average fluctuations of charge in the neighboring double-dot, but to the instantaneous charge configuration. This leads to a non-vanishing correlation in the coupled electron motion.

CHAPTER 4

QCA QUANTUM DYNAMICS USING THE STATE VECTOR DESCRIPTION

Unlike the metal-island implementation, that is strongly coupled to the heat bath, the semiconductor realization of the QCA can be modelled as a coherent system; thus the Scrödinger equation can be used for its description. A QCA cell consists of four quantum dots and two electrons. Ignoring spin, a cell can be described by a 16 element state vector[8]. For the line of N cells a 16^N elements state vector is required.

The large number of vector elements needed for state description makes it difficult to model QCA arrays. Fortunately, according to Ref. [8] its is possible to consider a QCA cell as a two state system. The Hamiltonian for a QCA line as a two-state system is:

$$\hat{H} \;=\; -\gamma \sum_{i=1}^{N} \hat{\sigma}_x(i) - \frac{E_k}{2} \sum_{i=1}^{N-1} \hat{\sigma}_z(i)\hat{\sigma}_z(i+1) \; , \qquad (4.1)$$

where E_k is the kink energy (the energy of two cells being oppositely polarized) and γ is the tunneling energy. γ is zero, if the interdot tunneling barriers in the cells are high and the tunneling rate is very low (zero). γ is large, if the he interdot tunneling barriers in the cells are low and the tunneling rate is high. The tunneling barriers of the cells are connected to electrodes and their heights is controlled externally by voltage sources.

The Hamiltonian of a QCA cell line has the same form as that of an Ising spin chain in transverse magnetic field. $E_k/2$ and γ plays the role of the J exchange energy and the transverse magnetic field, respectively.

The polarization of the kth cell can be interpreted as the expectation value of the σ_{zk} Pauli spin matrix:

$$P_k = -\langle \hat{\sigma}_{zk} \rangle . \tag{4.2}$$

With the negative sign we follow the convention of Ref. [57] choosing the sign of the Pauli spin matrices:

$$\hat{\sigma}_x = \begin{bmatrix} 0 & 1 \\ 1 & 0 \end{bmatrix}, \ \hat{\sigma}_y = \begin{bmatrix} 0 & i \\ -i & 0 \end{bmatrix}, \text{ and } \hat{\sigma}_z = \begin{bmatrix} -1 & 0 \\ 0 & 1 \end{bmatrix}. \tag{4.3}$$

Considering the QCA cell line, as coupled two-level systems, for a line of N cells a 2^N element state vector is needed. (This model will be referred to later as *full-Hamiltonian* model.) This number can be further reduced with the intercellular Hartree-Fock approximation.

The dynamics of a cell line can be obtained from solving the time-dependent Scrödinger equation numerically with the (4.1) Hamiltonian. The initial state of the simulation should be the ground state wave vector that can be obtained as the eigenvector of (4.1) with the minimal eigenvalue (energy). The Hamiltonian and the size of the state vector increases exponentially with the number of cells causing the rapid increase in memory and computational time with the increase of cell number and limiting the maximum length of a cell line that can be simulated on a personal computer to about 10-15 cells. This limit can be improved by using sparse matrix routines for matrix algebra and eigenvalue computation.

4.1 The intercellular Hartree-Fock approximation

The Hartree-Fock intercellular approximation decouples the line of N cells into N single-cell subsystems, which are coupled "classically" through expectation values. The Hamiltonian for the jth cell is:

$$\hat{H}_j = -\gamma_j \hat{\sigma}_x(j) - \frac{E_k}{2} \hat{\sigma}_z(j)(\langle \hat{\sigma}_z(j-1) \rangle + \langle \hat{\sigma}_z(j+1) \rangle) \ . \tag{4.4}$$

(Compare with (4.1).) Introducing

$$\bar{P}_j = -(\hat{\sigma}_z(j-1) + \hat{\sigma}_z(j+1)) = P_{j-1} + P_{j+1} \ . \tag{4.5}$$

and using the matrix form of the Pauli spin operators, the 2x2 Hamiltonian matrix can be obtained as:

$$\hat{H}_j = \begin{bmatrix} -\frac{1}{2}\bar{P}_j E_k & -\gamma_j \\ -\gamma_j & \frac{1}{2}\bar{P}_j E_k \end{bmatrix} . \tag{4.6}$$

4.1.1 The dynamics of a cell block

The dynamics of the cell line is given by coupled single-cell time-dependent Scrödinger equations. The Scrödinger equation of the jth cell is:

$$ih\frac{\partial}{\partial t}|\psi_j\rangle = \hat{H}_j|\psi_j\rangle, \tag{4.7}$$

where the two element state vector can be given as:

$$|\psi_j\rangle = \alpha_j|1\rangle + \beta_j|-1\rangle = \begin{bmatrix} \alpha_j \\ \beta_j \end{bmatrix} . \tag{4.8}$$

The QCA cell is modeled as a two-state level. Its $|\psi_j\rangle$ state is given as the linear superposition of the polarization +1 and -1 states.

According to (4.8), a cell is described by two complex or, equivalently, four real numbers. For a line of *N* cell, *2N* complex numbers are needed. However the degrees of freedom is less than that because the elements of the state vectors must fulfill the constraint:

$$\left|\alpha_j\right|^2 + \left|\beta_j\right|^2 = 1.$$
(4.9)

Moreover, in each cell, due to *phase arbitrariness*, the state vector can be multiplied by a phase factor (with absolute value one) without changing the physics. Due to these two we have, in fact, only two (real) degrees of freedom instead of four. Therefore it seems reasonable to eliminate the extra two variables from the (4.7) Scrödinger equation and to describe the QCA cell by two variables.

Let us choose the two variables to be the *P* polarization

$$P = |\alpha|^2 - |\beta|^2,$$
(4.10)

and the ϕ phase:

$$\phi = \arg\left(\frac{\beta}{\alpha}\right).$$
(4.11)

With these the state vector can be written as

$$\psi = \begin{bmatrix} \sqrt{\dfrac{1+P}{2}}\,e^{i\delta} \\ \sqrt{\dfrac{1-P}{2}}\,e^{i(\phi+\delta)} \end{bmatrix},$$
(4.12)

where δ is the arbitrary phase. Substituting (4.12) into (4.7) and eliminating δ, we get [52]:

$$\hbar\frac{d}{dt}P_j = -2\gamma\sqrt{1 - P_j^2}\sin\varphi_j \tag{4.13}$$

and

$$\hbar\frac{d}{dt}\varphi_j = -\overline{P}_jE_k + 2\gamma\frac{P_j}{\sqrt{1 - P_j^2}}\cos\varphi_j. \tag{4.14}$$

Notice that P represents a classical degree of freedom — it is related to expectation values of observables. By contrast ϕ is a fundamentally quantum variable, a quantum mechanical phase. Beside P and ϕ, κ and ϕ are another possible choice for state variables. Their defining equations are

$$\cos\frac{\kappa}{2} = |\alpha|, \ \sin\frac{\kappa}{2} = |\beta| \tag{4.15}$$

and

$$\varphi = \arg\left(\frac{\beta}{\alpha}\right). \tag{4.16}$$

The P polarization can be given with κ as

$$P = |\alpha|^2 - |\beta|^2 = \left(\cos\frac{\kappa}{2}\right)^2 - \left(\sin\frac{\kappa}{2}\right)^2 = \cos\kappa. \tag{4.17}$$

After some algebra, the state equations with these two state variables are obtained:

$$\hbar\frac{d\kappa_j}{dt} = 2\gamma\sin\phi_j, \tag{4.18}$$

and

$$\hbar\frac{d\phi_j}{dt} = -\overline{P}_jE_k + 2\gamma\cot(\kappa_j)\cos\phi_j. \tag{4.19}$$

Compare this result with the (4.13) and (4.14) state equations for P and ϕ.

4.1.2 Computing the stationary state of a cell block

Taking all the time derivatives to zero in (4.13) and (4.14), and assuming $\phi_j=0$, the steady state polarization of a cell can be computed as

$$P_j = \frac{\dfrac{E_k}{2\gamma}\bar{P}_j}{\sqrt{1+\left(\dfrac{E_k}{2\gamma}\bar{P}_j\right)^2}}.\qquad(4.20)$$

This formula can be used for iterative methods that find the stationary states of a cell block. First a polarization value P_j is assigned to all the cells. Then the $\bar{P}_j$'s, the sums of the polarizations of the neighbors are computed. From the $\bar{P}_j$'s the P_j polarizations can be computed according to (4.20). The last two steps must be repeated until the polarization of the cells do not change any more.

If the cell has only one neighbor, a driver cell, then the well-known *nonlinear cell-to-cell response function* [8] is obtained from (4.20) as shown in Figure 4.1. Note that mathematically (4.13) and (4.14) has another steady state solution, where both time derivatives are zero and $\phi_j=\pi$, however, it can be proved that this is a non-stable equilibrium.

If the driver polarization is near zero then the slope of the curve is

$$\frac{dP}{dP_d} \approx \frac{E_k}{2\gamma}.\qquad(4.21)$$

The method can be extended for more complex structures, e. g., for the majority gate shown in Figure 4.2.
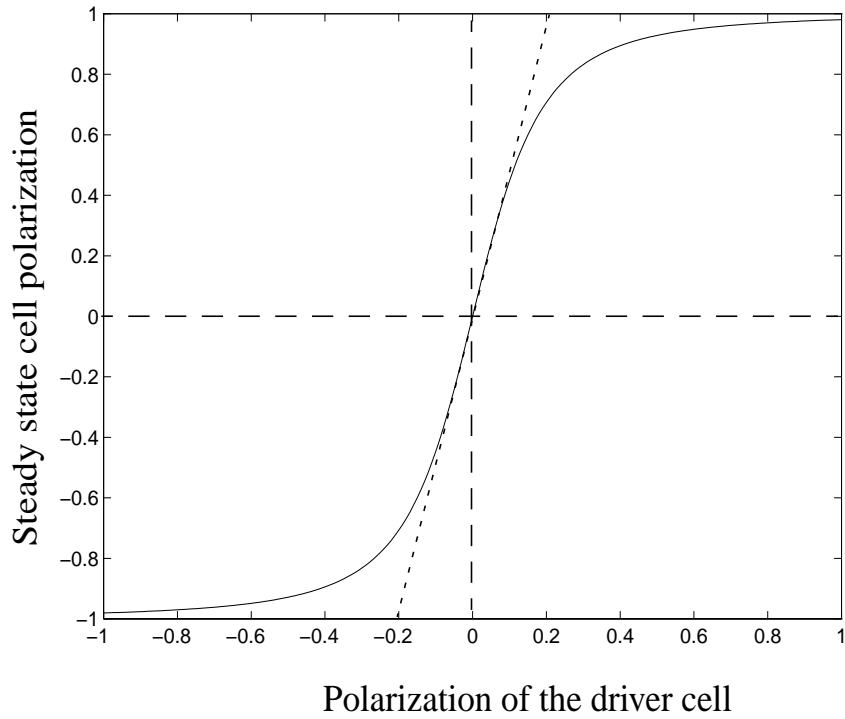
FIGURE 4.1. Nonlinear cell-to-cell response function. The steady-state polarization of a cell as a function of the polarization of the driver. According to (4.21) the slope of the curve at the origin is $E_k/2\gamma=0.2$ (See the slope of the dotted line).
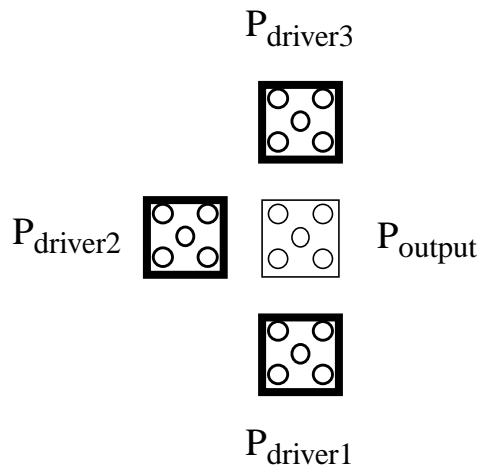
Three driver cells

FIGURE 4.2. Majority gate. If the interdot barriers are high (γ/E_k is small), then the polarization of the output cell is the same as the majority of the driver cell polarizations.

Now

$$P = \frac{\dfrac{E_k}{2\gamma}(P_{driver1} + P_{driver2} + P_{driver3})}{\sqrt{1 + \left(\dfrac{E_k}{2\gamma}(P_{driver1} + P_{driver2} + P_{driver3})\right)^2}} \ . \tag{4.22}$$

If the sum of the three driver polarizations is positive then the polarization of the cell will be also positive, and if the sum is negative then the driver polarization will be negative.

The steady state polarization of an infinite cell line can be obtained substituting $\bar{P}_j = 2P$ into (4.20):

$$P_{saturation} = \pm\sqrt{1 - \left(\frac{\gamma}{E_k}\right)^2} \ . \tag{4.23}$$

Notice that the cell line has a steady state polarization only for $E_k > \gamma$.

4.2 Linearization of the state equations

In this section the QCA state equations will be linearized around the equilibrium polarization and phase of an infinite cell line. The linearized equations are valid for small deviation in the polarization and phase from this equilibrium value. It will be shown that (sine) wave propagation through the cell line is possible only in a very narrow frequency range. This will be demonstrated by simulation results. Moreover it will be shown that the behavior of the additive noise or disturbance during a wave front propagating in the QCA array can be understood via the examination of these small amplitude waves and oscillations.

4.2.1 Linearization of the variables around the equilibrium point

Now let us consider a cell with its left and right neighbors in a cell line. Assume that the phase and the polarization of the cell and the polarization of the left and the right neighbors in the one-dimensional cell line differ from their equilibrium values only a very little:

$$P = P_0 + \Delta P,$$
(4.24)

$$\phi = \phi_0 + \Delta\phi,$$
(4.25)

$$P_{Left} = P_{Left0} + \Delta P_{Left}, \text{ and}$$
(4.26)

$$P_{Right} = P_{Right0} + \Delta P_{Right}.$$
(4.27)

Using (4.23), the equilibrium values are:

$$P_0 = P_{Left0} = P_{Right0} = \sqrt{1 - \left(\frac{\gamma}{E_k}\right)^2} \text{ and}$$
(4.28)

$$\phi_0 = 0 \ . \tag{4.29}$$

The linearizations of (4.13) and (4.14) around the equilibrium point are

$$\hbar\frac{d\Delta P}{dt} = \left.\frac{\partial RHS1}{\partial \Delta P}\right|_{equ} \times \Delta P + \left.\frac{\partial RHS1}{\partial \Delta \phi}\right|_{equ} \times \Delta\phi \ , \text{ and} \tag{4.30}$$

$$\hbar\frac{d\Delta\phi}{dt} = \left.\frac{\partial RHS2}{\partial \Delta P}\right|_{equ} \times \Delta P + \left.\frac{\partial RHS2}{\partial \Delta \phi}\right|_{equ} \times \Delta\phi + \tag{4.31}$$

$$\left.\frac{\partial RHS2}{\partial \Delta P_{Left}}\right|_{equ} \times \Delta P_{Left} + \left.\frac{\partial RHS2}{\partial \Delta P_{Right}}\right|_{equ} \times \Delta P_{Right},$$

where RHS1 and RHS2 are the right hand sides of the two state equations(4.13) and

(4.14):

$$RHS1 = -2\gamma\sqrt{1-(P_0 + \Delta P)^2}\sin(\phi_0 + \Delta\phi) \ , \text{ and} \tag{4.1}$$

$$RHS2 = 2\gamma\frac{(P_0 + \Delta P)}{\sqrt{1-(P_0 + \Delta P)^2}}\cos(\phi_0 + \Delta\phi) - \tag{4.2}$$

$$E_k(P_{Left0} + \Delta P_{Left} + P_{Right0} + \Delta P_{Right}) \ .$$

The derivatives of (4.1) and (4.2) are obtained as

$$\left.\frac{\partial RHS1}{\partial \Delta P}\right|_{equ} = -2\gamma\frac{P_0}{\sqrt{1-P_0^2}}\sin\phi_0 = 0 \ , \tag{4.1}$$

$$\left.\frac{\partial RHS1}{\partial \Delta \phi}\right|_{equ} = -2\gamma\sqrt{1-P_0^2} = -2\gamma\times\frac{\gamma}{E_k} \ , \tag{4.2}$$

$$\left.\frac{\partial RHS2}{\partial \Delta P}\right|_{equ} = 2\gamma\left(\frac{P_0^2}{(1-P_0^2)^{3/2}} + \frac{1}{\sqrt{1-P_0^2}}\right)\cos\phi_0 = 2\gamma\times\left(\frac{E_k}{\gamma}\right)^3 \ , \tag{4.3}$$

$$\left.\frac{\partial RHS2}{\partial \Delta \phi}\right|_{equ} = -2\gamma\frac{P_0}{\sqrt{1-P_0^2}}\sin\phi_0 = 0 \ , \tag{4.4}$$

$$\left.\frac{\partial RHS2}{\partial \Delta P_{Left}}\right|_{equ} = -E_k \ , \text{ and} \tag{4.5}$$

$$\left.\frac{\partial RHS1}{\partial \Delta P_{Right}}\right|_{equ} = -E_k. \tag{4.6}$$

Substituting (4.1-4.6) into (4.30) and (4.31), the linearized state equations are obtained as

$$\hbar\frac{d\Delta P}{dt} = -\frac{2\gamma^2}{E_k} \times \Delta\phi \text{ and} \tag{4.7}$$

$$\hbar\frac{d\Delta\phi}{dt} = \frac{2E_k^3}{\gamma^2} \times \Delta P - E_k \times (\Delta P_{Left} + \Delta P_{Right}). \tag{4.8}$$

Equations (4.7) and (4.8) are two first order differential equations. They describe a cell by two state variables, ΔP and $\Delta\phi$. It is possible to eliminate one of the state variables, and get the cell state equation as a second order differential equation.

To do that, first $\Delta\phi$ must be expressed from the (4.7) linearized state equation:

$$\Delta\phi = -\frac{\hbar E_k}{2\gamma^2} \times \frac{d\Delta P}{dt}, \tag{4.9}$$

and then be substituted into equation (4.8):

$$-\frac{\hbar^2 E_k}{2\gamma^2} \times \frac{d^2\Delta P}{dt^2} = \frac{2E_k^3}{\gamma^2} \times \Delta P - E_k \times (\Delta P_{Left} + \Delta P_{Right}). \tag{4.10}$$

Hence, the state equation as a second order differential equation is obtained as

$$\hbar^2\frac{d^2\Delta P}{dt^2} = -(2E_k)^2 \times \Delta P + (2\gamma)^2 \times \frac{(\Delta P_{Left} + \Delta P_{Right})}{2}. \tag{4.11}$$

4.2.2 Small amplitude wave propagation

Equation (4.11) can be used to find the small amplitude polarization waves that are able to propagate in the cell line. Assuming that the shape of the wave front does not change during the propagation, for ΔP_{Left} and ΔP_{Right} must stand:

$$\Delta P_{Left}(t) \;=\; \Delta P(t - \Delta t_{cell}) \text{ and} \tag{4.12}$$

$$\Delta P_{Right}(t) \;=\; \Delta P(t + \Delta t_{cell}), \tag{4.13}$$

where Δt_{cell} is the time that is necessary for the wave front to pass a cell. From (4.11), (4.12) and (4.13) it follows that

$$\hbar \frac{d^2 \Delta P}{dt^2}(t) \;=\; -(2E_k)^2 \times \Delta P(t) + (2\gamma)^2 \times \frac{\Delta P(t - \Delta t_{cell}) + \Delta P(t + \Delta t_{cell})}{2}. \tag{4.14}$$

Without loss of generality, only the $\Delta t_{cell} > 0$ case will be considered.

Equation (4.14) is linear, that is, if $\Delta P_1(t)$ and $\Delta P_2(t)$ are the solutions of the equation then $c_1 \Delta P_1(t) + c_2 \Delta P_2(t)$ is also a solution. The solution can be looked for as a sum of sinusoidal waves:

$$\Delta P(t) \;=\; \sum_k A_k \sin(\omega_k t + \phi_k). \tag{4.15}$$

For the sake of simplicity, let ΔP have the form:

$$\Delta P(t) \;=\; A \sin(\omega t + \phi). \tag{4.16}$$

After some elementary steps the allowed angular frequencies (ω_k) will be obtained as a function of Δt_{cell}. In the following part we will neglect the k index. The second derivative of (4.16) with respect to the time is:

$$\frac{d^2 \Delta P}{dt^2}(t) = -A\omega^2 \sin(\omega t + \phi) = -\omega^2 \Delta P(t) \tag{4.17}$$

The terms containing time delay can be expressed as:

$$\Delta P(t + \Delta t_{cell}) = A(\sin(\omega t + \phi)\cos(\omega \Delta t_{cell}) + \cos(\omega t + \phi)\sin\omega(\Delta t_{cell})), \tag{4.18}$$

and

$$\Delta P(t - \Delta t_{cell}) = A(\sin(\omega t + \phi)\cos(\omega \Delta t_{cell}) - \cos(\omega t + \phi)\sin(\omega \Delta t_{cell})). \tag{4.19}$$

Hence

$$\frac{\Delta P(t - \Delta t_{cell}) + \Delta P(t + \Delta t_{cell})}{2} = A\sin(\omega t + \phi)\cos(\Delta t_{cell}). \tag{4.20}$$

From (4.16) and (4.20) one can get

$$\frac{\Delta P(t - \Delta t_{cell}) + \Delta P(t + \Delta t_{cell})}{2} = \cos(\omega \Delta t_{cell})\Delta P(t). \tag{4.21}$$

Substituting (4.16), (4.17) and (4.21) into equation (4.14) we got for $\Delta P(t)$:

$$-\omega^2 \Delta P(t) = -\left(\frac{2E_k}{\hbar}\right)^2 \Delta P(t) + \left(\frac{2\gamma}{\hbar}\right)^2 \cos(\omega \Delta t_{cell})\Delta P(t). \tag{4.22}$$

After $\Delta P(t)$ is eliminated, the relationship between ω and Δt_{cell} is obtained as

$$\omega^2 = \left(\frac{2E_k}{\hbar}\right)^2 - \left(\frac{2\gamma}{\hbar}\right)^2 \cos(\omega \Delta t_{cell}). \tag{4.23}$$

From this equation the range of the possible angular frequencies can be obtained. (Remember that this is the angular frequency of the oscillation of a cells in the array.)

$$\frac{2E_k}{\hbar}\sqrt{1 - \left(\frac{\gamma}{E_k}\right)^2} < \omega < \frac{2E_k}{\hbar}\sqrt{1 + \left(\frac{\gamma}{E_k}\right)^2} \tag{4.24}$$

68

In many practical cases the interdot tunneling barriers are relatively high thus $E_k \gg \gamma$, so the angular frequency of the oscillation is restricted to a very narrow range.

If $\Delta t_{cell} = 0$ then

$$\Delta P_{Left}(t) = \Delta P_{Right}(t) = \Delta P(t). \tag{4.25}$$

In this case the polarization of the whole cell block changes together. The frequency of this oscillation is:

$$\omega = \frac{2E_k}{\hbar} \sqrt{1 - \left(\frac{\gamma}{E_k}\right)^2}. \tag{4.26}$$

Let us consider a concrete example with the following cell parameters:

$$\frac{E_k}{\hbar} = 0.25 \text{ and } \frac{\gamma}{\hbar} = 0.05. \tag{4.27}$$

The saturation polarization is

$$P_{saturation} = \pm \sqrt{1 - \left(\frac{\gamma}{E_k}\right)^2} = 0.9798. \tag{4.28}$$

According to (4.24) the range of possible angular frequencies $0.4899 < \omega < 0.5099$. The corresponding period time range is $12.3223 < T < 12.8255$. Fig. 4.3(a) and (b) show the possible $(\omega, \Delta t_{cell})$ pairs.

(a)

(b)
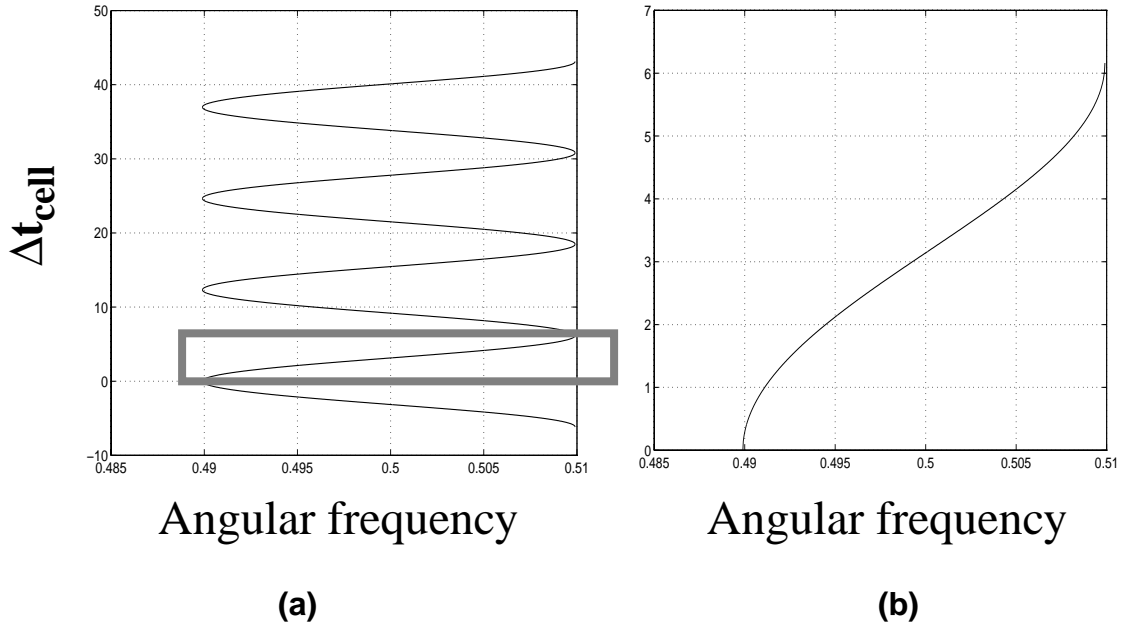
FIGURE 4.3. Δt_{cell} as a function of the angular frequency(ω) of the oscillation of a cell. (b) Magnification of the framed (and relevant) part of (a).

4.2.3 Simulation results

The left edge of a cell block of sixty cells was excited with a sinusoidal signal with small amplitude and different angular frequencies. In correspondence with the theoretical results it was found that for the frequencies that were in the range given above wave started to propagate form the excited edge. On the other edge it was reflected and started to propagate backward. Thus a standing wave appeared as a superposition of the two waves propagating into opposite directions.

Fig. 4.4 shows the polarization and phase curves after 2000 time units for $T=12$, 12.5 and

13.5, respectively. Resonance was experienced only in case of $T=12.5$.
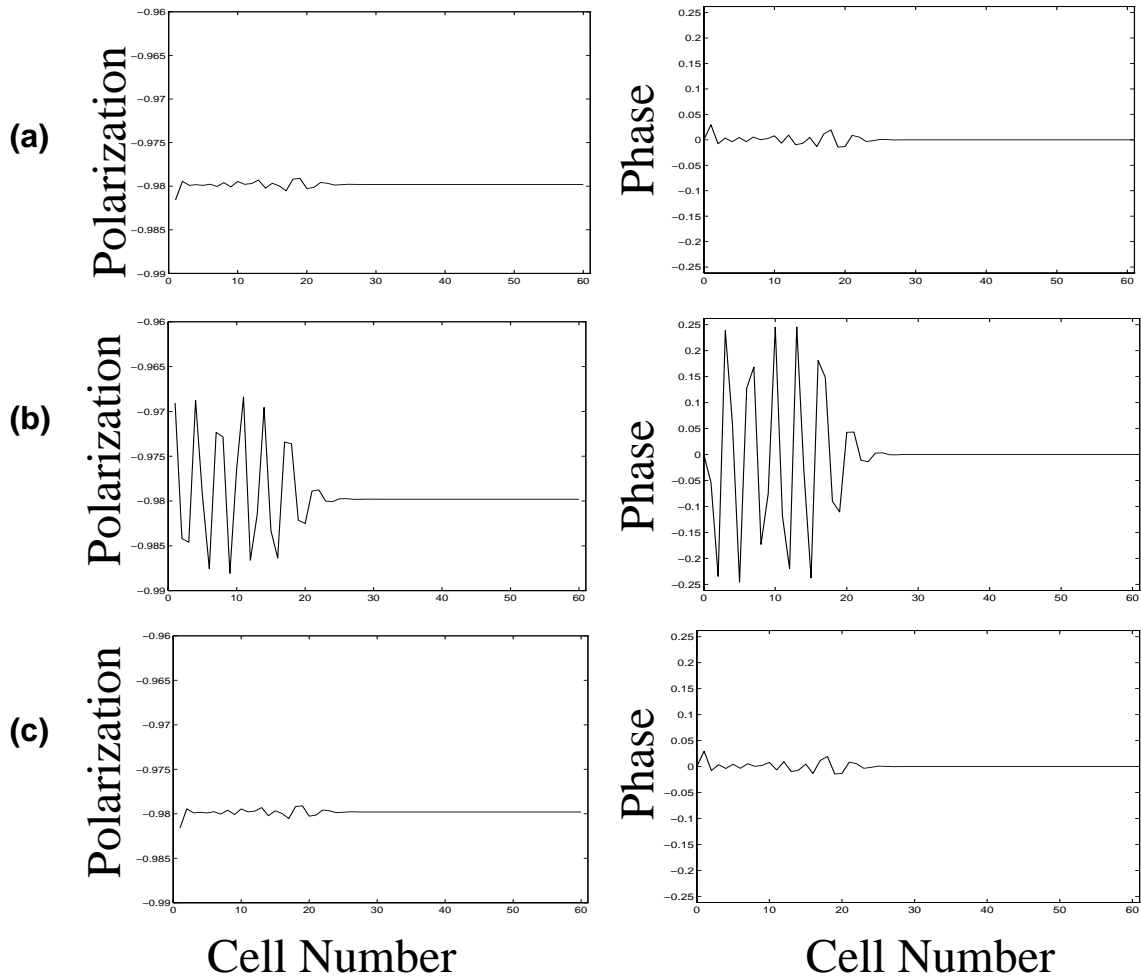
FIGURE 4.4. Polarization and phase of a cell block of sixty cells exciting the left edge with a sinusoidal for (a) $T=12$, (b) $T=12.5$, and (c) $T=13.5$. Resonance occurs for (b), because the excitation frequency is in the allowed range.

The cell block was tried also with non-sinusoidal excitation. The square wave used

exciting the left driver cell is shown in Fig. 4.5(a). The polarization of the first cell can be

seen in Fig. 4.5(b). In this system only a very narrow frequency range can propagate thus

even the polarization of the cell beside the driver cell is a sinusoidal function of time. (The higher frequency components of the square wave were "filtered" out.)

.   Next, the driver cell was excited with the sum of two sine waves with period time T=12.4 and 12.7, respectively. Both period times are in the allowed range. The polarization and phase of a cell, as a function of time is shown. It is easy to recognize the envelope of the shape in Fig. 4.6.

Fig. 4.7 shows the state of the system in case of sinusoidal excitation (T=12.5) between 8000-8120 time units. (The sinusoidal excitation of the left edge started at t=0.) Now time is measured along the vertical axis, increasing from the top to the bottom. The propagation of the waves can be seen on the left hand side, while the checkerboard-like pattern on the right hand side indicates standing waves. The standing waves are the result of the superposition of the waves propagating from the excited driver to the right and the reflected waves propagating to the left.
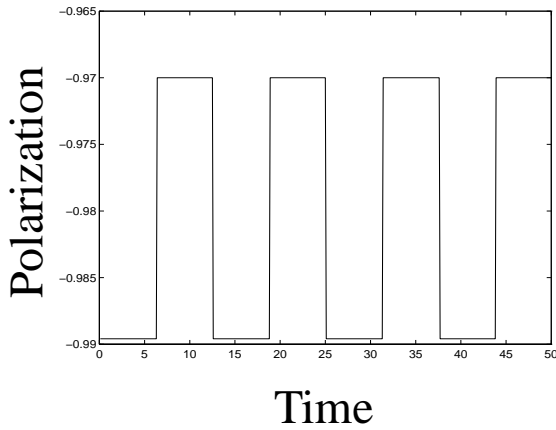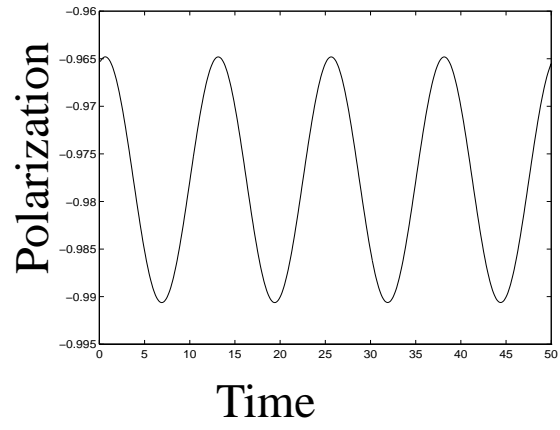
FIGURE 4.5. Excitation of a cell line at the left edge with a square wave (period time=12.5). (a) The polarization of the driver cell as the function of time is shown. (b) The polarization of the cell beside the driver cell as the function of time is shown
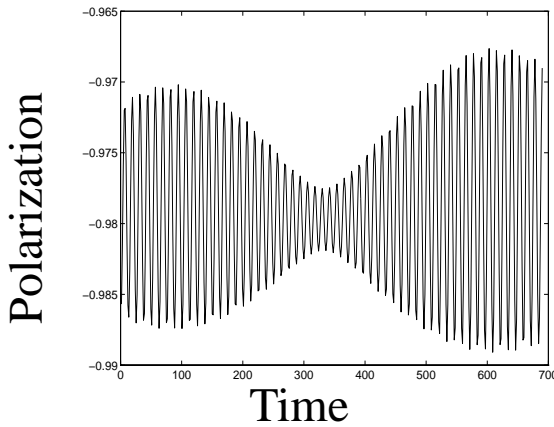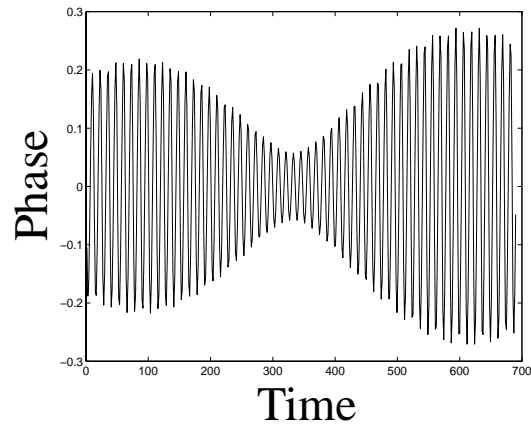
FIGURE 4.6. Excitation of a cell line at the left edge with the sum of two sine waves with near frequencies. The polarization and the phase of a cell as the function of time is shown.
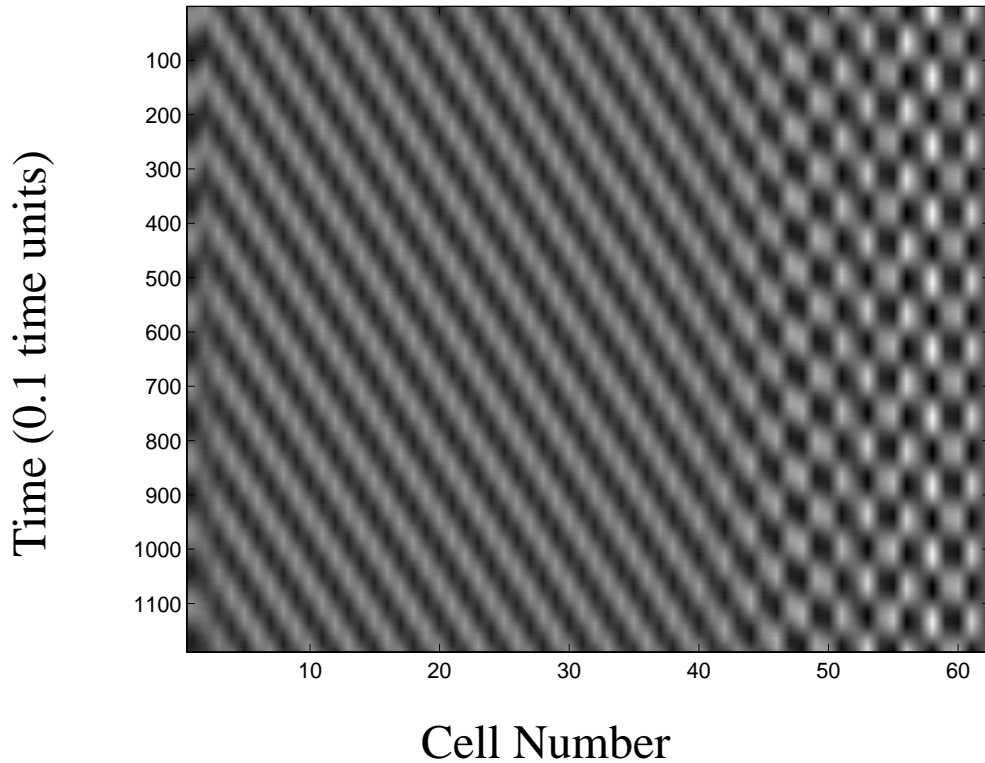
FIGURE 4.7. Polarization of a cell block of sixty cells exciting the left edge with a sinusoidal (T=12.5). This graph shows the state after 8000 time units. From the left edge the propagation of the wave can be seen. Δt_{cell} is about 3.3 time units. At the right edge standing waves appeared because the propagation has already reached the right edge and the wave is reflected. The superposition of the original and the reflected wave gives a standing wave.

4.2.4 Conclusions

In this section, the small amplitude polarization oscillation of the QCA one-dimensional cell array was examined linearizing the cell line around the equilibrium. We saw that wave propagation is possible only in a very narrow frequency range. This small amplitude oscillation can be experienced as "noise" or disturbance added to the expected

wave fronts. Fig. 4.8. shows a snapshot of a propagating wave front. Fig. 4.9. shows the
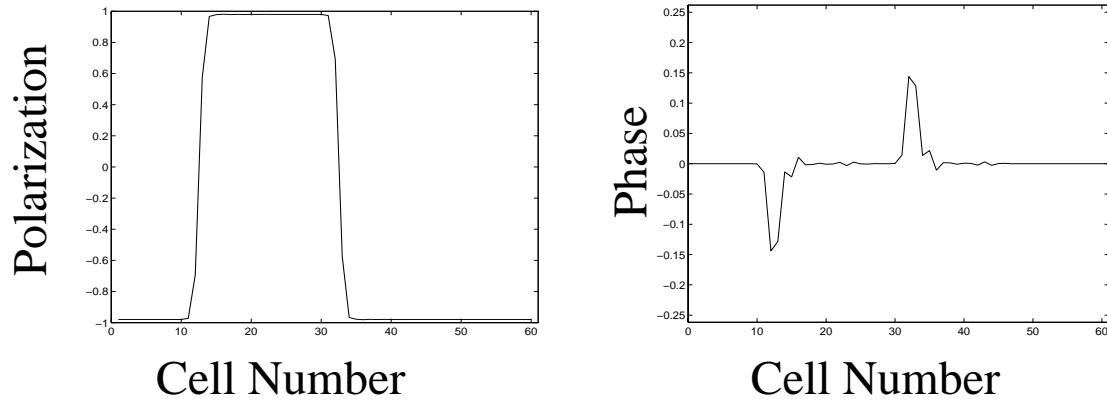
FIGURE 4.8. Wave front propagation in a one-dimensional cell block. Note the disturbances added as a noise to the expected shape
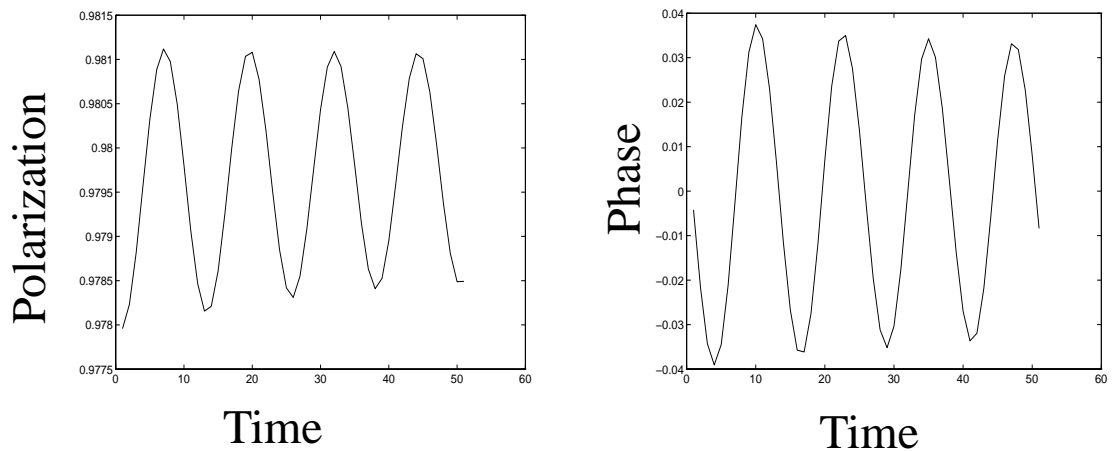
FIGURE 4.9. Polarization and phase of the 15*th* cell in the one dimensional cell block of Fig. 4.8, as function of the time starting from *t*=500 time units. The period time of the small amplitude oscillation is about 12.5 time units.

time function of the polarization and the phase of the 15th cell in the former system from

t=500 time units to 550 time units. The small oscillation can be seen and the period time of

the oscillation is about 12.5 time units, as it was expected. Knowing the allowed frequency

range it is possible to avoid these disturbances in practical applications.

75

4.3 Dynamics of a one-dimensional QCA array

In this section the behavior of a one-dimensional QCA array will be investigated. The propagation and collision of polarization wave fronts and waves will be analyzed based on simulation results.

In Fig. 4.10 an array of 30 QCA cells can be seen. The cells at the left and right edges (that is, the 0th and the 31th cell) are called driver cells, as shown in Figure 4.10. Their polarization can be set externally.
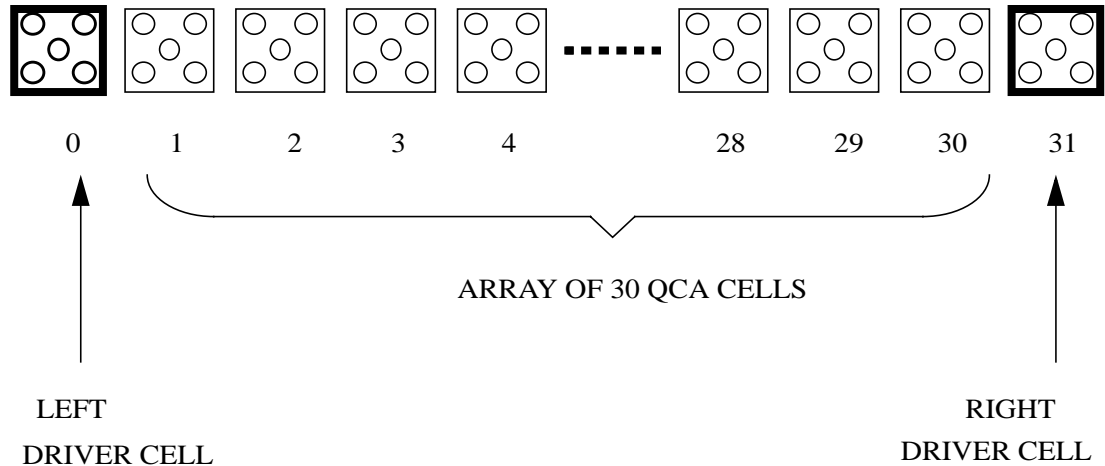
FIGURE 4.10. Array of 30 QCA cells with two driver cells at the right and the left edges, respectively. The polarization of the driver cells can be set externally.

The initial polarization of the cell array was -1. Then by driving the left and the right cells in different ways, the behavior of the cell array was examined.

In subsection 1 the state equations are presented and the propagation of a wave front is demonstrated. In subsections 2 the collision of two wave fronts is analyzed. In subsection 3 an example is shown how to decompose a more complex wave shape into a sequence of the previous two phenomena.

4.3.1 Propagation of a wave front

Every cells in the QCA array is described by two state variables: P (polarization) and ϕ (phase). The two state equations, rewriting (4.13) and (4.14), for the jth cell are given by:

$$\hbar\frac{\partial}{\partial t}P_j = -2\gamma\sqrt{1 - P_j^2}\sin\varphi_j\text{, and} \tag{4.29}$$

$$\hbar\frac{\partial}{\partial t}\varphi_j = -\overline{P}_j E_k + 2\gamma\frac{P_j}{\sqrt{1 - P_j^2}}\cos\varphi_j, \tag{4.30}$$

where E_k, γ and $\hbar$ are constants and $\overline{P}$ is the sum of the polarizations of the neighboring cells.

$$\overline{P}_j = P_{j-1} + P_{j+1}. \tag{4.31}$$

From (4.29) it follows that the cell polarization does not change if and only if $\sin \phi=0$. (One might think that $P_j=+1$ would make the right hand side of (4.29) zero, however, $P_j=+1$ is not allowed because it leads to infinity on the right hand side of (4.30).) Consequently in equilibrium $\sin\phi=0$. The polarization decreases if $\sin\phi >0$ and it increases if $\sin\phi<0$. These basic considerations help us to understand the graphs in the following sections.

The simplest phenomenon in the cell array is a propagating wave front. First both driver cells have -1 polarization. Then the polarization of the left driver cell is raised gradually from -1 to +1. Due to this, the polarization of the first cell changes from -1 to +1, then the same happens to the second, the third, etc. At the end the whole cell block changes its polarization from -1 to +1.

A snapshot of the propagating wave front is shown in Fig. 4.11. Each cell is described by its polarization and phase. The little arrows show the direction of change of the polarization and the phase, respectively. The phase of the cells are zero, except for the
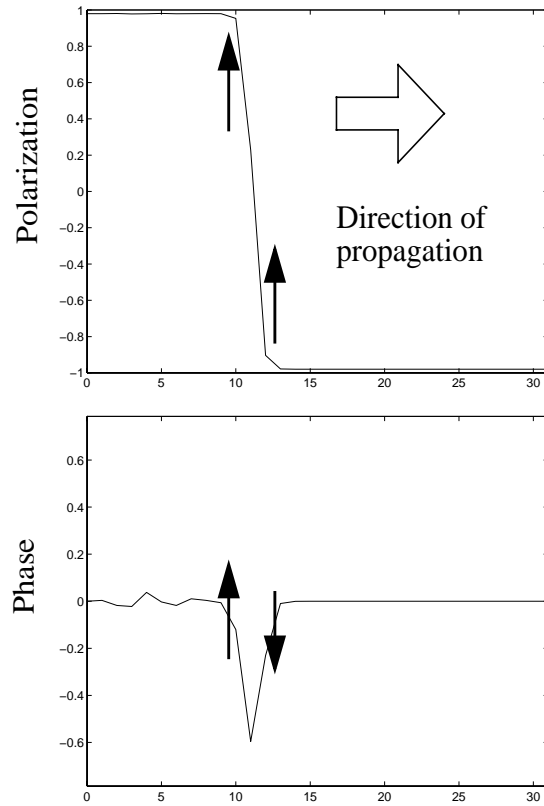
FIGURE 4.11. Propagation of a wave front from the left to the right. A snapshot with the polarization and the phase of the cells are shown. The arrows show the direction of the change for the polarization and the phase. The sign of the phase peak determines in which direction the wave front propagates.

cells at the edge of the wave front. Here a negative peak in the phase can be seen. The sign of this peak determines the direction of propagation.

When the wave front reaches the right driver cell (that has -1 polarization) it is reflected. That is, the wave front begins to propagate in the opposite direction. This can be

seen in Fig. 4.9. As the direction of propagation changes, the negative peak becomes a positive peak on the phase plot. The little arrows again show the direction of change.

If a different slope is applied when rising the polarization of the left driver cell then the speed and the shape of the propagating wave will be different. The smaller the slope the smaller the phase peak and the smaller the propagation speed of the wave.
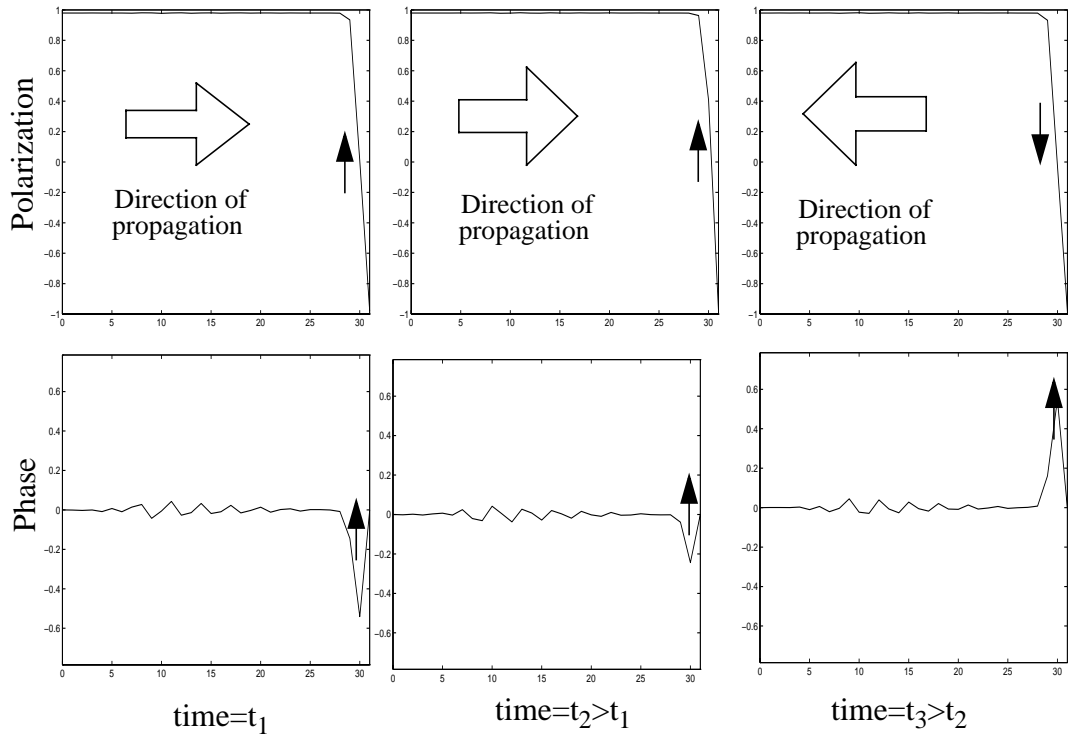
FIGURE 4.12. Collision of the wave front and the fixed border. Three snapshots are shown. The direction of the propagation changes, as the phase peak changes sign.

4.3.2 Collision of two wave fronts

Next the collision of two wave fronts will be discussed. Both the left and the right cells are driven with a -1 to +1 polarization transition. Due to this, a wave front starts from

the left driver cell and another starts from the right, as shown in Figure 4.13. Both wave

fronts have a negative phase peak.
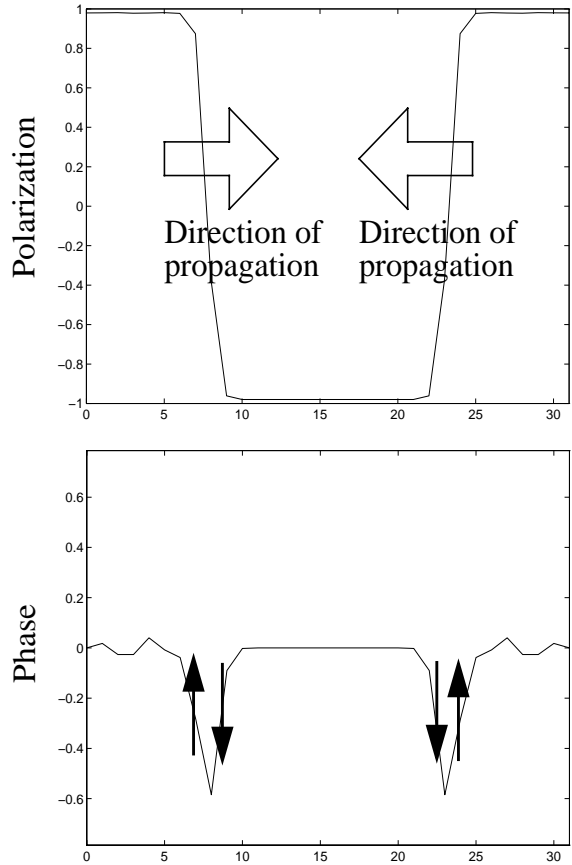
FIGURE 4.13. Two wave fronts propagating in the opposite directions. A snapshot with the polarization and the phase of the cells are shown. The black arrows are indicating the direction of the change.

When the two fronts collide they are reflected. As the direction of their

propagation changes the sign of the phase peak also changes. This can be seen in Figure

4.14. However, the mechanism of the change differs from the previous case. According to

Figure 4.14(b) the two negative phase peaks fuse. In Figure 4.14(c) they become more and

more negative. After reaching $-\pi$, the phase will become positive as shown in Figure

4.14(d). (The phase is kept between $-\pi$ and π.) At the end the one positive phase peak

divides into two peaks (Figure 4.14(e)).
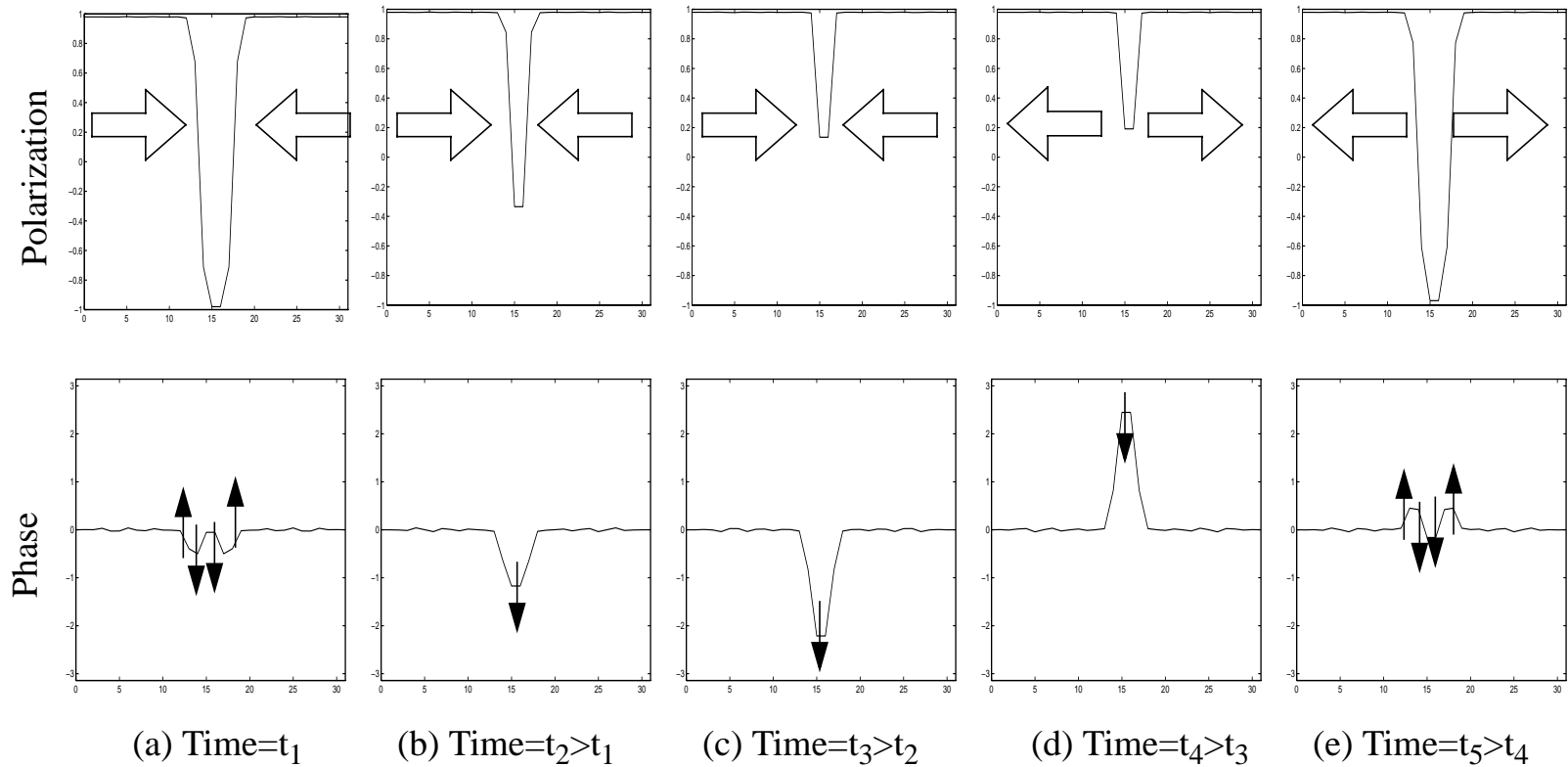
FIGURE 4.14. Collision of two wave fronts. Five snapshots with the polarization and the phase of the cells are shown. After the collision both wave fronts turn back. This can be seen on the change of the sign of the phase peak.

4.3.3 Propagation of a wave

More complex structures can be made of wave fronts. The simplest example is a *wave*. It is constructed of two wave fronts as it can be seen in Figure 4.15. In this case the right cell was driven with a fixed -1 polarization, the left cell was driven with a -1 to +1 to -1 transition. This started a wave propagation from left to right.
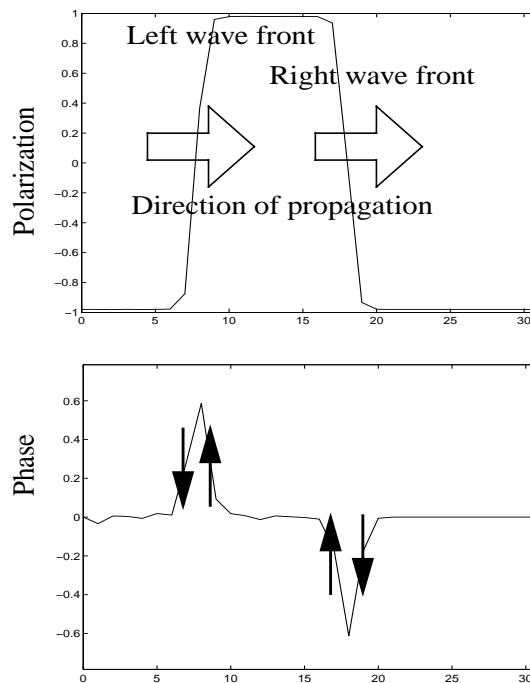
FIGURE 4.15. Propagation of a wave from left to right. The wave is constructed from two wave fronts propagating in the same direction. A snapshot with the polarization and the phase of the cells are shown. The black arrows are indicating the direction of the change.

Reaching the right edge the wave was reflected, however the mechanism of the reflection is more sophisticated than in the case of a reflection of a single wave front. This is summarized schematically in Figure 4.16. The reflection of the wave

82

can be interpreted as a sum of the two basic phenomena described in Sec. 4.3.1 and 4.3.2.

Sec. 4.3.1 describes the collision of a wave front and the fixed border, Sec. 4.3.2 explains

the collision of two wave fronts.

In Figure 4.16(a) both wave fronts of the wave propagates from left to right. When

the right front of the wave reaches the right driver cell, it is reflected and changes the

direction of its propagation as shown in Figure 4.16(b). Then the two fronts collide and

both change their direction of propagation as shown in Figure 4.16(c). Eventually the right

front of the wave reflects when it reaches the right driver cell and it changes direction. The

wave begins to propagate from right to left as it can be seen in Figure 4.16(d).

(a) Time=t_1

(b) Time=$t_2 > t_1$

(c) Time=$t_3 > t_2$

(d) Time=$t_4 > t_3$
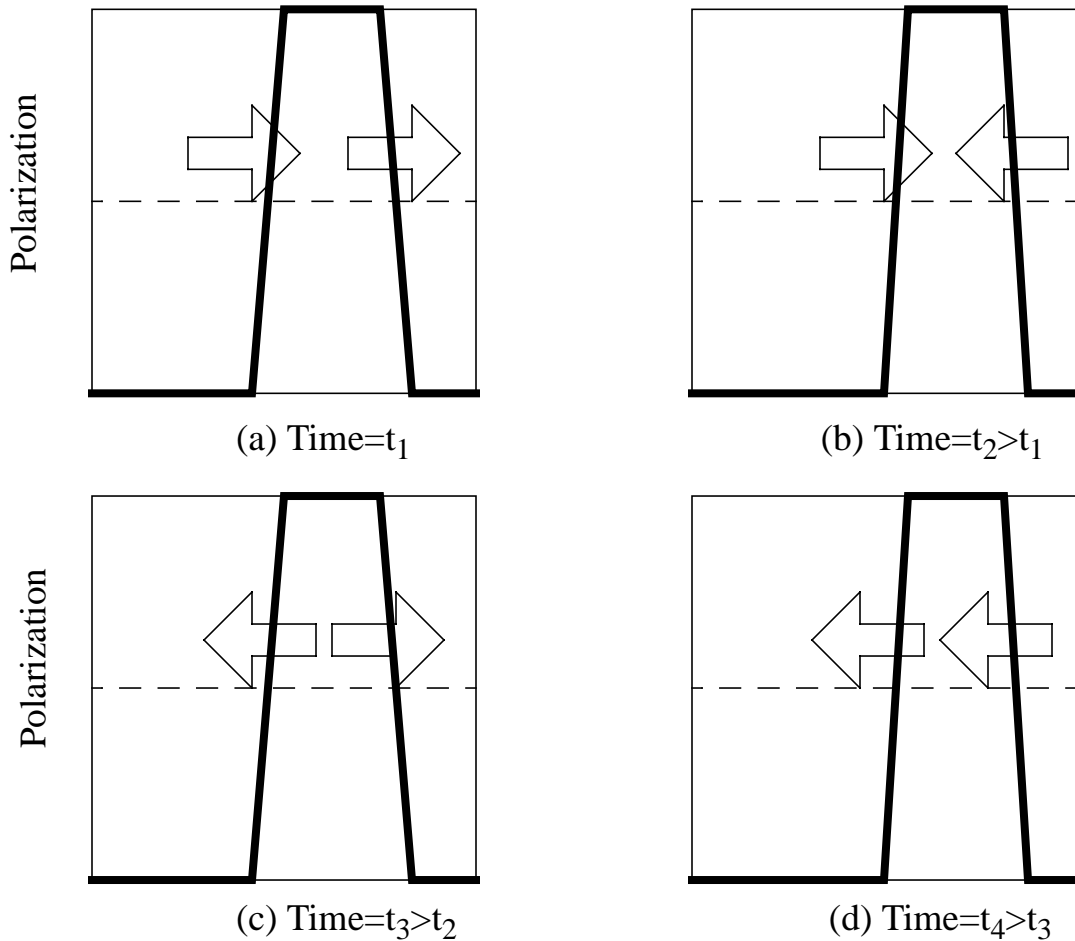
FIGURE 4.16. Reflection of a wave at the right edge. The wave fronts collide with the fixed border and with each other. Eventually the whole wave will turn back.

4.4 Quantum Cellular Neural Networks (QCNNs) [52]

In this section a computing paradigm in which QCA cells composed of interacting quantum dots (QCA's) are employed in a cellular neural network (CNN) architecture. Communication between cells is only through the Coulomb interaction. The cells and their basic behavior are the same as we have previously discussed in the context of the Quantum-dot Cellular Automata (QCA) architecture. The key differences here are that in the quantum CNN (Q-CNN) approach: (1) Each cell is used to encode a continuous rather than binary degree of freedom. (2) We focus on the time dependent problem instead of the ground state. (3) The time-dependent Schrödinger equation can be transformed into the CNN state equations.

We have constructed a simple quantum model of a Q-CNN composed of quantum-dot cells. Each cell contains one classical degree of freedom, the cell polarization, and one quantum degree of freedom, a quantum mechanical phase difference. Mapping onto the CNN paradigm maintains phase information within the cell but no quantum coherence exists between cells. Thus though dynamics is accomplished through the quantum degrees of freedom, information is only carried across the array in classical degrees of freedom.

Our hope is that by connecting the problem of coupled quantum cells to a circuit architecture developed for exploiting conventional analog integrated circuits, we might be able to open up a new solution domain for interconnected quantum devices. Because local connectivity is natural in ultra-small quantum devices, CNN's may prove a natural extension to the QCA architecture and allow a move into non-digital domains.

First we briefly review the CNN paradigm. In the next subsection the connection between the quantum problem and the CNN approach will be demonstrated. At last we discuss the generalization of our simple model to a more general class of Q-CNN's.

4.4.1 The CNN paradigm

The CNN, invented by L. O. Chua and L. Yang [53-54] and generalized in subsequent work [55-56], is a two or three dimensional, usually regular array of analogous cells. Each cell, indexed by κ, has dynamical state variables $\grave{x}_\kappa$, external inputs $\grave{u}_\kappa$, and internal constant cell data $\grave{z}_\kappa$. Each cell is influenced by its neighbors through a synaptic input I^s_κ which depends on the values of cell states and cell inputs within a sphere S_κ centered on cell κ. A *CNN synaptic law* describes the effect of other cells on the synaptic input:

$$I^s_\kappa = \sum_\lambda A^\lambda_\kappa \grave{x}_{\kappa+\lambda} + \sum_\lambda B^\lambda_\kappa f(\grave{x}_\kappa, \grave{x}_{\kappa+\lambda}) + \sum_\lambda C^\lambda_\kappa \grave{u}_{\kappa+\lambda} \ . \tag{4.32}$$

The cell dynamics are determined by a *CNN state equation* giving the rate of change of state variables as the *nonlinear* function of the state of the cell itself, the synaptic input from neighboring cells, and the external inputs:

$$\frac{\partial}{\partial t} \ \grave{x}_\kappa = -g(\grave{x}_\kappa, \grave{z}_\kappa, \grave{u}_\kappa, I^s_\kappa) . \tag{4.33}$$

If there no external inputs exist then the CNN is called *autonomous*. The CNN is then defined by (1) the synaptic law, (2) the state equation, (3) initial conditions, and (4) boundary conditions. Unlike neural networks in case of the CNN the cells are primarily *locally interconnected*, thus the practical realization is much easier, than in the case of a fully interconnected neural network.

4.4.2 Formulating quantum dynamics as CNN dynamics

The (4.13) and (4.14) cell state equations deduced in Section 4.1 have the (4.33)

form of CNN equations:

$$\hbar \frac{d}{dt}P = -2\gamma\sqrt{1-P^2}\sin\varphi ,\qquad (4.34)$$

$$\hbar \frac{d}{dt}\varphi = -\overline{P}E_k + 2\gamma\frac{P}{\sqrt{1-P^2}}\cos\varphi .\qquad (4.35)$$

The synaptic law is given by:

$$I^s = E_k\overline{P} = \sum_{\lambda \in S_\kappa} w(\mathbf{R}_\kappa - \mathbf{R}_\lambda)P_\lambda .\qquad (4.36)$$

The (4.13) and (4.14) equations are based on the Hartree-Fock intercellular

approximation.

This gives the exact dynamics if there are no quantum entanglements between cells.

Allowing correlation effects that produced mixed intercellular states would make

connecting to a CNN description impossible because of the need for local cell state

information. Moreover, in our simulations of dynamic switching of cellular arrays we

found that including the correlations between cells did not alter the qualitative behavior

(though it did increase the speed of the intercellular responses.)

Fig. 4.17 shows some simulation examples with two-dimensional arrays. In Fig.

4.17(a) the snapshots of circular wave propagation can be seen. The edges of a cell block

were periodically excited. Near the top left corner a block of cells were kept fixed causing

a disturbance in the wave propagation. In Figs. 4.17(b) and (c) snapshots of spiral wave

propagation can be seen. For simulation examples with a one-dimensional array see Sec.

4.3.
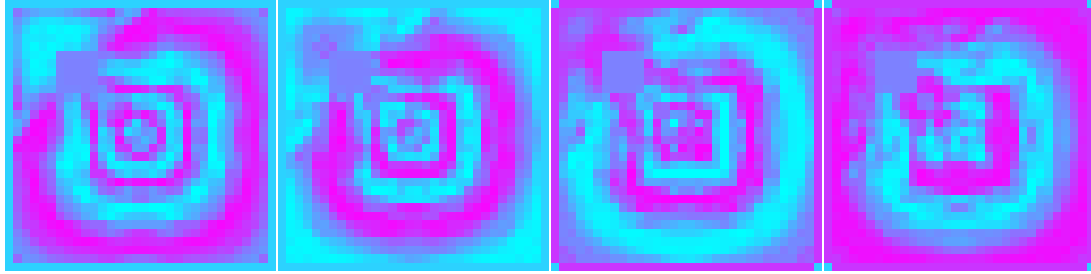
(a)
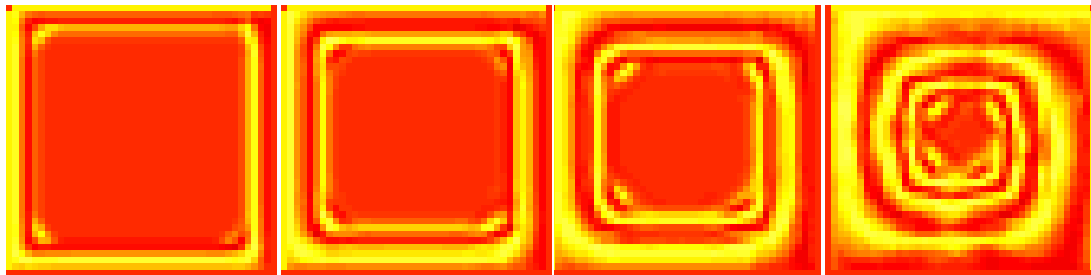
(b)
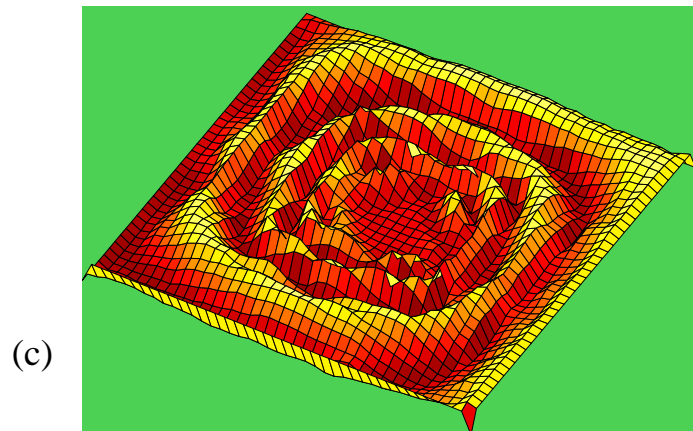
(c)

FIGURE 4.17. Circular and spiral waves in a two-dimensional array of QCA cells. (a) The edges are periodically excited. Near the top left corner a fixed cell block causes disturbances in the wave propagation. A pixel of a snapshot corresponds to a QCA cell. The color indicates a polarization between +1 (blue) and -1 (purple). (b) The edges are periodically excited, with a certain delay with respect to each other. Due to this delay spiral waves occur instead of circular waves. (c) The last snapshot of (b) is redrawn as a 3D graph.

4.4.3 Generalization of Quantum Cellular Neural Networks

Although we have employed a fairly simple model for demonstrating Q-CNN behavior, the general features of the paradigm are clear.

1. Each cell is a quantum system. The specification of the quantum system can distinguish N_c classical degrees of freedom and N_q quantum degrees of freedom.

2. *The interaction between cells, the synaptic input, depends only on the classical degrees of freedom. This corresponds to an intercellular Hartree-Fock approximation. The precise form of the synaptic law is determined by the physics of the intercellular interaction.*

3. *The state equations are derived from the time-dependent Schrödinger equation. One state equation exists for each classical and quantum degree of freedom.*

4.4.4 Conclusions

We have defined the Q-CNN paradigm and examined it in the case of a simple two-state model of the cell. The system is sufficiently rich to reproduce the wave propagation behavior seen in a fuller quantum treatment as demonstrated in Sec. 4.3. The general features of Q-CNN architecture have been outlined. Of particular interest is the distinction between information-bearing classical degrees of freedom and quantum degrees of freedom which are necessary for proper temporal evolution.

CHAPTER 5

QCA QUANTUM DYNAMICS USING THE COHERENCE VECTOR FORMALISM

In this chapter an alternative of the state vector description, the coherence vector formalism [57] is presented. It is equivalent to the density matrix description thus it can model mixed states and decoherence. Its other advantage is that the state variables can be divided into groups corresponding to the state of the individual cells, and to the two-point, three-point, etc. correlations. This is not possible with state vector or the density matrix description.

In Sec. 5.1 the dynamical equations of the coherence vector for many-cell systems are deduced. It is also shown how to interpret correlations in the framework of this formalism. In Sec.5.2 a particular application of the formalism, quantum computing with Quantum-dot Cellular Automata, is presented.

5.1 The coherence vector formalism

The state of a QCA cell, as a two-state system, can be given by a two-element state vector according to (4.8). Besides the state vector, a 2x2 element density matrix can also be used for state description. Its main advantage is the possibility of describing mixed states while the state vector description can be applied only for pure states. The dynamics

of the system can be given in terms of differential equations for the four complex elements of the density matrix (Liouville equation).

The method can be improved if we eliminate the redundant part of the density matrix. Although it has 4 complex (i.e., 8 real) elements, these elements are not independent from each other. The density matrix is Hermitian that means 4 constrains on the elements. Its trace is unity, that gives a further constraint. Thus the number of degrees of freedom is only 8-4-1=3. It means that the state of the ensemble can be given by 3 real numbers instead of the density matrix containing 4 complex numbers.

Our observation agrees with the theory[57] that says that the density matrix can be constructed as the linear combination of the generators of the *SU(2)* group, namely the $\hat{\sigma}_x$, $\hat{\sigma}_y$ and $\hat{\sigma}_z$ Pauli spin matrices and the unit matrix

$$\hat{\rho} \; = \; \frac{1}{2}(\hat{1} + \lambda_x\hat{\sigma}_x + \lambda_y\hat{\sigma}_y + \lambda_z\hat{\sigma}_z),\tag{5.1}$$

where the λ_a coefficients are the three elements of the so-called *coherence vector*. They can be obtained as the expectation values of the Pauli spin matrices:

$$\lambda_a \; = \; \langle\hat{\sigma}_a\rangle; \qquad a{=}x,y,z.\tag{5.2}$$

The coherence vector will be used for state description instead of the state vector or the density matrix in the next sections.

To get the time dependence of the coherence vector, first the time dependence of the Pauli spin operators must be acquired in the Heisenberg picture. Then the dynamical equations for the coherence vector elements can be obtained by taking the expectation values of both sides of the dynamical equations for the Pauli spin operators.

In the Heisenberg picture, the time dependence of an operator is:

$$i\hbar\frac{\partial}{\partial t}\hat{O} = [\hat{O}, \hat{H}].\tag{5.3}$$

The Hamiltonian for a single-cell interacting with a driver is:

$$\hat{H} = -\gamma\hat{\sigma}_x + \frac{E_k}{2}P_{driver}\hat{\sigma}_z.\tag{5.4}$$

The time dependence of the $\hat{\sigma}_x$ Pauli spin matrix can be obtained as

$$\frac{d\hat{\sigma}_x}{dt} = -\frac{i}{\hbar}[\hat{\sigma}_x, \hat{H}] = (-E_k)P_{driver}\hat{\sigma}_y.\tag{5.5}$$

(For the commutator relations of Pauli spin matrices see [57], (2.34) on p. 39 with (2.17) on p. 36.). Similar equations can be found for the time dependence of $\hat{\sigma}_y$ and $\hat{\sigma}_z$:

$$\frac{d\hat{\sigma}_y}{dt} = -\frac{i}{\hbar}[\hat{\sigma}_y, \hat{H}] = E_kP_{driver}\hat{\sigma}_x + 2\gamma\hat{\sigma}_z \text{ , and}\tag{5.6}$$

$$\frac{d\hat{\sigma}_z}{dt} = -\frac{i}{\hbar}[\hat{\sigma}_z, \hat{H}] = -2\gamma\hat{\sigma}_y.\tag{5.7}$$

Equations (5.5-5.7) can be written in matrix form as

$$\hbar\frac{d}{dt}\begin{bmatrix}\hat{\sigma}_x\\\hat{\sigma}_y\\\hat{\sigma}_z\end{bmatrix} = \begin{bmatrix}0 & -E_kP_{driver} & 0\\E_kP_{driver} & 0 & 2\gamma\\0 & -2\gamma & 0\end{bmatrix}\begin{bmatrix}\hat{\sigma}_x\\\hat{\sigma}_y\\\hat{\sigma}_z\end{bmatrix}.\tag{5.8}$$

Taking the expectation value of both sides yields to:

$$\hbar\frac{d}{dt}\vec{\lambda} = \begin{bmatrix}0 & -E_kP_{driver} & 0\\E_kP_{driver} & 0 & 2\gamma\\0 & -2\gamma & 0\end{bmatrix}\vec{\lambda}.\tag{5.9}$$

(5.9) can also be written in a very expressive form ([57], equations (3.57-58) on p. 194 and (3.100-103) on p. 200) as

$$\hbar\frac{d}{dt}\vec{\lambda} = \vec{\Gamma}\times\vec{\lambda},\tag{5.10}$$

where

$$\vec{\Gamma} = \begin{bmatrix} -2\gamma \\ 0 \\ E_k P_{driver} \end{bmatrix}, \tag{5.11}$$

and the cross denotes vector cross product. Here $\Gamma_i = Tr(\hat{\sigma}_i \hat{H})$ for $i=x,y,z$.

(5.10) is the dynamical equation of the cell, equivalent to the Liouville equation giving the time dependence of the single-cell density matrix. It describes the precession of the coherence vector around $\vec{\Gamma}$ as shown in Fig. 5.1.

If we were describing a spin-1/2 particle instead of a QCA cell then $\langle \hat{\sigma}_x \rangle, \langle \hat{\sigma}_y \rangle$ and $\langle \hat{\sigma}_z \rangle$ would correspond to the three coordinates of the spin. The dynamics of the spin would be given similarly to (5.10), however, the role of $\vec{\Gamma}$ would be played by the $\vec{B}$ magnetic field.

In case of a QCA cell the interpretation of $\vec{\Gamma}$ and $\vec{\lambda}$ is more difficult. $\vec{\lambda}$ describes the state of the cell while $\vec{\Gamma}$ describes the influences of the environment. The two main influences from the environment are the polarization of the driver cell and the interdot barrier height controlled by external electrodes. The third element of $\vec{\lambda}$ is related to the polarization of the cell as

$$P = -\langle \hat{\sigma}_z \rangle = \lambda_z. \tag{5.12}$$

The $P = \pm 1$ states correspond to $\vec{\lambda} = [0, 0, \mp 1]^T$. The other two elements of $\vec{\lambda}$ does not have such expressive interpretation.
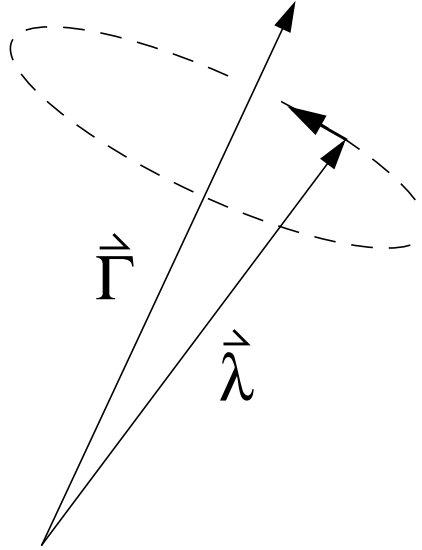
FIGURE 5.1. The dynamics of the $\vec{\lambda}$ coherence vector. It precesses around $\vec{\Gamma}$. $\vec{\lambda}$ describes the state of the cell while $\vec{\Gamma}$ describes the influences of the environment.

During the QCA cell-operation, if the barriers are high (γ=0) then $\vec{\Gamma}$ points to the +z or to the -z direction. In this case, if the cell is fully polarized ($\vec{\lambda} = [0, 0, \pm 1]^T$) then it remains in this state since $\vec{\Gamma} \parallel \vec{\lambda}$. When the barriers are extremely low ($\gamma \gg E_k$), $\vec{\Gamma}$ points to the -x direction.

As it was mentioned before, the density matrix description is able to handle mixed states. Unlike in pure states, in mixed states the ensemble contains systems being in different quantum mechanical states. If we restrict our attention to pure states, then length of the coherence vector remains unity[57]: $|\vec{\lambda}| = 1$.

5.1.1 Dynamical description of the state of two interacting QCA cells

The coherence vector formalism can also be used to describe multi-cell systems. The density matrix of a system of N cells has $2^N \mathrm{x} 2^N$ complex=$2 \mathrm{x} 2^{2N}$ real elements. $2^{2N} +1$ constraints are coming from the requirements of Hermiticity and unit trace that leaves $s=2^{2N}-1$ real degrees of freedom. Now density matrix can be given as the linear combination of the s generating operators of the SU(2^N) group:

$$\hat{\rho} = \frac{1}{2^N}\hat{1} + \frac{1}{2^N}\sum_{i=1}^{s}\lambda_i\hat{\lambda}_i \qquad (5.13)$$

For $N=2$ cells the $\hat{\lambda}_i$ basis operators are shown in Fig.5.2. There are three single-cell operators for the first cell, three single-cell operators for the second cell, and nine two-cell operators. The $s=15$ element coherence vector of the whole system contains their expectation values:

$$\vec{\lambda} = \begin{bmatrix} \vec{\lambda}(1) \\ \vec{\lambda}(2) \\ \vec{K}(1,2) \end{bmatrix}. \qquad (5.14)$$

Here $\vec{\lambda}(1)$ and $\vec{\lambda}(2)$ *single-cell coherence vectors* contain the expectation values of the single-cell operators. $\vec{K}(1,2)$ contains the *two-point correlations*, that is, the expectation

values of the two-cell operators. The two-point correlations are often placed instead of a

vector in a 3x3 matrix called the *correlation tensor.*.

$$\hat{\sigma}_x(1) \quad\quad \hat{\sigma}_y(1) \quad\quad \hat{\sigma}_z(1)$$

$$\hat{\sigma}_x(2) \quad\quad \hat{\sigma}_y(2) \quad\quad \hat{\sigma}_z(2)$$

Single-cell operators

$$\hat{\sigma}_x(1)\hat{\sigma}_x(2) \quad\quad \hat{\sigma}_x(1)\hat{\sigma}_y(2) \quad\quad \hat{\sigma}_x(1)\hat{\sigma}_z(2)$$
$$\hat{\sigma}_y(1)\hat{\sigma}_x(2) \quad\quad \hat{\sigma}_y(1)\hat{\sigma}_y(2) \quad\quad \hat{\sigma}_y(1)\hat{\sigma}_z(2)$$
$$\hat{\sigma}_z(1)\hat{\sigma}_x(2) \quad\quad \hat{\sigma}_z(1)\hat{\sigma}_y(2) \quad\quad \hat{\sigma}_z(1)\hat{\sigma}_z(2)$$

Two-cell operators

FIGURE 5.2. The *s*=15 basis operators for a two-cell system. There are three single-cell operators for the first cell, three single-cell operators for the second cell, and nine two-cell operators.

In summary, to describe the state of two QCA cells fully, besides the two 3 element

coherence vectors, a 3x3 element correlation tensor is needed as shown in Fig. 5.3. The

$$\vec{\lambda}(1) \quad\quad\quad\quad\quad\quad \vec{\lambda}(2)$$

$$\hat{K}(1, 2)$$
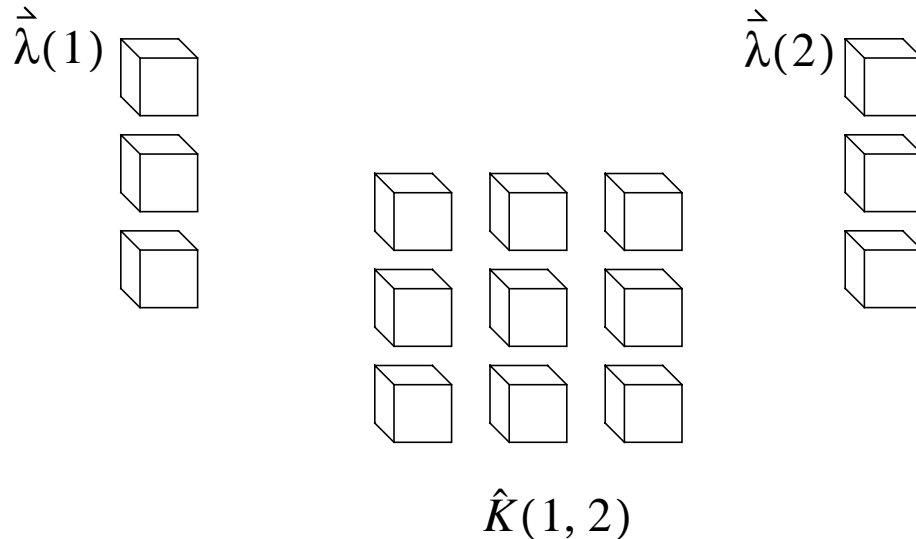
FIGURE 5.3. To describe the state of two interacting cells, beside the two coherence vectors, the correlation tensor is also necessary.

degrees of freedom describing the correlation between the two cells are more then the degrees of freedom describing the cell states. This is even more so, if the number of cells are increased.

Notice that when using the coherence vector formalism, the state variables can be divided into three groups. One group corresponds to the first cell, the second to the second cell, and the third group of variables describe the correlation of the two cells. This cannot be done so explicitly when using the state vector or the density matrix description. For these descriptions, when uniting two subsystems, the state variables describe the state of the whole quantum mechanical system.

To obtain information about the state of a subsystem further algebraic transformations are needed (e.g., reduced density matrices can be used to describe the state of a single cell.)

To get the dynamics of the coherence vector of the system, we need the Hamiltonian of two interacting cells:

$$\hat{H} = -\gamma_1 \hat{\sigma}_x(1) - \gamma_2 \hat{\sigma}_x(2) - \frac{E_k}{2} \hat{\sigma}_z(1) \hat{\sigma}_z(2). \tag{5.15}$$

According to (5.3) the time dependence of the Pauli spin matrices for the first and the second cells can be obtained as,

$$\hbar \frac{d}{dt} \begin{bmatrix} \hat{\sigma}_x(1) \\ \hat{\sigma}_y(1) \\ \hat{\sigma}_z(1) \end{bmatrix} = \begin{bmatrix} 0 & 0 & 0 \\ 0 & 0 & 2\gamma_1 \\ 0 & -2\gamma_1 & 0 \end{bmatrix} \begin{bmatrix} \hat{\sigma}_x(1) \\ \hat{\sigma}_y(1) \\ \hat{\sigma}_z(1) \end{bmatrix} + E_k \begin{bmatrix} \hat{\sigma}_y(1)\hat{\sigma}_z(2) \\ -\hat{\sigma}_x(1)\hat{\sigma}_z(2) \\ 0 \end{bmatrix}, \text{ and} \tag{5.16}$$

$$\hbar \frac{d}{dt} \begin{bmatrix} \hat{\sigma}_x(2) \\ \hat{\sigma}_y(2) \\ \hat{\sigma}_z(2) \end{bmatrix} = \begin{bmatrix} 0 & 0 & 0 \\ 0 & 0 & 2\gamma_2 \\ 0 & -2\gamma_2 & 0 \end{bmatrix} \begin{bmatrix} \hat{\sigma}_x(2) \\ \hat{\sigma}_y(2) \\ \hat{\sigma}_z(2) \end{bmatrix} + E_k \begin{bmatrix} \hat{\sigma}_y(2)\hat{\sigma}_z(1) \\ -\hat{\sigma}_x(2)\hat{\sigma}_z(1) \\ 0 \end{bmatrix}. \tag{5.17}$$

The dynamics of the coherence vectors can be obtained computing the expectation values of the right and left hand sides of (5.16) and (5.17):

$$\hbar \frac{d}{dt}\vec{\lambda}(1) = \hat{\Omega}_1\vec{\lambda}(1) + E_k\left[\langle\hat{\sigma}_y(1)\hat{\sigma}_z(2)\rangle - \langle\hat{\sigma}_x(1)\hat{\sigma}_z(2)\rangle \; 0\right]^T, \text{ and} \qquad (5.18)$$

$$\hbar \frac{d}{dt}\vec{\lambda}(2) = \hat{\Omega}_2\vec{\lambda}(2) + E_k\left[\langle\hat{\sigma}_y(2)\hat{\sigma}_z(1)\rangle - \langle\hat{\sigma}_x(2)\hat{\sigma}_z(1)\rangle \; 0\right]^T. \qquad (5.19)$$

where

$$\hat{\Omega}_i = \begin{bmatrix} 0 & 0 & 0 \\ 0 & 0 & 2\gamma_i \\ 0 & -2\gamma_i & 0 \end{bmatrix}. \qquad (5.20)$$

The $\langle\hat{\sigma}_y(1)\hat{\sigma}_z(2)\rangle$ and $\langle\hat{\sigma}_x(1)\hat{\sigma}_z(2)\rangle$ terms describe the *intercell quantum correlation*. Since they appear on the right hand side of the differential equations for the single-cell coherence vectors, their dynamics must be also computed, if one wants to know the dynamics of the single-cell coherence vectors.

The general form of a quantum correlation term is

$$K_{ab} = \langle\hat{\sigma}_a(1)\hat{\sigma}_b(2)\rangle; \qquad\qquad a, b = x, y, z . \qquad (5.21)$$

The 3x3=9 quantum correlation terms can be placed in a matrix, called the *correlation tensor*:

$$\hat{K} = \begin{bmatrix} K_{xx} & K_{xy} & K_{xz} \\ K_{yx} & K_{yy} & K_{yz} \\ K_{zx} & K_{zy} & K_{zz} \end{bmatrix}. \qquad (5.22)$$

The time dependence of the elements of the correlation tensor can be obtained from the commutator relation of (5.3):

$$\hbar\frac{d}{dt}\vec{K} = \begin{bmatrix} 0 & 0 & 0 & 0 & 0 & 0 & 0 & 0 & 0 \\ 0 & 0 & 2\gamma_2 & 0 & 0 & 0 & 0 & 0 & 0 \\ 0 & -2\gamma_2 & 0 & 0 & 0 & 0 & 0 & 0 & 0 \\ 0 & 0 & 0 & 0 & 0 & 0 & 2\gamma_1 & 0 & 0 \\ 0 & 0 & 0 & 0 & 0 & 2\gamma_2 & 0 & 2\gamma_1 & 0 \\ 0 & 0 & 0 & 0 & -2\gamma_2 & 0 & 0 & 0 & 2\gamma_1 \\ 0 & 0 & 0 & -2\gamma_1 & 0 & 0 & 0 & 0 & 0 \\ 0 & 0 & 0 & 0 & -2\gamma_1 & 0 & 0 & 0 & 2\gamma_2 \\ 0 & 0 & 0 & 0 & 0 & -2\gamma_1 & 0 & -2\gamma_2 & 0 \end{bmatrix} \vec{K} + E_k \begin{bmatrix} 0 \\ 0 \\ \lambda_y(1) \\ 0 \\ 0 \\ -\lambda_x(1) \\ \lambda_y(2) \\ -\lambda_x(2) \\ 0 \end{bmatrix}, \quad (5.23)$$

where the vector containing the nine elements of the correlation tensor is

$$\vec{K} = \begin{bmatrix} K_{xx} & K_{xy} & K_{xz} & K_{yx} & K_{yy} & K_{yz} & K_{zx} & K_{zy} & K_{zz} \end{bmatrix}^T. \quad (5.24)$$

(For further details see Appendix A.) It is possible to write (5.23) in a simpler form using the so-called direct product:

$$\hbar\frac{d}{dt}\vec{K} = (1 \otimes \hat{\Omega}_2 + \hat{\Omega}_1 \otimes 1)\vec{K} + E_k\begin{bmatrix} 0 & 0 & \lambda_y(1) & 0 & 0 & -\lambda_x(1) & \lambda_y(2) & -\lambda_x(2) & 0 \end{bmatrix}^T. \quad (5.25)$$

Up to now the correlation terms were placed in a nine element vector. Different formalism can be obtained if they are placed in a 3x3 tensor according to (5.23). With the correlation tensor (5.23) can be rewritten as

$$\hbar\frac{d}{dt}\hat{K} = \hat{\Omega}_2\hat{K} - \hat{K}\hat{\Omega}_1 + E_k\begin{bmatrix} 0 & 0 & \lambda_y(1) \\ 0 & 0 & -\lambda_x(1) \\ \lambda_y(2) & -\lambda_x(2) & 0 \end{bmatrix}. \quad (5.26)$$

Rewriting (5.16) and (5.17) with the correlation tensor elements, the equations for the two cells' coherence vectors are:

$$\hbar\frac{d}{dt}\vec{\lambda}(1) = \hat{\Omega}_1\vec{\lambda}(1) + E_k\begin{bmatrix} K_{yz} & -K_{xz} & 0 \end{bmatrix}^T, \quad (5.27)$$

and

$$\hbar \frac{d}{dt}\hat{\lambda}(2) \;=\; \hat{\Omega}_2 \hat{\lambda}(2) + E_k \begin{bmatrix} K_{zy} & -K_{zx} & 0 \end{bmatrix}^T. \tag{5.28}$$

(5.26), (5.27) and (5.28) are the dynamical equations for two coupled QCA cells. They can be found in [49] (Section 3.2.5.3, page 227) for a more general case, presented in terms of nested sums. We are following a slightly different path, using linear algebra that hopefully makes both the interpretation of these equations and their numerical applications easier.

Next a concrete simulation example is presented. The setup consists of two QCA cells where the first one is also coupled to a driver as shown in Fig, 5.4(a). The Hamiltonian is

$$\hat{H} \;=\; -\gamma_1 \hat{\sigma}_x(1) - \gamma_2 \hat{\sigma}_x(2) - \frac{E_k}{2}\hat{\sigma}_z(1)\hat{\sigma}_z(2) + \frac{E_k}{2} P_{driver}\hat{\sigma}_z(1). \tag{5.29}$$

The dynamical equation for this case can be obtained from (5.26), (5.27) and (5.28) with the following substitution:

$$\hat{\Omega}_1 \;=\; \begin{bmatrix} 0 & 0 & 0 \\ 0 & 0 & 2\gamma_1 \\ 0 & -2\gamma_1 & 0 \end{bmatrix} \rightarrow \hat{\Omega}'_1 \;=\; \begin{bmatrix} 0 & -E_k P_{driver} & 0 \\ E_k P_{driver} & 0 & 2\gamma_1 \\ 0 & -2\gamma_1 & 0 \end{bmatrix}. \tag{5.30}$$

Figs. 5.4(b-d) show the time evolution of the coherence vectors and the correlation tensor elements obtained from the numerical simulation of these dynamical equations. ($\hbar$ and E_k is taken to be 1 for simplicity.) The driver cell has -1 polarization. The time dependence of the interdot tunneling energy is shown in 5.4(b). As the barriers are gradually (quasi-adiabatically) raised the two cells align with the driver cell. Fig. 5.4(c) shows the time dependence of the three coordinates of the two coherence vectors. λ_{zj}'s change from 0 to 1 (remember that $P = -\lambda_z$), while λ_{xj}'s change from 1 to 0. λ_{yj}'s remain close to zero.
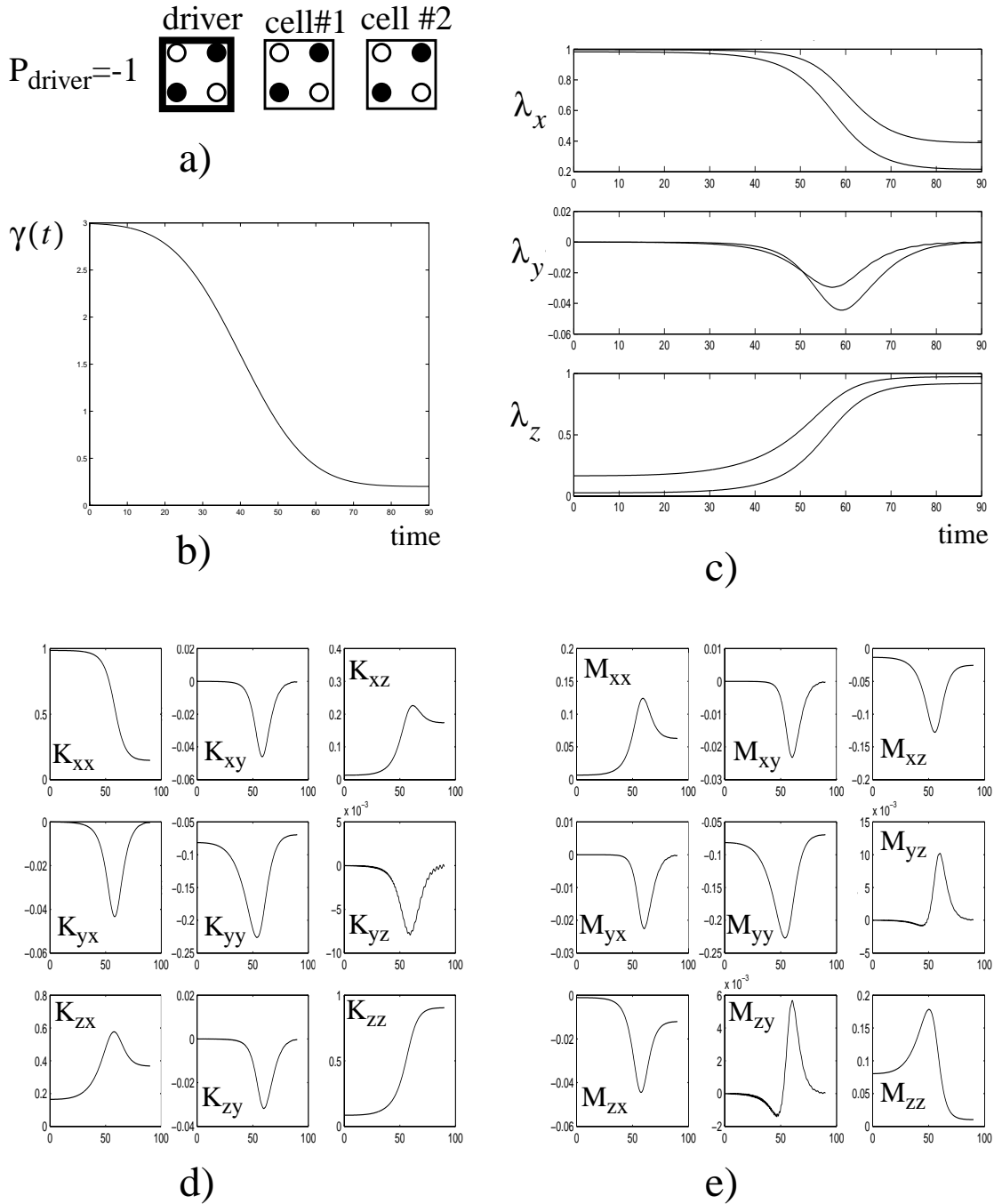
FIGURE 5.4. Adiabatic switching of two cells. The barriers are gradually lowered while the driver has constant -1 polarization. The two cells follow the polarization of the driver. (a) The arrangement of the two cells and a driver, (b) the dynamics of the interdot tunneling energy, (c) the elements of the two coherence vectors as the function of time, (d) the dynamics of the elements of the correlation tensor and (d) the dynamics of the elements of the correlation tensor proper.

If the barriers were raised even more gradually then the peak of λ_{yj}'s would be even smaller. Fig. 5.4(d) and (e) show the time dependence of the nine element correlation tensor and correlation tensor proper, respectively. The elements of the latter one start from zero and return to almost zero. If the process were fully adiabatic and the barriers were raised to infinity, the correlation tensor proper would be zero at the end.

5.1.2 Dynamical description of the state of a QCA cell line

In the general case of a system of N cells the $\hat{\lambda}_i$ basis operators have the form of

$$\left\{\begin{array}{c} \hat{1} \\ \hat{\sigma}_x(1) \\ \hat{\sigma}_y(1) \\ \hat{\sigma}_z(1) \end{array}\right\}\left[\begin{array}{c} \hat{1} \\ \hat{\sigma}_x(2) \\ \hat{\sigma}_y(2) \\ \hat{\sigma}_z(2) \end{array}\right]\left[\begin{array}{c} \hat{1} \\ \hat{\sigma}_x(3) \\ \hat{\sigma}_y(3) \\ \hat{\sigma}_z(3) \end{array}\right] \times \ldots \times \left\{\begin{array}{c} \hat{1} \\ \hat{\sigma}_x(N) \\ \hat{\sigma}_y(N) \\ \hat{\sigma}_z(N) \end{array}\right\}. \tag{5.31}$$

A basis operator can be constructed by choosing one operator from each column. (For example, possible basis operators are $\hat{\sigma}_x(1)\hat{\sigma}_y(2)\hat{\sigma}_x(3)$, $\hat{\sigma}_y(1)\hat{\sigma}_z(3)$ and $\hat{\sigma}_z(1)$.) There are 4^N ways to do that, however, choosing all ones is not counted. Thus the number of basis operators is $4^N\text{-}1\text{=}2^{2N}\text{-}1$. That is in agreement with the number of freedom of the density matrix that was obtained as $s\text{=}2^{2N}\text{-}1$ in Sec. 5.1.1.

The coherence vector now contains the single-cell coherence vectors, the pair-correlations and the higher order (three-point, four-point) correlation terms as well. The three-point correlations are the expectation values of the three-cell basis operators.

The dynamical equations for a cell inside a cell line are similar to (5.26-5.28) but now a cell has two neighbors. The equation for the dynamics of the coherence vector is:

$$\hbar\frac{d}{dt}\hat{\vec{\lambda}}(i) \ = \ \hat{\Omega}_i\hat{\vec{\lambda}}(i) + E_k\begin{bmatrix} K_{zy}(i-1,i) + K_{yz}(i,i+1) \\ -K_{zx}(i-1,i) - K_{xz}(i,i+1) \\ 0 \end{bmatrix} . \tag{5.32}$$

The dynamics of the pair correlation tensor is given as:

$$h\frac{d}{dt}\hat{K}(i,j) \ = \ \hat{\Omega}_j\hat{K}(i,j) - \hat{K}(i,j)\hat{\Omega}_i + E_k\hat{C}(i,j), \tag{5.33}$$

where $\hat{C}(i,j)$ is a matrix containing coherence vectors and third order correlations. For the nearest neighbor case ($j=i+1$) it is

$$\hat{C}(i,i+1) \ = \ \begin{bmatrix} 0 & 0 & \lambda_y(i) \\ 0 & 0 & -\lambda_x(i) \\ \lambda_y(i+1) & -\lambda_x(i+1) & 0 \end{bmatrix} + \tag{5.34}$$

$$\left\langle \begin{bmatrix} \sigma_x(i)\sigma_y(i+1) & -\sigma_x(i)\sigma_x(i+1) & 0 \\ \sigma_y(i)\sigma_y(i+1) & -\sigma_y(i)\sigma_x(i+1) & 0 \\ \sigma_z(i)\sigma_y(i+1) & -\sigma_z(i)\sigma_x(i+1) & 0 \end{bmatrix} \sigma_z(i+2) \right\rangle +$$

$$\left\langle \begin{bmatrix} \sigma_y(i)\sigma_x(i+1) & -\sigma_x(i)\sigma_x(i+1) & 0 \\ \sigma_y(i)\sigma_y(i+1) & -\sigma_x(i)\sigma_y(i+1) & 0 \\ \sigma_y(i)\sigma_z(i+1) & -\sigma_x(i)\sigma_z(i+1) & 0 \end{bmatrix}^T \sigma_z(i-1) \right\rangle .$$

The following three point correlations can be found on the right hand side of (5.34): *xyz*, *xxz*, *yyz*, *yxz*, *zyz*, *zxz*, *zyx*, *zxx*, *zyy* and *zxy*.

For further than nearest neighbors it is

$$\hat{C}(i,j) = \left\langle \begin{bmatrix} \sigma_x(i)\sigma_y(j) & -\sigma_x(i)\sigma_x(j) & 0 \\ \sigma_y(i)\sigma_y(j) & -\sigma_y(i)\sigma_x(j) & 0 \\ \sigma_z(i)\sigma_y(j) & -\sigma_z(i)\sigma_x(j) & 0 \end{bmatrix} (\sigma_z(j-1) + \sigma_z(j+1)) \right\rangle +$$

$$\left\langle \begin{bmatrix} \sigma_y(i)\sigma_x(j) & -\sigma_x(i)\sigma_x(j) & 0 \\ \sigma_y(i)\sigma_y(j) & -\sigma_x(i)\sigma_y(j) & 0 \\ \sigma_y(i)\sigma_z(j) & -\sigma_x(i)\sigma_z(j) & 0 \end{bmatrix}^T (\sigma_z(i-1) + \sigma_z(i+1)) \right\rangle . \qquad (5.35)$$

On the right hand side of (5.35) the following further four three point correlations terms show up: *zzy*, *zzx*, *yzz* and *xzz*. It is important to notice that of the 3x3x3=27 three point correlation terms only these 14 are explicitly in the dynamical equations of the pair correlations. For example, the *zzz* three-point correlation is not among them.

It can be seen that substituting $j=i+1$ into (5.34) and using the rules for the multiplication of Pauli spin matrices, (5.35) can be obtained.

The equations for a cell at the edges of the line are slightly different, however, giving them explicitly do not help our analysis. When these equations are used for numerical simulation, it is reasonable to generate the dynamical equations symbolically by a computer program able to handle Pauli spin matrices. (As an example, see Appendix B for the results of a MATLAB program calculating (5.34) and (5.35) symbolically.) From the symbolical form the actual numerical equations can be obtained substituting the numerical values for E_k and γ_i into them. With our complicated equation systems the manual computations could lead easily to errors, however, manual computations can sill be used to check the results of the program generating the equations symbolically.

Notice also that further equations are necessary to describe the state of the cell line giving the dynamics of the third, fourth, etc. order correlation terms. These are not given here, however, can be computed similarly as it was done for the dynamics of the two-point correlations.

5.1.3 The correlation tensor proper and the measures of correlation

Besides the correlation tensor there are other quantities characterizing the intercell correlation. The *correlation tensor proper* for two cells is defined as

$$M_{ab}(1, 2) = \left\langle \left[\hat{\sigma}_a(1) - \langle \hat{\sigma}_b(1) \rangle \right] \left[\hat{\sigma}_b(2) - \langle \hat{\sigma}_b(2) \rangle \right] \right\rangle;$$

$$a, b = x, y, z. \tag{5.36}$$

With coherence vector elements (5.36) can be rewritten as

$$M_{ab}(1, 2) = K_{ab}(1, 2) - \lambda_a(1)\lambda_b(2); \qquad a, b = x, y, z. \tag{5.37}$$

The elements of the correlation tensor proper are all zero if there is no correlation between the cells or they are *uncorrelated*.

EXAMPLE 5.1

Let us consider two fully polarized QCA cells described by the two-state wave function $\Psi = |1, 1\rangle$. The coherence vector and correlation tensor elements can be computed according to (5.2) and (5.21):

104

$$\vec{\lambda}(1) \;=\; \begin{bmatrix} 0 \\ 0 \\ -1 \end{bmatrix}, \qquad \vec{\lambda}(2) \;=\; \begin{bmatrix} 0 \\ 0 \\ -1 \end{bmatrix}, \qquad \hat{K}(1,2) \;=\; \begin{bmatrix} 0 & 0 & 0 \\ 0 & 0 & 0 \\ 0 & 0 & 1 \end{bmatrix}. \qquad (5.38)$$

The correlation tensor proper can be obtained using (5.36):

$$\hat{M}(1,2) \;=\; \begin{bmatrix} 0 & 0 & 0 \\ 0 & 0 & 0 \\ 0 & 0 & 0 \end{bmatrix}. \qquad (5.39)$$

Rather counter intuitively there is no correlation between the two aligned cells.

The same is true for $\Psi = |-1, -1\rangle$.

EXAMPLE 5.2

Let us consider the superposition of the two states mentioned in Example 5.1: $\Psi = |1, 1\rangle + |-1, -1\rangle$. The coherence vector and correlation tensor elements are

$$\vec{\lambda}(1) \;=\; \begin{bmatrix} 0 \\ 0 \\ 0 \end{bmatrix}, \qquad \vec{\lambda}(2) \;=\; \begin{bmatrix} 0 \\ 0 \\ 0 \end{bmatrix}, \qquad \hat{K}(1,2) \;=\; \begin{bmatrix} 1 & 0 & 0 \\ 0 & -1 & 0 \\ 0 & 0 & 1 \end{bmatrix} \qquad (5.40)$$

The correlation tensor proper now have non-zero elements.

$$\hat{M}(1,2) \;=\; \begin{bmatrix} 1 & 0 & 0 \\ 0 & -1 & 0 \\ 0 & 0 & 1 \end{bmatrix}. \qquad (5.41)$$

If the polarization of first cell is measured, the +1 and -1 results are equally probable. The same is true for the second cell. However, if both are

measured simultaneously then either both will have +1 or both will have -1 polarization.

It is instructive to examine the complementary example with $\Psi = |1, -1\rangle + |-1, 1\rangle$ for which $M_{zz} = -1$. If the cell polarizations are measured simultaneously, they will be opposite. $M_{zz} = 1$ indicated in the previous case that the two cells "tended to align", now $M_{zz} = -1$ indicates that they tend to anti-align.

EXAMPLE 5.3

Our last example is the superposition of the two state vectors mentioned in Example 5.2: $\Psi = |1, -1\rangle + |1, -1\rangle + |1, 1\rangle + |-1, -1\rangle$. The coherence vector and correlation tensor elements are

$$\vec{\lambda}(1) = \begin{bmatrix} 0 \\ 0 \\ 0 \end{bmatrix}, \qquad \vec{\lambda}(2) = \begin{bmatrix} 0 \\ 0 \\ 0 \end{bmatrix}, \qquad \hat{K}(1, 2) = \begin{bmatrix} 1 & 0 & 0 \\ 0 & 0 & 0 \\ 0 & 0 & 0 \end{bmatrix}. \qquad (5.42)$$

The $\hat{M}(1, 2)$ correlation tensor proper now has only zero elements. It describes an uncorrelated two-cell state. Note that $\Psi = |1, -1\rangle + |1, -1\rangle + |1, 1\rangle + |-1, -1\rangle$ can be written as a product of two single-cell states: $\Psi = (|1\rangle + |-1\rangle)(|1\rangle + |-1\rangle)$. If this can be done for a two-cell state, then the two cells are uncorrelated.

It is also useful to have a simple scalar measure instead of a matrix to characterize intercell correlation (See [57], equation (2.683) in on page 145). This can be some norm of $\hat{M}$, preferably

$$\beta = Tr(\hat{M}\hat{M}^H) = \sum_{a,b}|M_{ab}|^2. \qquad (5.43)$$

If one of the two cells is fully polarized ($\vec{\lambda}$=(0,0,+1) or (0,0,-1)) then the $\hat{M}$ correlation tensor proper is zero. In this case the two cells are uncorrelated.

The higher order correlation tensors proper are defined similarly to (5.36). For example, the three-point correlation proper (see [57], equations (2.810-811), page 168) can be given as

$$M_{abc}(1,2,3) = \left\langle \left[\hat{\sigma}_a(1) - \langle\hat{\sigma}_a(1)\rangle\right]\left[\hat{\sigma}_b(2) - \langle\hat{\sigma}_b(2)\rangle\right]\left[\hat{\sigma}_c(3) - \langle\hat{\sigma}_c(3)\rangle\right]\right\rangle;$$

$$a, b, c = x, y, z$$
$$(5.44)$$

After some algebraic transformations one gets

$$M_{abc}(1,2,3) = K_{abc}(1,2,3) - K_{ab}(1,2)\lambda_c(3) - K_{ac}(1,3)\lambda_b(2) -$$
$$K_{bc}(2,3)\lambda_a(1) + 2\lambda_a(1)\lambda_b(2)\lambda_c(3);$$

$$a, b, c = x, y, z. \qquad (5.45)$$

There are 3x3x3=27 elements of a three-point correlation tensor and tensor proper.

EXAMPLE 5.4

The $\Psi = |1, 1, 1\rangle - |-1, -1, -1\rangle$ three-cell state is known as Greenberger-Horne-Zeilinger(GHZ; see [57] Section 2.5.3.5, page 175) state. In this example the coherence vector elements and the correlations

will be computed for the GHZ state. The coherence vectors and the two-point correlation tensors and tensor propers are:

$$\vec{\lambda}(1) = \vec{\lambda}(2) = \vec{\lambda}(3) = \begin{bmatrix} 0 \\ 0 \\ 0 \end{bmatrix}, \tag{5.46}$$

$$\hat{K}(1,2) = \hat{K}(2,3) = \hat{K}(1,3) = \hat{M}(1,2) = \hat{M}(2,3) = \hat{M}(1,3) = \begin{bmatrix} 0 & 0 & 0 \\ 0 & 0 & 0 \\ 0 & 0 & 1 \end{bmatrix}$$
$$. \tag{5.47}$$

The non-zero elements of the three-point correlation tensor are

$$\hat{K}_{xxx}(1,2,3) = -1,$$

$$\hat{K}_{yyx}(1,2,3) = \hat{K}_{yxy}(1,2,3) = \hat{K}_{xyy}(1,2,3) = 1. \tag{5.48}$$

The $\hat{M}(1,2,3)$ three-point correlation proper has the same non-zero elements.

EXAMPLE 5.5

After examining the GHZ state in the previous example, it is instructive to make the same computations for the $\Psi = |1, 1, 1\rangle - |-1, -1, 1\rangle$ three-cell state. The coherence vectors and the two-point correlation tensors and tensor propers are:

$$\vec{\lambda}(1) = \vec{\lambda}(2) = \begin{bmatrix} 0 \\ 0 \\ 0 \end{bmatrix}, \vec{\lambda}(3) = \begin{bmatrix} 0 \\ 0 \\ 1 \end{bmatrix}, \tag{5.49}$$

$$\hat{K}(1,3) = \hat{M}(1,3) = \hat{K}(2,3) = \hat{M}(2,3) = \begin{bmatrix} 0 & 0 & 0 \\ 0 & 0 & 0 \\ 0 & 0 & 0 \end{bmatrix}, \tag{5.50}$$

$$\hat{K}(1, 2) = \hat{M}(1, 2) = \begin{bmatrix} -1 & 0 & 0 \\ 0 & 1 & 0 \\ 0 & 0 & 1 \end{bmatrix}.$$ (5.51)

Not surprisingly, the third cell is not correlated with the other two.

The non-zero elements of the three-point correlation tensor are

$$\hat{K}_{xxz}(1, 2, 3) = -1, \hat{K}_{yyz}(1, 2, 3) = 1, \hat{K}_{zzz}(1, 2, 3) = 1.$$ (5.52)

The $\hat{M}(1, 2, 3)$ three-point correlation tensor proper contains only zeros.

5.1.4 The energy of a cell block

The average energy will be computed as the expectation value of the Hamiltonian operator: The expression obtained for the energy contains only two-point, and not higher order correlation terms. The energy expression will be interpreted through examples.

The Hamiltonian of a cell line of N cells, having a driver connected to the first cell is

$$\hat{H} = -\gamma \sum_{i=1}^{N} \hat{\sigma}_x(i) - \frac{E_k}{2} \sum_{i=1}^{N-1} \hat{\sigma}_z(i)\hat{\sigma}_z(i+1) + \frac{E_k}{2} P_{driver} \hat{\sigma}_z(1).$$ (5.53)

The expectation value of (5.53) is:

$$E = \langle \hat{H} \rangle = -\gamma \sum_{i=1}^{N} \langle \hat{\sigma}_x(i) \rangle - \frac{E_k}{2} \sum_{i=1}^{N-1} \langle \hat{\sigma}_z(i)\hat{\sigma}_z(i+1) \rangle + \frac{E_k}{2} P_{driver} \langle \hat{\sigma}_z(1) \rangle.$$ (5.54)

It can be expressed with the coherence vector and correlation tensor components as

$$E = \langle \hat{H} \rangle = -\gamma \sum_{i=1}^{N} \lambda_x(i) - \frac{E_k}{2} \sum_{i=1}^{N-1} K_{zz}(i, i+1) + \frac{E_k}{2} P_{driver} \lambda_z(1).$$ (5.55)

Due to the structure of the Hamiltonian, the average energy depends only on the coherence vector elements and on the two-point zz correlations, and not on higher order correlations.

According to (5.37) $K_{zz}(i,i+1)$ can be expressed with $M_{zz}(i,i+1)$, P_i and $P_{i+}1$:

$$K_{zz}(i, i+1) = \lambda_z(i)\lambda_z(i+1) + M_{zz}(i, i+1) = P_iP_{i+1} + M_{zz}(i, i+1). \quad (5.56)$$

Substituting this into (5.55) one obtains:

$$E = -\gamma\sum_{i=1}^{N}\lambda_x(i) - \frac{E_k}{2}\sum_{i=1}^{N-1}(P_iP_{i+1} + M_{zz}(i, i+1)) + \frac{E_k}{2}P_{driver}\lambda_z(1). \quad (5.57)$$

The (5.57) form of the energy expression is very instructive. The first term describes the energy coming from the non-zero tunneling energy. The second term in the right hand side of (5.57) describes the intercell coupling energy. The third term describes the effect of the driver cell on the first cell. If the first is aligned with the driver ($\lambda_z(1)=-P_{driver}$) then this energy term is negative. If they are anti-aligned then this term is positive.

EXAMPLE 5.6

Consider two interacting QCA cells. Let us suppose that the barriers are infinite high ($\gamma=0$) and the driver polarization is zero for simplicity. The energy of the two cells in this case is:

$$E = -\frac{E_k}{2}P_1P_2 - \frac{E_k}{2}M_{zz}(1, 2). \quad (5.58)$$

In the uncorrelated case $M_{zz}(1,2)=0$. If the two fully polarized cells have the same polarization ($P_i=P_{i+1}=+1$), then the energy of these two cells will be $-\frac{E_k}{2}$. If they have opposite polarization ($P_i=-P_{i+1}=+1$), the

110

corresponding energy will be $+\dfrac{E_k}{2}$. Thus if the cells are aligned with each other it decreases their energy.

However, it is also possible that the two cells have $-\dfrac{E_k}{2}$ energy even if their polarizations are zero. An example for that is the $\Psi = |1, 1\rangle + |-1, -1\rangle$ two-cell state for which $P_1=P_2=0$ and $M_{zz}(1,2)=+1$. The classical analogy of this state is two cells which are alternating their polarization between +1 and -1 in such a way that one has always the same polarization as the other. It is not difficult to see that energetically this is the same case as they both had constant +1 or -1 polarization.

5.1.5 Stationary solution of the dynamical equations

The (two-point, three-point, etc.) coherence vectors and correlation tensors describing the stationary states can be obtained by solving the dynamical equations taking the time derivatives zero. (The dynamical equations for the coherence vectors and the two-point correlations are (5.32-5.35). The equations for higher order correlations are not given here.) This way a system of algebraic equation is obtained. If the system is in pure state, further constraints are:

$$Tr(\hat{\rho}^n) \;=\; 1 \,;\, n=(1,2, \dots ,n). \tag{5.59}$$

Without these additional constrains, the stationary equations obtained from the dynamical ones cannot be solved, since the equations are not independent.

In mixed state, if additional damping terms are inserted in the dynamical equations, the stationary solution can be obtained without further constrains since the equations are now independent. From the point of view of the numerical computations this case is much better, since it is not necessary to compute the density matrix of the whole system, as it were needed in a pure state. Thus it is reasonable to add even small damping terms to the undamped equations in order to be able to determine the steady state easily. (For these damping terms see 5.1.7.)

5.1.6 The Hartree-Fock intercellular approximation applied for the coherence vector formalism

It is possible to apply both the coherence vector formalism and the Hartree-Fock intercellular approximation (see Sec. 4.1) to describe the state dynamics of a multi-cell structure. The Hartree-Fock model ignores all the correlations thus the number of state variables is radically decreased.

Using Hartree-Fock intercellular approximation, the dynamics of the multi cell system is given in terms of coupled single cell Scrödinger equations (Sec. 4.1). The differential equation of the jth cell is

$$i\hbar\frac{\partial}{\partial t}|\psi_j\rangle \,=\, \hat{H}_j|\psi_j\rangle,\tag{5.60}$$

where Hamiltonian matrix is

$$\hat{H}_j \,=\, \begin{bmatrix} -\frac{1}{2}\bar{P}_jE_k & -\gamma_j \\ -\gamma_j & \frac{1}{2}\bar{P}_jE_k \end{bmatrix} \,=\, -\gamma_j\hat{\sigma}_x(j) + \frac{E_k\bar{P}_j}{2}\hat{\sigma}_z(j).\tag{5.61}$$

$\bar{P}$ is the sum of the polarizations of the neighbors. Notice that the Hamiltonian is the size of 2x2 and the state vector has two elements.

Similarly to the deduction (5.3-5.10) one can get single cell dynamical equations, based on the Hartree-Fock approximation, for the single cell coherence vectors:

$$\hbar \frac{d}{dt} \vec{\lambda}(j) = \vec{\Gamma}(j) \times \vec{\lambda}(j), \tag{5.62}$$

where

$$\vec{\Gamma}(j) = \begin{bmatrix} -2\gamma_j \\ 0 \\ E_k \bar{P}_j \end{bmatrix}. \tag{5.63}$$

(5.62) and (5.63) describe the state dynamics of the cell equivalently to the single cell Scrödinger equation. In stationary states the right hand side of (5.62) must be zero. This is the case if $\vec{\Gamma}(j) \parallel \vec{\lambda}(j)$. Notice that $\vec{\lambda}(j)$ single cell coherence vectors are not coupled to two-point correlations as in (5.32).

It is possible to obtain (5.62) and (5.63) from the (5.32) exact dynamical equation for the coherence vector assuming that there are no intercell correlations. In this case

$$M_{zy}(i-1, i) = K_{zy}(i-1, i) - \lambda_z(i-1)\lambda_y(i) = 0. \tag{5.64}$$

Hence $K_{zy}(i-1, i) = \lambda_z(i-1)\lambda_y(i)$. Similar equations stand for K_{yz}, K_{zx} and K_{xz}. Substituting these into (5.32) one obtains:

$$\hbar \frac{d}{dt} \vec{\lambda}(i) = \begin{bmatrix} 0 & 0 & 0 \\ 0 & 0 & 2\gamma_i \\ 0 & -2\gamma_i & 0 \end{bmatrix} \vec{\lambda}(i) + E_k \begin{bmatrix} (\lambda_z(i-1) + \lambda_z(i+1))\lambda_y(i) \\ -(\lambda_z(i-1) + \lambda_z(i+1))\lambda_z(i) \\ 0 \end{bmatrix}. \tag{5.65}$$

It can be rewritten as

$$\hbar \frac{d}{dt} \vec{\lambda}(i) \; = \; \begin{bmatrix} 0 & E_k \bar{P} & 0 \\ -E_k \bar{P} & 0 & 2\gamma_i \\ 0 & -2\gamma_i & 0 \end{bmatrix} \vec{\lambda}(i), \tag{5.66}$$

with

$$\bar{P} \; = \; -(\lambda_z(i-1) + \lambda_z(i+1)). \tag{5.67}$$

(5.62) and (5.63) can be obtained transforming the matrix product into a vector product. The energy of the jth cell is the expectation value of the Hamiltonian of the cell:

$$E_j \; = \; \langle \hat{H}_j \rangle \; = \; -\gamma_j \langle \hat{\sigma}_x(j) \rangle + \frac{E_k \bar{P}_j}{2} \langle \hat{\sigma}_z(j) \rangle \; = \; -\gamma_j \lambda_x(j) + \frac{E_k \bar{P}_j}{2} \lambda_z(j). \tag{5.68}$$

It can be expressed in an instructive form with $\vec{\Gamma}(j)$ and $\vec{\lambda}(j)$:

$$E_j \; = \; \langle \hat{H}_j \rangle \; = \; \frac{1}{2} \vec{\Gamma}(j) \vec{\lambda}(j). \tag{5.69}$$

From (5.69) it follows that the energy for a given $\vec{\Gamma}(j)$ is minimal if $\vec{\Gamma}(j) \parallel \vec{\lambda}(j)$ and they are opposite in direction:

$$\vec{\lambda}(j) \; = \; -\frac{\vec{\Gamma}(j)}{\left| \vec{\Gamma}(j) \right|}. \tag{5.70}$$

Notice that since $\vec{\Gamma}(j)$ and $\vec{\lambda}(j)$ are parallel, this is a *stationary state*.

5.1.7 Modeling dissipation with the coherence vector formalism

The model presented in the previous subsections, describes the unitary time evolution of the cell line. Inserting damping terms in the differential equations for the coherence vector and correlation tensor elements, dissipation can also be included in the dynamics. (See Section 3.3.7.3. in [57]). The (5.32) differential equation for the coherence vector changes in the following way:

$$\frac{d}{dt}\vec{\lambda}(i)\big|_{diss} - \frac{d}{dt}\vec{\lambda}(i)\big|_{nd} = diag(\vec{\xi}_i)\vec{\lambda}(i) + \vec{\eta}_i. \tag{5.71}$$

where *diss* and *nd* stand for dissipative and non-dissipative. The three element vector $\vec{\xi}_i$ describes the dissipation rate for the three coordinates of the coherence vector. It has usually negative elements. $diag(\vec{\xi}_i)$ denotes a matrix with the elements of $\vec{\xi}_i$ in its diagonal. Vector $\vec{\eta}_i$ accounts for the fact that the dissipation drives the coherence vector elements to non-zero values.

The (5.33) differential equation for the correlation tensor change in the following way:

$$\frac{d}{dt}\hat{K}(i,j)\big|_{diss} - \frac{d}{dt}\hat{K}(i,j)\big|_{nd} = diag(\vec{\xi}_j)\hat{K}(i,j) + \hat{K}(i,j)diag(\vec{\xi}_i) + \vec{\eta}_i\vec{\lambda}^T(j) + \vec{\lambda}(i)\vec{\eta}_j^T \tag{5.72}$$

There are several possibilities to choose the $\vec{\xi}_i$ and $\vec{\eta}_i$ vectors depending on what kind of model of dissipation is used. One possibility [92] is the following. Let $\vec{\xi}_i$ be a vector of three negative numbers describing the damping rate. The instantaneous ground state with no dissipation according to the mean field type model (using Hartree-Fock approximation) described in [92] is

$$\vec{\lambda}_{ss}(i) = -\frac{\vec{\Gamma}_i}{\left|\vec{\Gamma}_i\right|}, \tag{5.73}$$

where

$$\vec{\Gamma}_i = \begin{bmatrix} -2\gamma \\ 0 \\ E_k\bar{P}_i \end{bmatrix}. \tag{5.74}$$

$\bar{P}_i$ the sum of the polarizations of the cell's neighbors. $\vec{\eta}_i$ can be chosen as

$$\vec{\eta}_i = -\vec{\xi}_j\vec{\lambda}_{ss}(i) = \vec{\xi}_j\frac{\vec{\Gamma}_i}{\left|\vec{\Gamma}_i\right|}. \tag{5.75}$$

115

Modeling the dissipation this way, describes the relaxation of the coherence vector towards $\vec{\lambda}_{ss}$.

5.2 An application of the coherence vector formalism: Quantum computing with Quantum-dot Cellular Automata

Quantum computing [58-90] has attracted attention in the last two decades because it was found that computers exploiting quantum mechanics are able to outperform classical digital computers in certain areas (factoring integers [83], searching [64,86]). Beside designing and analyzing new quantum computing algorithms, significant effort has been taken to find a suitable realization for a quantum computer. With the application of nuclear magnetic resonance (NMR) several groups have created quantum computers [67,68,69,75,76] up to the size of 5 qubits. Other implementations employ ion traps [84], cavity QED [85], Josephson junctions [87-90] and semiconductor quantum-dots [70,77-82].

We propose a multi quantum-dot structure, Quantum-dot Cellular Automata (QCA) [1-8] and investigate the basic quantum gates suitable for this implementation. Information is encoded in the position of the electrons inside the QCA cell. The basic single- and multi-qubit operations can be realized by lowering and raising the interdot tunneling barriers. Several other realizations have been proposed using semiconductor quantum dots. The information can be encoded in the electron spin [78,82], in the position of the electron in the double-dot [77,81], or the ground state and excited state of the electron can be used for logical "0" and "1" [79,80]. The quantum computing algorithms are performed by manipulating the interdot coupling with magnetic field [78], optically by

116

laser pulses [77,78,80] or by using external electrodes to raise and lower the interdot barriers [78,81,82].

QCA [1-8] was originally proposed as a transistorless alternative for digital circuit technology at nanoscale. The cells of digital QCA are mostly fully polarized during the operation. Dissipation plays a positive role helping the system to stay near the ground state.

The aim of our paper is to explore the possibilities of using semiconductor QCA for quantum computing. In the case of quantum computing, the cells are not fully polarized: they can be in a superposition of the P=+1 and P=-1 basis states. Similarly, a cell line can be in a superposition of the multi-qubit product states. Unlike digital applications, quantum computing ideally needs coherence for correct operation. (In real systems decoherence is always present thus its effects must be circumvented by error correction.) In order to distinguish QCA applied for quantum computing from digital QCA, the notion of coherent QCA (C-QCA) will be used.

In Sec. II the C-QCA cell line is used as a quantum register. In Sec. III and Sec. IV the single- and multi-qubit operations are presented. In Sec V. the decoherence and other issues pertaining to the physical realization are discussed.

5.2.1 The C-QCA cell line as a quantum register

An N qubit register can be realized with a line of N C-QCA cells as shown in Fig. 5.5. The γ_j interdot tunneling energy is set by external electrodes that lower or raise the interdot barriers of the jth cell. A cell can be turned off by lowering the barriers. (When a cell's barriers are extremely low, it does not have a definite polarization and it does not

affect its neighbors.) Each cell is Coulombically coupled to its left and right neighbors and to the bias electrodes. The $P_{bias,j}$ biases are set externally, thus these and the γ_j's are the inputs of the quantum register.
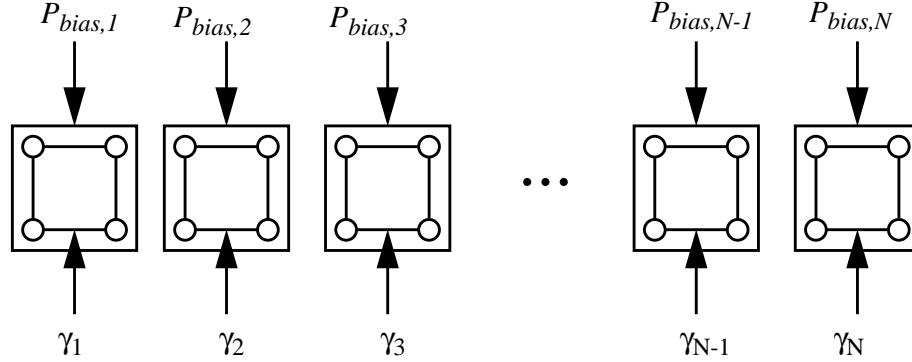
FIGURE 5.5. The *N* qubit register realized with a line of *N* C-QCA cells. Each cell has two inputs: the γ_j interdot tunneling energy and the $P_{bias,j}$ bias polarization.

There are three main steps when executing a program on the quantum register: writing in the initial state, running the algorithm and reading out the final state. The initial state can be loaded into the register by setting the biases to $\left| P_{bias,\,j} \right| \gg 1$ and waiting for a time sufficient to settle in the ground state. If $P_{bias,\,j} \gg 1$ ($P_{bias,\,j} \ll -1$) then the cell is forced to the P=+1 (P=-1) state. The execution of the algorithm is realized with a series of pulses applied to the electrodes of the cell. The final state can be read out by electrometers that are sensitive enough to detect the presence or the absence of an electron (e.g., single electron transistor [15-17]).

The C-QCA cell can be reasonably approximated as a two-state system [7]. The Hamiltonian for a line of *N* C-QCA cells is

$$\hat{H} = -\sum_{j=1}^{N} \gamma_j \hat{\sigma}_x(j) - \sum_{j=1}^{N-1} E_j \hat{\sigma}_z(j)\hat{\sigma}_z(j+1) + \sum_{j=1}^{N} E_0 P_{bias,\,j} \hat{\sigma}_z(j). \qquad (5.76)$$

Here E_j is the strength of Coulombic coupling between the jth and the $(j+1)^{st}$ cell. For

reasons explained later, its is alternating between E_0 and $2E_0$:

$$E_j = \left(\begin{array}{l} E_0, \text{ if j is odd} \\ 2E_0, \text{ if j is even.} \end{array} \right. \tag{5.77}$$

Hamiltonian (5.76) is isomorphic to that of an Ising spin chain in a transverse magnetic

field. The E_j and γ_j terms play the role of the interaction energy and the transverse

magnetic field strength, respectively. Only nearest neighbor coupling is considered

because for coupled electric quadrupoles the strength of the Coulombic interaction is

inversely proportional to the fifth power of the distance. The γ_j and $P_{bias,j}$ are setable,

however, the E_j intercell coupling is constant. Thus during a one-, two- or three-qubit

operation, the intercell coupling cannot be turned off in the rest of the cell line.

The polarization of the jth cell can be obtained as the expectation value of the $\hat{\sigma}_z$

operator:

$$P_j = -\langle \hat{\sigma}_z(j) \rangle . \tag{5.78}$$

With the minus sign we follow the convention of Ref. 57 in defining the Pauli spin

matrices:

$$\hat{\sigma}_x = \begin{bmatrix} 0 & 1 \\ 1 & 0 \end{bmatrix}, \hat{\sigma}_y = \begin{bmatrix} 0 & i \\ -i & 0 \end{bmatrix}, \text{ and } \hat{\sigma}_z = \begin{bmatrix} -1 & 0 \\ 0 & 1 \end{bmatrix}. \tag{5.79}$$

It is possible to give an effective Schrödinger equation for a single cell using the

mean-field approximation (See Ref. 52; these equations can be obtained from the Hartree-

Fock approximation applied to the C-QCA line as a many electron system):

$$\hat{H} = -\gamma \hat{\sigma}_x - E_\Sigma \hat{\sigma}_z , \tag{5.80}$$

where

$$E_\Sigma = E_{left}P_{left} + E_{right}P_{right} + E_0 P_{bias}. \tag{5.81}$$

The cell is coupled to its left and right neighbors through $E_{left}P_{left}$ and $E_{right}P_{right}$. (One of E_{left} and E_{right} is E_0, the other is $2E_0$.) The edge cells does not have left or right neighbors thus for them the corresponding polarizations are taken to be zero.

The state vector of a cell can be given as the linear combination of the fully polarized $P=+1$ and $P=-1$ basis states:

$$|\Psi\rangle = \alpha|1\rangle + \beta|-1\rangle = \begin{bmatrix} \alpha \\ \beta \end{bmatrix}. \tag{5.82}$$

Thus the state of a cell is described by two complex numbers, α and β.

The density matrix can also be used to describe the state of a single cell. The main advantage of the density matrix is that it can be used to describe energy dissipation although such dissipation will not be considered now. The dynamics of the density matrix are given by the Liouville equation:

$$i\hbar \frac{\partial}{\partial t}\hat{\rho} = [\hat{H}, \hat{\rho}]. \tag{5.83}$$

The density matrix can be expressed as the linear combination of the *SU(2)* generators, which are the Pauli spin matrices and the unit matrix:

$$\hat{\rho} = \frac{1}{2}(\hat{1} + \lambda_x\hat{\sigma}_x + \lambda_y\hat{\sigma}_y + \lambda_z\hat{\sigma}_z), \tag{5.84}$$

where $\lambda_a = \langle\hat{\sigma}_a\rangle$ for $a=x, y, z$. It can be seen from (5.84) that the three real λ_a values contain the same information about the quantum mechanical state as the 2x2 density matrix does. In other words, although the density matrix has four complex (=eight real) elements, it has only three (real) degrees of freedom, due to the constraints of Hermiticity and unit trace. The $\vec{\lambda}$ vector constructed from the three λ_a values is called the *coherence vector* (or the Bloch vector). The fully polarized $P=+1$ state corresponds to $\vec{\lambda}=[0,0,-1]^T$

and the P=-1 state corresponds to $\vec{\lambda}=[0,0,+1]^T$. In general, the third coordinate of $\vec{\lambda}$ equals -P.

The dynamical equation of the coherence vector is given as [57]:

$$\frac{d\vec{\lambda}}{dt} = \vec{\Gamma}\times\vec{\lambda},$$
(5.85)

where the cross denotes a vector product and $\Gamma_i = Tr(\hat{\sigma}_i\hat{H})$ for i=x,y,z. ($\hat{H}$ is given in (5.80).) For the C-QCA cell $\vec{\Gamma}$ is:

$$\hbar\vec{\Gamma} = \begin{bmatrix} -2\gamma \\ 0 \\ 2E_\Sigma \end{bmatrix}.$$
(5.86)

Equation (5.85) describes the precession of the coherence vector around $\vec{\Gamma}$. If there is no dissipation, the length of the coherence vectors remains unity. In the case of dissipation further terms are added to the right hand side of (5.85). The coherence vector describes the state of the cell, while $\vec{\Gamma}$ represents the influence of the environment. $\vec{\Gamma}_x$ depends on the barrier height. $\vec{\Gamma}_z$ represents the coupling to the bias cell and to the neighbors.

If there is no entanglement during the operation (the register remains in a quantum mechanical product state) then the mean-field description gives the same dynamics for the coherence vector as the full Hamiltonian model does.

Besides the coherence vector description, the quantum gates presented here will also be given by the unitary time evolution matrices computed from the many-cell Hamiltonian of the gates. They fully describe the functionality of the gate while the coherence vector description is used for making the design of quantum gates clearer.

5.2.2 Single qubit rotations

We consider the elementary single qubit rotations in λ-space. If $\gamma \gg E_k$ (the barriers are low) and $P_{bias}=0$ then $\hbar\vec{\Gamma} \cong [-2\gamma,0,0]^T$ which causes $\vec{\lambda}$ to precess around the $-x$ axis as shown in Fig. 5.6. (It is assumed that $\gamma=0$ for all the other cells.) The duration of the
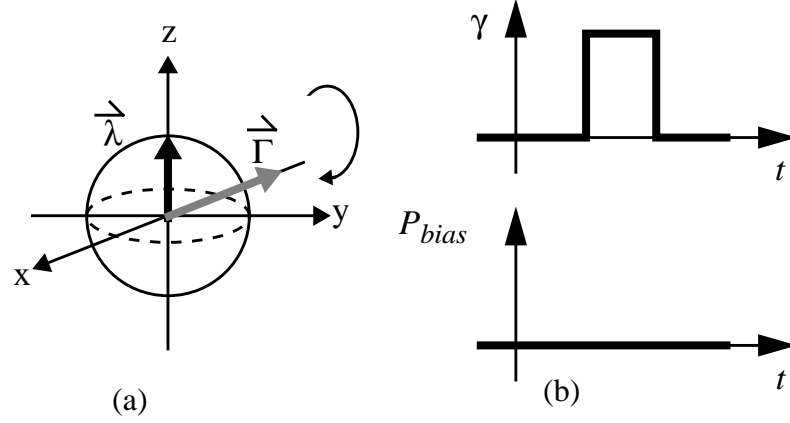
FIGURE 5.6. Rotation around the $-x$ axis. (a) The rotation in the λ-space. $\gamma \gg E_k$ (the barriers are low) and $P_{bias}=0$ thus $\hbar\vec{\Gamma}=[-2\gamma,0,0]^T$. (b) The pulses applied to the γ and the P_{bias} cell inputs.

precession corresponding to a rotation by an angle φ is

$$\Delta t = \frac{\varphi}{|\vec{\Gamma}|} = \frac{\hbar}{2\gamma}\varphi. \qquad (5.87)$$

The unitary time evolution operator for this single qubit rotation is

$$U_{-x,\,\varphi} = e^{i\hat{\sigma}_x \frac{\varphi}{2}} = \begin{bmatrix} \cos\frac{\varphi}{2} & i\sin\frac{\varphi}{2} \\ i\sin\frac{\varphi}{2} & \cos\frac{\varphi}{2} \end{bmatrix}. \qquad (5.88)$$

If $\varphi=\pi$ then the polarization of the cell is inverted, that is, the cell goes from the $\vec{\lambda}=[0,0,+1]^T$ state to the $[0,0,-1]^T$ state and vice versa, realizing the *NOT operation,* as shown in Fig. 5.7.
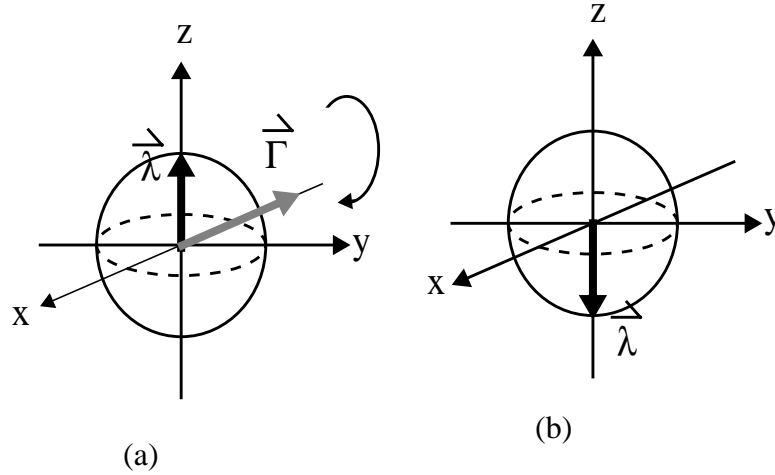
FIGURE 5.7. NOT operation. (a) The initial state is $\vec{\lambda}=[0,0,+1]^T$, that is, $P=-1$. (b) The final state obtained after 180° rotation around the x axis in the negative direction is $\vec{\lambda}=[0,0,-1]^T$, that is, $P=+1$.

Another type of single qubit rotation can be realized if $\gamma=0$ (the barriers are high) and $P_{bias}\gg1$. In this case $\hbar\vec{\Gamma}\cong[0,0,2E_0P_{bias}]^T$ which causes $\vec{\lambda}$ to precess around the z axis as shown in Fig. 5.8. The duration of precession corresponding to a rotation by an angle φ is

$$\Delta t \;=\; \frac{\varphi}{\left|\vec{\Gamma}\right|} \;=\; \frac{\hbar}{2E_0P_{bias}}\varphi. \tag{5.89}$$

The unitary time evolution operator for rotations around the z axis is

$$U_{z,\,\varphi} \;=\; e^{-i\hat{\sigma}_z \frac{\varphi}{2}} \;=\; \begin{bmatrix} e^{i\frac{\varphi}{2}} & 0 \\[2mm] 0 & e^{-i\frac{\varphi}{2}} \end{bmatrix}. \tag{5.90}$$

The (5.76) Hamiltonian does not contain $\hat{\sigma}_y$, however, the rotation around the y axis can still be realized by a series of rotations around the z and x axes:

$$U_{y,\,\varphi} \;=\; U_{z,\,\frac{\pi}{2}} U_{-x,\,\varphi} U_{z,\,\frac{3\pi}{2}} \;=\; -\begin{bmatrix} \cos\frac{\varphi}{2} & -\sin\frac{\varphi}{2} \\[2mm] \sin\frac{\varphi}{2} & \cos\frac{\varphi}{2} \end{bmatrix} \;=\; -e^{i\hat{\sigma}_y \frac{\varphi}{2}}. \tag{5.91}$$

(a)   (b)
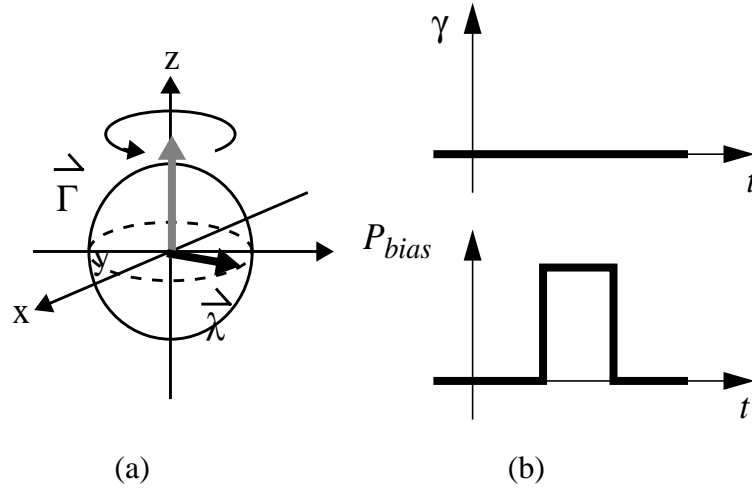
FIGURE 5.8. Rotation around the z axis. (a) The rotation in the λ-space. $P_{bias} \gg 1$ and $\gamma = 0$ (the barriers are high) thus $\hbar\vec{\Gamma} = [0,0,2E_0 P_{bias}]^T$. (b) The pulses applied to the γ and the P_{bias} cell inputs.

The gates presented above were operating on a single qubit. It is reasonable to require that the state of the other qubits in the register do not change. This requirement can be fulfilled in the case of two-state systems by turning off the E_j intercell coupling for the

rest of the cell line, however, for the QCA register the coupling is constant. The unused

part of the register will undergo time evolution thus the effect of this time evolution must

be examined. The time that would be necessary for the intercell coupling to affect the

dynamics considerably is $T_{coupling} = \hbar/E_0$. In the case of single qubit rotations, the

duration of the operation is much shorter than that (compare $T_{coupling}$ to (5.87) with the

condition $\gamma \gg E_0$, and to (5.89) with the condition $P_{bias} \gg 1$) thus the change of the state in the

rest of the line is negligible for single qubit operations.

5.2.3 Multi-qubit operations

The scheme for three-qubit operations presented here can be seen in Fig. 5.9. The
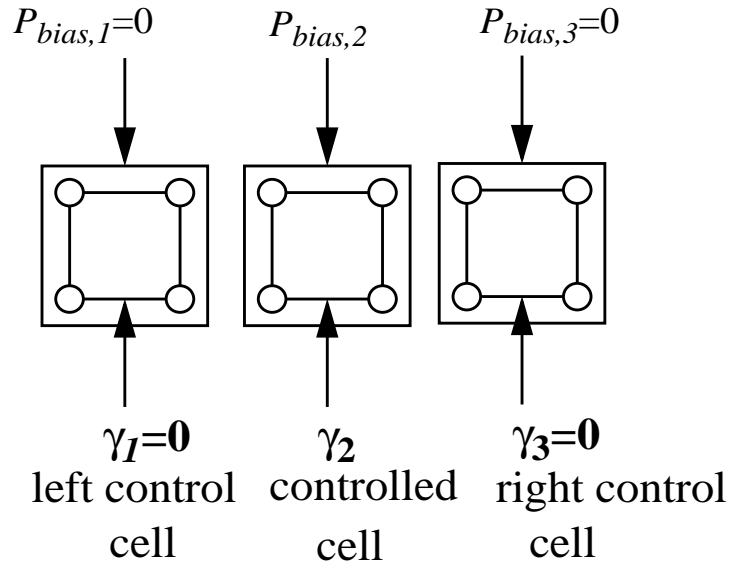
FIGURE 5.9. Schematic of the arrangement for three-qubit operations. The polarizations of the control cells determine what happens to the controlled cell during the operation.

middle cell (cell #2) is the *controlled* cell, its two neighbors (cell #1 and cell #3) are the

left and right *control* cells. The polarizations of the control cells determine what happens

to the controlled cell during the operation. In regard to the multi-qubit operations $\vec{\lambda}$, $\vec{\Gamma}$, γ, P_{bias} and E_Σ without indices refer to the controlled cell. The bias of both control cells are zero and their barriers are high.

For the three-qubit operations $0 < \gamma \ll E_0$. Depending on E_Σ there are two possibilities for the time evolution of the controlled cell:

- If $E_\Sigma = 0$ then $\hbar\vec{\Gamma} = [-2\gamma,0,0]^T$ which causes $\vec{\lambda}$ to precess around the -x axis.

- If $E_\Sigma \neq 0$ then $\hbar\vec{\Gamma} \cong [0,0,2E_0P_{bias}]^T$ which causes $\vec{\lambda}$ to precess around the z axis.

For simplicity suppose that $E_{left}=E_0$ and $E_{right}=2E_0$. Substituting that into (5.81) one obtains

$$E_\Sigma = E_0(P_{left} + 2P_{right} + P_{bias}). \tag{5.92}$$

Let us examine the behavior of the controlled cell for the four possible cases when its two neighbors are fully polarized. E_Σ can be zero only for one of the four possible combinations of P_{left} and P_{right}. For example, choosing $P_{bias}=-3$, it is zero only if both P_{left} and P_{right} are +1. (The other three possibilities can be selected by $P_{bias}=-1$, 1 and 3. Notice that if the E_j coupling would not alternate according to (5.77) then the $P_{left}=+1/P_{right}=-1$ case could not be distinguished from $P_{left}=-1/P_{right}=+1$ since $E_\Sigma = E_0(P_{left} + P_{right} + P_{bias})$ would be the same for both.)

Table I shows E_Σ and $\hbar\vec{\Gamma}$ for the four possible states of the neighbors assuming $P_{bias}=-3$. If both P_{left} and P_{right} are +1 then coherence vector of the cell is rotated around the -x axis, otherwise it is rotated around the -z axis. This will be called *conditional rotation* in the followings.

P_{left}	P_{right}	E_Σ/E_0	$\hbar\vec{\Gamma}$
-1	-1	-6	$[-2\gamma,0,-12E_0]^T \approx [0,0,-12E_0]^T$
-1	+1	-2	$[-2\gamma,0,-4E_0]^T \approx [0,0,-4E_0]^T$
+1	-1	-4	$[-2\gamma,0,-8E_0]^T \approx [0,0,-8E_0]^T$
+1	+1	0	$[-2\gamma,0,0]^T$

TABLE I. The values of $\hbar\vec{\Gamma}$ for the four possible binary states of the left and right neighbors if P_{bias}=-3. If both P_{left} and P_{right} are +1 then $\vec{\Gamma}$ points in the -x direction. If either of them is -1 then $\vec{\Gamma}$ points in the -z direction.

If the left or right neighbors are not fully polarized then the time evolution of the three cells lead to entanglement and the mean-field type description of (5.85) and (5.86) can no longer be used. In this general case, the 3-qubit gate corresponding to P_{bias}=-3 can be characterized by a unitary time evolution operator:

$$
\hat{U} =
\begin{array}{c}
\begin{array}{cccccccc}
\textbf{000} & \textbf{001} & \textbf{010} & \textbf{011} & \textbf{100} & \textbf{101} & \textbf{110} & \textbf{111}
\end{array} \\
\left[
\begin{array}{cccc|cccc}
e^{i\frac{3\varphi_z}{2}} & 0 & 0 & 0 & & & & \\[2ex]
0 & e^{-i\frac{\varphi_z}{2}} & 0 & 0 & & & & \\[2ex]
0 & 0 & e^{-i\frac{3\varphi_z}{2}} & 0 & & & & \\[2ex]
0 & 0 & 0 & e^{i\frac{\varphi_z}{2}} & & & & \\[1ex]
\hline
 & & & & e^{i\frac{\varphi_z}{2}} & 0 & 0 & 0 \\[2ex]
 & & & & 0 & \cos\frac{\varphi_{-x}}{2} & 0 & i\sin\frac{\varphi_{-x}}{2} \\[2ex]
 & & & & 0 & 0 & e^{-i\frac{\varphi_z}{2}} & 0 \\[2ex]
 & & & & 0 & i\sin\frac{\varphi_{-x}}{2} & 0 & \cos\frac{\varphi_{-x}}{2}
\end{array}
\right]
\begin{array}{c}
\textbf{000} \\[2ex]
\textbf{001} \\[2ex]
\textbf{010} \\[2ex]
\textbf{011} \\[1ex]
\textbf{100} \\[2ex]
\textbf{101} \\[2ex]
\textbf{110} \\[2ex]
\textbf{111}
\end{array}
\end{array}
$$

$$. \tag{5.93}$$

In (5.93) φ_{-x} and φ_z are the angles of rotation around the -x and z axes, respectively. They both depend on the *t* duration of the operation:

$$\varphi_{-x,\,t} = \left|\vec{\Gamma}\right|t = \frac{2\gamma}{\hbar}t, \tag{5.94}$$

and

$$\varphi_{z,\,t} = \left|\vec{\Gamma}\right|t = \frac{2E_0}{\hbar}t. \tag{5.95}$$

The labels are showing the three-qubit states (the product basis vectors) corresponding to the rows and columns of the matrix. "1" and "0" refer to the $|1\rangle$ and $|-1\rangle$ states. The three digits correspond to the polarization of the left, the middle and the right cells, respectively. Blank off-diagonal blocks refer to blocks of zeros omitted here for easier understanding.

It is often advantageous to eliminate the rotation around the z axis for multi-qubit operations. The rotation around z does not change the state of the controlled cell if φ_z is an integer multiple of 4π. The corresponding constraint for the duration of the operation is

$$t = \frac{2\pi\hbar}{E_0}m\,;\ m=0,\ 1,\ 2,\ ... \tag{5.96}$$

With the choice of (5.96) for t, rotation occurs around the x axis when $P_{left}=P_{right}$, however, the state of the cells do not change, if $P_{left}\neq P_{right}$. In multi-qubit gates later it will always be supposed that t is chosen so that rotation around the z axis does not take place. In this way φ_z can be ignored and φ_{-x} will be replaced with φ. Since t is constant, φ must be set by controlling γ. Combining (5.94) and (5.96) gives:

$$\gamma = \frac{\hbar}{2t}\varphi = \frac{E_0}{4\pi m}\varphi. \tag{5.97}$$

Applying condition (5.96) to (5.93) the following gate is obtained:

$$\hat{U}_{-x,\ \varphi;-3} = \left[\begin{array}{cccc|cccc} 1 & 0 & 0 & 0 & & & & \\ 0 & 1 & 0 & 0 & & & & \\ 0 & 0 & 1 & 0 & & & & \\ 0 & 0 & 0 & 1 & & & & \\ \hline & & & & 1 & 0 & 0 & 0 \\ & & & & 0 & \cos\frac{\varphi}{2} & 0 & i\sin\frac{\varphi}{2} \\ & & & & 0 & 0 & 1 & 0 \\ & & & & 0 & i\sin\frac{\varphi}{2} & 0 & \cos\frac{\varphi}{2} \end{array}\right]. \tag{5.98}$$

The "-3" refers to a rotation around x with the condition given by P_{bias}=-3. A variation of this quantum gate can be found in the literature [62,65] as U_λ or the Deutsch gate [73,74]. The only difference between (5.98) and the Deutsch gate is that cell #2 and cell #3 are exchanged. If $\varphi=\pi$ then the controlled cell is inverted if both control cells have polarization +1.

A two-qubit gate can be realized as a series of two three-qubit gates:

$$\hat{U}_{-x,\,\varphi;(-3,\,-1)} \;=\; \hat{U}_{-x,\,\varphi;-3}\hat{U}_{-x,\,\varphi;-1}\,. \tag{5.99}$$

This gate rotates around x if P_{right} =+1 while the polarization of the left neighbor does not matter. Taking $\varphi=\pi$, (5.98) can be used to implement the *controlled NOT* operation:

$$\hat{U}_{-x,\,\pi;(-3,\,-1)} \;=\; \begin{bmatrix} \begin{matrix} 1 & 0 & 0 & 0 \\ 0 & 0 & 0 & i \\ 0 & 0 & 1 & 0 \\ 0 & i & 0 & 0 \end{matrix} & \\ & \begin{matrix} 1 & 0 & 0 & 0 \\ 0 & 0 & 0 & i \\ 0 & 0 & 1 & 0 \\ 0 & i & 0 & 0 \end{matrix} \end{bmatrix}. \tag{5.100}$$

The controlled cell is inverted if the right control cell has polarization +1. That is almost a controlled NOT, but there is an additional $\pi/2$ phase shift if inversion happens. With the additional application of

$$\hat{U}^{(3)}_{z,\,\varphi} \;=\; diag\!\left(e^{i\frac{\varphi}{2}},\, e^{-i\frac{\varphi}{2}},\, e^{i\frac{\varphi}{2}},\, e^{-i\frac{\varphi}{2}},\, e^{i\frac{\varphi}{2}},\, e^{-i\frac{\varphi}{2}},\, e^{i\frac{\varphi}{2}},\, e^{-i\frac{\varphi}{2}}\right) \tag{5.101}$$

for $\varphi = \pi/2$ one can get rid of this additional phase shift and realize the controlled NOT operation. $\hat{U}^{(3)}_{z,\,\varphi}$ is the time evolution operator corresponding to the rotation of the third qubit around the z axis. Its matrix form can be obtained from (5.90) by extending the operator from one qubit to three qubits. (The operator does not affect the other two qubits.)

According to Refs. 71-73 the set of operations presented above makes our quantum computer universal, thus it is able to perform any unitary operation.

The "doing nothing" problem

It follows from (5.94) that the execution time of a multi qubit gate is

$$t \sim \frac{\hbar}{2\gamma}. \tag{5.102}$$

Since $\gamma \ll E_0$, the (5.102) execution time is much longer than $T_{coupling} = \hbar/E_0$ and thus the intercell coupling will affect the dynamics of the rest of the line. The duration of the operation must be chosen in such a way that the state of the rest of the line does not change.

Suppose that the three-qubit gate described by (5.93) is operating on the first three cells of the line while there is no operation taking place on the rest of the cells. (For these cells $P_{bias,j}=0$ and $\gamma_j=0$.) The unitary operation for the whole line is:

$$\hat{U}_{whole} = e^{-\frac{i}{\hbar}\hat{H}_{whole}t} = \left(e^{-\frac{i}{\hbar}\hat{H}_{gate}t}\right)\left(e^{-\frac{i}{\hbar}\hat{H}_{rest}t}\right)\left(e^{-\frac{i}{\hbar}\hat{H}_{interaction}t}\right), \tag{5.103}$$

Here

$$\hat{H}_{gate} = -\gamma_2\hat{\sigma}_x(2)-E_0(\hat{\sigma}_z(1)\hat{\sigma}_z(2) + 2\hat{\sigma}_z(2)\hat{\sigma}_z(3))-3E_0\hat{\sigma}_z(2), \tag{5.104}$$

$$\hat{H}_{rest} = -\sum_{j=4}^{N-1} E_j\hat{\sigma}_z(j)\hat{\sigma}_z(j+1), \text{ and} \tag{5.105}$$

$$\hat{H}_{interaction} = -E_0\hat{\sigma}_z(3)\hat{\sigma}_z(4). \tag{5.106}$$

The unitary evolution of the whole line can be split into three terms according to (5.103) since the (5.104-5.106) Hamiltonians commute with each other. To avoid the change in the

rest of the cell line, the second and third term on the right hand side of (5.103) must be equal to an identity matrix (or an additional overall phase factor is also allowed).

The second term is a diagonal matrix. Its kth diagonal element is

$$d_k = e^{\frac{it}{\hbar}\left(\sum_{j=4}^{N-1} E_j P_j^{(k)} P_{j+1}^{(k)}\right)}, \tag{5.107}$$

where $P_j^{(k)} = \pm 1$ refers to the polarization of the jth cell of the kth product basis vector. (For example, for $N{=}5$ qubits the 32 product basis vectors are 00000, 00001, 00010, ...,11111 and k is in the range of 1 to 32.) Notice that $\sum E_j P_j P_{j+1}$ is an integer multiply of E_0. With the choice of

$$t = \frac{2\pi\hbar}{E_0}m \, ; \, m{=}1, 2, 3, \, ... \tag{5.108}$$

the phases of the elements given by (5.107) are the integer multiples of 2π. Thus $\exp\left(-\frac{i}{\hbar}\hat{H}_{rest}t\right) = \hat{1}$ and the state of the other cells of the line does not change. It can be seen that (5.96) and (5.108) are the same. The $\exp\left(-\frac{i}{\hbar}\hat{H}_{interaction}t\right) = \hat{1}$ condition leads to (5.108) as well.

Issues about necessary accuracy of control parameters

Up to now the control parameters were assumed to be ideal. Now it will be investigated how much deviation of the control parameters can be tolerated. Especially the accuracy requirements on the bias, on the coupling and on the timing of the operations will be examined qualitatively.

In the case of the multi-qubit gates described in the beginning of Sec. IV, $\vec{\Gamma}$ does not have a z component if the polarizations of the two neighbors are such that $E_\Sigma = 0$. In

this case the terms in (5.92) cancel each other. (The corresponding notion is the "resonant pulse" for nuclear spin quantum computing [91]. The pulse has an effect only if its frequency equals the resonance frequency.) In practice, the third coordinate of $\vec{\Gamma}$ is not zero, but it must be much smaller than the first: $E_\Sigma = E_0(P_{left} + 2P_{right} + P_{bias}) \ll \gamma$. For a multi-qubit operation $\gamma \ll E_0$. Combining the two inequalities and dividing by E_0 leads to $P_{left} + 2P_{right} + P_{bias} \ll \frac{\gamma}{E_0} \ll 1$. Thus for the error of the bias

$$\Delta P_{bias} \ll \frac{\gamma}{E_0} \ll 1 \tag{5.109}$$

is required. Up to now the E_j intercell couplings were supposed to be exactly E_0 or $2E_0$, however, in reality they will be slightly different. From a similar deduction it follows that to fulfill $E_\Sigma \ll \gamma$ the E_j intercell couplings must satisfy similar requirements to P_{bias}. A possible solution in order to nullify the effects of the variance of intercell couplings is to fine tune the four P_{bias} values necessary to select one of the four possible combinations of P_{left} and P_{right} after the fabrication of the circuit.

The first step to get the constrains for the accuracy for the timing is to combine (5.102) and (5.108) with the requirement $\gamma \ll E_0$. One obtains $4\pi m \sim \frac{E_0}{\gamma} \gg 1$. The error in the rotation around axis z must fulfill $\Delta\varphi_{z,t} \ll 2\pi$. Combining this with (5.95) imposes on the error of timing $\Delta t \ll \frac{\pi\hbar}{E_0}$. Dividing both sides by (5.96) leads to $\frac{\Delta t}{t} \ll \frac{1}{2m}$. Hence

$$\frac{\Delta t}{t} \ll \frac{\gamma}{E_0} \ll 1. \tag{5.110}$$

That is, the duration of the pulse must be very well controlled in order to cancel the effect of the rotation around z for multi-qubit gates.

Alternative multi-qubit gates

Conditional gates can be implemented without exploiting the "resonance-like" effect that was applied in the previous multi-qubit gates [92]. Their advantage is that they do not need as exact control of $P_{bias,j}$'s and E_j's. (From now, suppose that all $E_j=E_0$.) For example, for three isolated cells a three-qubit gate can be obtained as

$$\hat{U} = \hat{U}^{(2)}_{-x, \frac{3\pi}{2}} \hat{U}^{(1,2,3)}_{idle, \frac{\pi}{2}} \hat{U}^{(2)}_{-x, \frac{\pi}{2}} = \left[\begin{array}{cccc|cccc} 0 & 0 & 1 & 0 & & & & \\ 0 & -1 & 0 & 0 & & & & \\ -1 & 0 & 0 & 0 & & & & \\ 0 & 0 & 0 & -1 & & & & \\ \hline & & & & -1 & 0 & 0 & 0 \\ & & & & 0 & 0 & 0 & -1 \\ & & & & 0 & 0 & -1 & 0 \\ & & & & 0 & 1 & 0 & 0 \end{array}\right], \tag{5.111}$$

where

$$\hat{U}^{(1,2,3)}_{idle, \varphi} = diag(e^{i\varphi}, 1, e^{-i\varphi}, 1, 1, e^{-i\varphi}, 1, e^{i\varphi}). \tag{5.112}$$

This modified version of controlled controlled NOT inverts the middle cell if its two neighbors have the same polarization. $\hat{U}^{(1,2,3)}_{idle, \varphi}$ describes the time evolution of the three-cell system if $P_{bias,j}=0$ and $\gamma_j=0$ for $j=1,2,3$. $\varphi = \frac{2E_0}{\hbar}t$ for (5.112), where t is the duration of the time evolution.

A modified version of controlled NOT [92] for two isolated cell is:

$$\hat{U}_{CNOT'} = \hat{U}^{(1)}_{-x, \frac{3\pi}{2}} \hat{U}^{(1,2)}_{idle, \frac{\pi}{2}} \hat{U}^{(1)}_{z, \frac{3\pi}{2}} \hat{U}^{(1)}_{-x, \frac{\pi}{2}} = \left[\begin{array}{cc|cc} 1 & 0 & 0 & 0 \\ 0 & 1 & 0 & 0 \\ \hline 0 & 0 & 0 & 1 \\ 0 & 0 & -1 & 0 \end{array}\right], \tag{5.113}$$

where

$$\hat{U}_{idle,\,\phi}^{(1,\,2)} = diag\left(e^{i\frac{\phi}{2}}, e^{-i\frac{\phi}{2}}, e^{-i\frac{\phi}{2}}, e^{i\frac{\phi}{2}}\right).\tag{5.114}$$

It is possible to realize controlled NOT with the correct phases with a longer sequence of gates [88], however, (5.113) seems to be the simplest two-qubit gate suitable for the first experimental realizations and not exploiting the "resonance-like" phenomenon.

Notice that in (5.113) all the operations except for $\hat{U}_{idle,\,\phi}$ are single qubit transformations. $\hat{U}_{idle,\,\phi}$ is the operation through which the control cell can affect the controlled cell while in the case of gates (5.93), (5.98) and (5.100) it was realized by the "resonance-like" behavior.

5.2.4 Discussion

It is instructive to compare the C-QCA quantum computer to the nuclear spin quantum computers [67,68,69,75,76]. The role of the nuclear spin is now played by the coherence vector. The spin of the nucleus is manipulated by a strong constant magnetic field and a weaker alternating one while the C-QCA uses external electrodes to control the interdot tunneling barriers. In the case of a spin quantum computer there is a spin-spin coupling while the C-QCA cells are coupled Coulombically. The classical analogy of the spin-1/2 system is a magnetic dipole. The classical analogy of a C-QCA cell is an electric quadrupole. In nuclear or electron spin quantum computing manipulating individual qubits is rather difficult. The NMR devices are running an ensemble of parallel quantum computers. A related approach [78,82] uses the electron spin in a quantum dot for a qubit, but the hardware for writing data in and reading data out has not been developed yet. The technology for writing into and reading out of the individually accessible C-QCA cells is

already available. The limiting factor in the C-QCA approach is the shorter decoherence time which restricts the number of quantum operations.

In regards to physical realizibility, the ratio of the execution time of a quantum operation and the decoherence time is very important. A conservative estimate for the decoherence time in the semiconductor quantum dots can be a couple of *ps*. This is used in Ref. 12 for the modeling of a digital QCA where coherence is not required. For quantum computing applications further efforts must be made to increase decoherence time [71]. In general, it is not at all clear, what are the limits from this point of view.

The time that is necessary for the intercell coupling to affect the dynamics considerably is $T_{coupling} = \hbar/E_0$. Assuming $E_0 = 1meV$, $T_{coupling} = \dfrac{\hbar}{E_0} \approx 1ps$. According to (5.87), the duration for the NOT operations is $T = \dfrac{\hbar\pi}{2\gamma}$. It is smaller by several orders of magnitude than $T_{coupling}$, because $\gamma \gg E_0$. The same is true for the rotations around the -*x* axis. The duration of a controlled NOT is also $T = \dfrac{\hbar\pi}{2\gamma}$, but $\gamma \ll E_0$. Thus the time to execute a controlled NOT is longer by several orders of magnitude than $T_{coupling}$. The gates described by (5.111) and (5.113) have an execution time near $T_{coupling}$.

Two crucial questions concerning the feasibility of C-QCA quantum computing remain to be addressed. The first is whether a large quantum register can be realized with C-QCA in the future. The second is whether a system with a few qubits can be realized with the present or near future technology. Even if large scale implementation proves to be difficult, C-QCA technology can still be used as a tool to test the concepts of quantum computing in solid state devices.

An alternative to the four-dot cell with two extra electrons is a two-dot cell with one extra electron. E_0 in a double-dot cell can be much smaller than the energy difference between the ground state and the excited state of the electron in the quantum dot thus the excitation of parasitic energy levels ("leakage") can be suppressed, unlike in the case of proposals where the information is stored in the ground state and the excited state of the electron in the quantum-dot [71]. A drawback of the double-dot cell is that the strength of the intercell-coupling does not decrease with distance as fast as in the case of four-dot cells thus next to nearest neighbors must be also included in the model of a cell line. For the first realization of a multi-qubit gate, the controlled NOT described by (5.113) seems to be most reasonable with two two-dot C-QCA cells.

5.2.5 Conclusions

In this paper a multi quantum-dot structure, the Quantum Cellular Automata (QCA) was proposed to realize quantum computing. The basic operations were performed with a line of QCA cells, so QCA is viable option for constructing a universal quantum computer. The QCA may offer an example of integrable quantum computer with electrostatic data read in/write out. The main drawback of our implementation is the relatively short decoherence time comparing to the implementations using nuclear or electron spins.

CHAPTER 6

APPROXIMATE QCA QUANTUM DYNAMICS

In a classical multi-particle system the number of degrees of freedom necessary for the state description increases linearly with the number of particles. A point-like particle can be described by its position and velocity. For N particles, N positions and N velocities are required which gives N times more degrees of freedom than for a single particle.

In a quantum mechanical system of N QCA cells, the number of degrees of freedom are much larger than N times the degrees of freedom of a single cell. The extra degrees of freedom come from the intercell *correlations*. The information necessary for a total description increases exponentially with the number of cells and makes it difficult to simulate even a modest size block of QCA cells. To describe N coupled cells exactly, $2^{2N}-1$ variables are necessary for the coherence vector description.

With the state vector description it is possible to use the Hartree-Fock approximation and divide the multi-cell system into single cell quantum mechanical subsystems coupled classically to each other. This simplification does not consider inter-cell correlations at all thus the results obtained from this method differ greatly from that of the exact model, especially when describing the dynamical behavior.

The coherence vector description makes it possible to divide the state variables into groups. One group corresponds to the state of the cells, another group corresponds to the two-point, three-point, etc. correlations. A correlation term can be nearest neighbor,

next-to-nearest neighbor, etc. This feature of the coherence vector description helps us to determine which correlation terms are important from the point of view of the dynamics and which can be neglected. Usually it is reasonable to assume that the further than nearest neighbor and higher order correlations play a less important role, thus they can be approximated by lower order correlations. Depending on which correlation terms are kept and which are neglected, models with different levels of approximations can be constructed which are intermediate between the Hartree-Fock and the exact method. Sec. 6.1 presents a model keeping the two-point correlations and neglecting higher order ones. (The section is based on the theory of the coherence vector description presented in Sec. 5.1. For definitions of notions such as three-point correlation tensor and correlation tensor proper consult this section.)

In Sec. 6.2 an example, the so-called majority logic gate with unequal input legs, is shown for which the self-consistent mean-field (Hartree-Fock) method gives qualitatively wrong results. An improved version of the self-consistent mean-field approximation is presented which by including correlation effects determines the ground state correctly.

Modeling a line of QCA cells as two-state systems leads to the same Hamiltonian as modeling an Ising spin chain with nearest neighbor ferromagnetic coupling in transverse magnetic field. The statistical behavior of the Ising chain in thermal equilibrium has been thoroughly investigated in the literature, however, up to now not much attention was paid to the quantum dynamics of a finite system making our approach useful even from the point of view of the theory of coupled two-state systems.

6.1 Model neglecting three-point and higher order correlations

When modeling two coupled cells, the state of the two-cell system is described by the two single-cell coherence vectors and the (two-point nearest neighbor) correlation tensor. If there are more than two cells, third order (three-point) correlation terms show up in the dynamic equation of the two-point correlations. If the number of cells is greater than three, then fourth order correlation terms will appear in the dynamic equations of the third order terms. Thus a hierarchy of equations is obtained. The hierarchy of equations seems to be ideal to construct intermediate models between the Hartree-Fock and the exact method, by truncating the equation system at a reasonable point.

According to Sec.5.1.6, the Hartree-Fock approximation can be obtained from the exact equations for the coherence vectors assuming that the $M_{ab}(i, i+1)$ two-point correlation tensor proper elements are zero and the elements of the two-point correlation tensors can be approximated with coherence vector elements: $K_{ab}(i, i+1) = \lambda_a(i)\lambda_b(i+1)$. The first approximation, that is better than the Hartree-Fock, could be obtained by keeping the second order correlations and approximating the third order correlations. It will be assumed that three-point correlation tensor proper elements are zero and the elements of the three-point correlation tensors will be approximated with lower order correlations and coherence vector elements

The three-point correlation proper of A, B, and C can be given (see (5.45); see also [57], equation (2.811) on page 168) with the three-point correlation and the lower order correlations as

$$M(A, B, C) = \langle ABC \rangle - \langle AB \rangle \langle C \rangle - \langle BC \rangle \langle A \rangle - \langle AC \rangle \langle B \rangle + 2\langle A \rangle \langle B \rangle \langle C \rangle. \tag{6.1}$$

Assuming that it is zero gives an approximation for the three-point correlations:

$$K(A, B, C) \;=\; \langle ABC \rangle \approx \langle AB \rangle \langle C \rangle + \langle BC \rangle \langle A \rangle + \langle AC \rangle \langle B \rangle - 2\langle A \rangle \langle B \rangle \langle C \rangle. \quad (6.2)$$

For example, if $A = \hat{\sigma}_x(1)$, $B = \hat{\sigma}_z(3)$ and $C = \hat{\sigma}_y(6)$, one obtains

$$K_{xzy}(1, 3, 6) \approx \langle \hat{\sigma}_x(1)\hat{\sigma}_z(3) \rangle \langle \hat{\sigma}_y(6) \rangle + \langle \hat{\sigma}_z(3)\hat{\sigma}_y(6) \rangle \langle \hat{\sigma}_x(1) \rangle + \qquad (6.3)$$

$$\langle \hat{\sigma}_x(1)\hat{\sigma}_y(6) \rangle \langle \hat{\sigma}_z(3) \rangle - 2\langle \hat{\sigma}_x(1) \rangle \langle \hat{\sigma}_z(3) \rangle \langle \hat{\sigma}_y(6) \rangle.$$

(6.3) can be written down with correlation tensor and coherence vector elements as well:

$$K_{xzy}(1, 3, 6) \approx K_{xz}(1, 3)\lambda_y(6) + K_{xy}(1, 6)\lambda_z(3) + K_{zy}(3, 6)\lambda_x(1) - 2\lambda_x(1)\lambda_z(3)\lambda_y(6).$$

$$(6.4)$$

The general formula for approximating any three-point correlations is

$$(6.5)$$

$$K_{abc}(i, j, k) \;=\; \langle \hat{\sigma}_a(i)\hat{\sigma}_b(j)\hat{\sigma}_c(k) \rangle \approx K_{ab}(i, j)\lambda_c(k) + K_{bc}(j, k)\lambda_a(i) +$$

$$K_{ac}(i, k)\lambda_b(j) - 2\lambda_a(i)\lambda_b(j)\lambda_c(k),$$

$$a, b, c \;=\; x, y, z.$$

Using this approximation, the three-point correlations can be eliminated from the dynamical equations (5.32-5.35). The model using this approximation will be called "PC" referring to that it keeps only the pair correlations. It describes the state of the cell array by the coherence vectors of the cells and all the two-point correlations. (For detailed deduction see Appendix C.)

Notice that not all the possible 3x3x3=27 three-point correlations must be approximated by lower order ones, only those which can be found in the (5.32-5.35) dynamical equations of the two-point correlations. As it was mentioned in Sec. 5.1.2, there are 14 of them: *xyz, xxz, yyz, yxz, zyz, zxz, zyx, zxx, zyy, zxy, zzy, zzx, yzz* and *xzz.*

The system of equations can be reduced further by approximating the next to nearest neighbor two-point correlations by the multiplication of corresponding two coherence vector elements based on the assumption that the next to nearest neighbor

141

correlations are less important than the nearest neighbor correlations: e.g., $K_{xy}(1, 3) \approx \lambda_x(1)\lambda_y(3)$. The general formula for approximating any nearest neighbor three-point correlation this way is

$$K_{abc}(i, i+1, i+2) = \langle \hat{\sigma}_a(i)\hat{\sigma}_b(i+1)\hat{\sigma}_c(i+2) \rangle \approx$$
$$K_{ab}(i, i+1)\lambda_c(i+2) + K_{bc}(i, i+2)\lambda_a(i+1) - \lambda_a(i)\lambda_b(i+1)\lambda_c(i+2), \quad (6.6)$$
$$a, b, c = x, y, z.$$

Using this approximation, the three-point correlations and the further than nearest neighbor correlations can be eliminated from the (5.32-5.34) dynamical equations of the coherence vectors and the nearest neighbor correlations. The method based on this approximation will be called "NNPC" referring to that it includes only the nearest neighbor pair correlations in the state description of the cell array. (See Fig. 6.1 for the interpretation of pair correlations and three-point correlations. See Appendix C for a more detailed explanation of the deduction and for summary of the equations.)

Since we do not need the dynamical equations for the non-nearest neighbor correlations, only the three-point correlation terms which can be found in the (5.32-5.34) dynamical equation of the nearest neighbor pair correlations must be approximated. There are 10 of them: *xyz, xxz, yyz, yxz, zyz, zxz, zyx, zxx, zyy* and *zxy*.
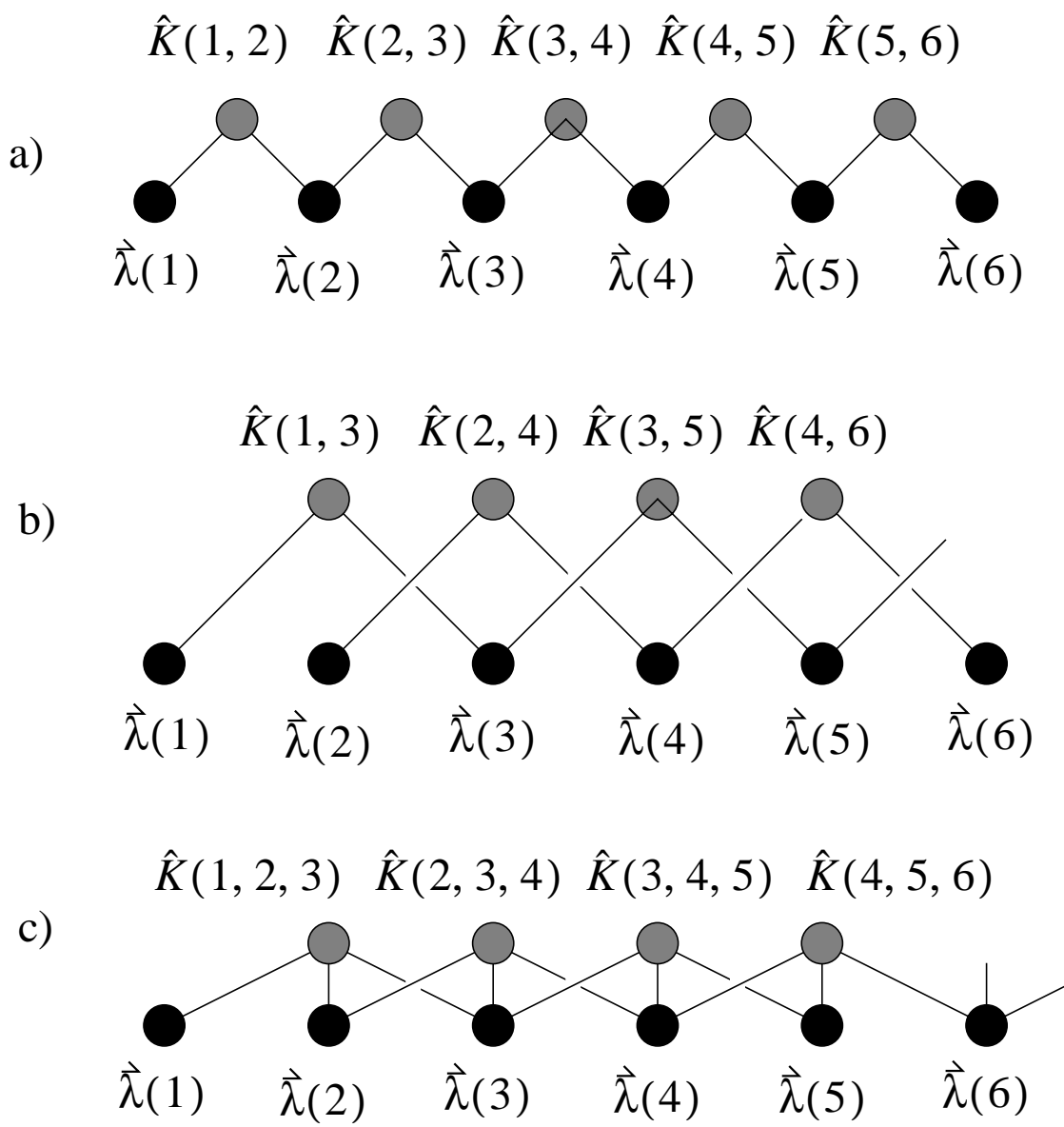
FIGURE 6.1. Scematic for (a) the nearest neighbor pair correlations, (b) the next to nearest neighbor pair correlations and (c) the nearest neighbor three-point correlations.

6.1.1 Comparison of the dynamics of the exact and approximate methods

Computer simulations were made to compare PC and NNPC with the Hartree-Fock approximation and the exact model with the many-body Hamiltonian. The comparison was done for the case of adiabatic switching of a QCA cell line.

The PC and NNPC describes the system of two cells exactly, thus the smallest cell array for which the behavior of these approximations is worth to study has three cells. To describe the state fully, beside the two point correlation tensors $\hat{K}(1, 2, 3)$, a $3 \times 3 \times 3$ three-point correlation tensor is necessary as shown in Fig. 6.2. PC approximates the elements of this tensor with lower order correlations and keeps all the 3×3 pair correlation tensors: $\hat{K}(1, 2)$, $\hat{K}(1, 3)$ and $\hat{K}(2, 3)$. NNPC approximates even $\hat{K}(1, 3)$.

The first simulation example is the adiabatic switching of a line of three cells as shown Fig. 6.3(a). The first cell is coupled to a driver cell. The tunneling coefficient is gradually lowered (the barriers are raised) as shown in Fig. 6.3(b). Fig. 6.3(c) shows the dynamics of the coherence vector coordinates for the three cells coming from PC. At the end all the three cells align with the driver, that is, at the end $\lambda_z(i) \approx -1$. Figs. 6.3(c) and (d) show a comparison of the curves corresponding to the Hartree-Fock approximation, the NNPC, the PC and the exact model. It is clearly visible that NNPC gives a better match with the exact model than the Hartree-Fock approximation does and PC gives a better match than NNPC.
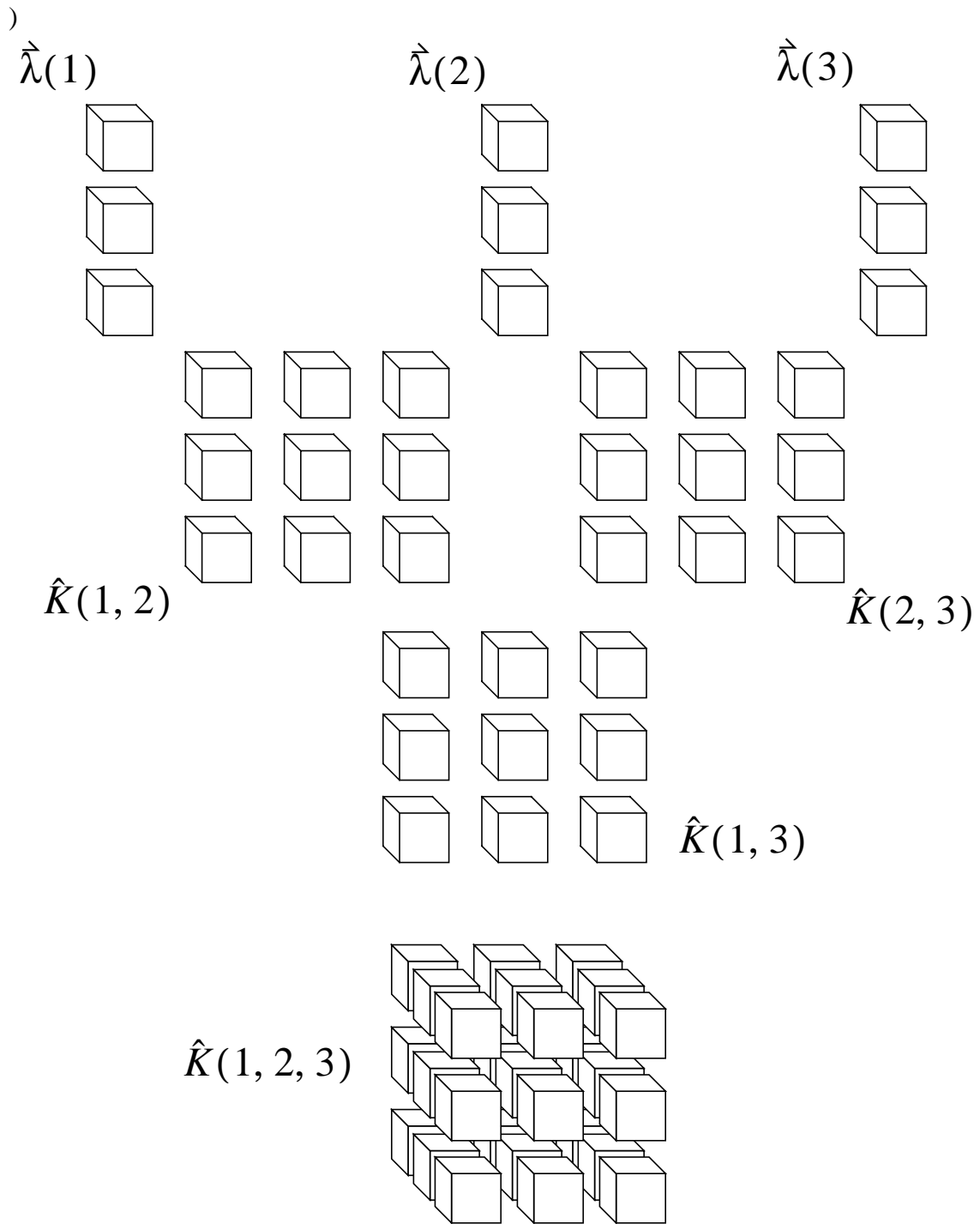
FIGURE 6.2. Modeling three coupled cells. The state of the $SU(2) \otimes SU(2) \otimes SU(2)$ system is fully described by the three coherence vectors, the three 3×3 pair correlation tensors and the $3 \times 3 \times 3$ three-point correlation tensor. PC neglects the $\hat{K}(1, 2, 3)$ three-point correlation tensor keeping 36 variables of the 63. NNPC ignores even the $\hat{K}(1, 3)$ next nearest neighbor correlation, and keeps 27 variables.
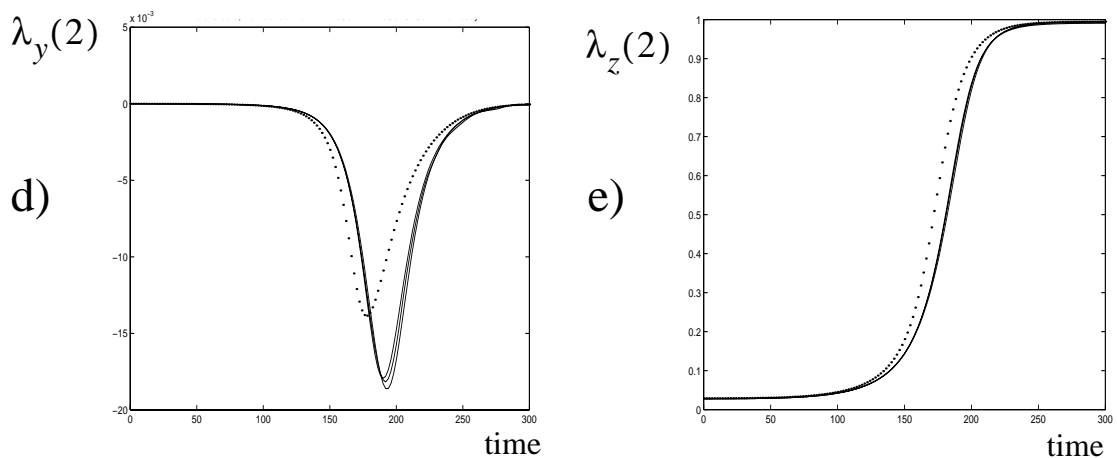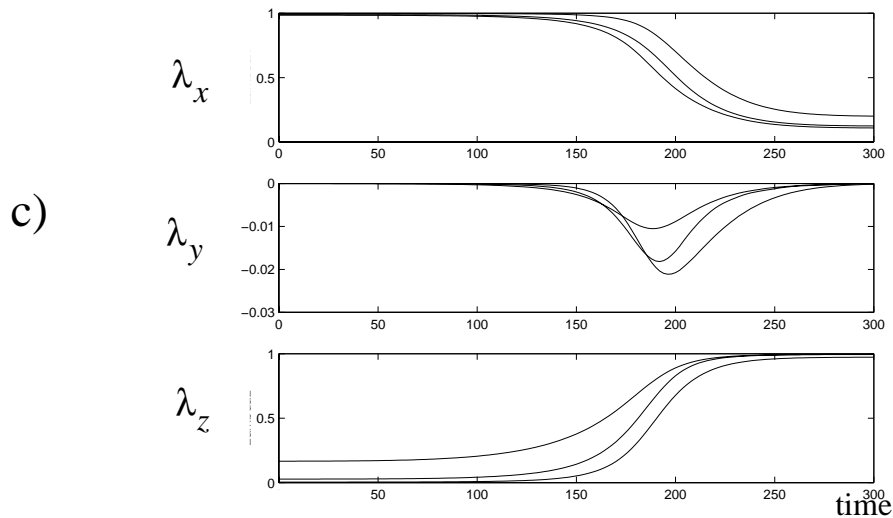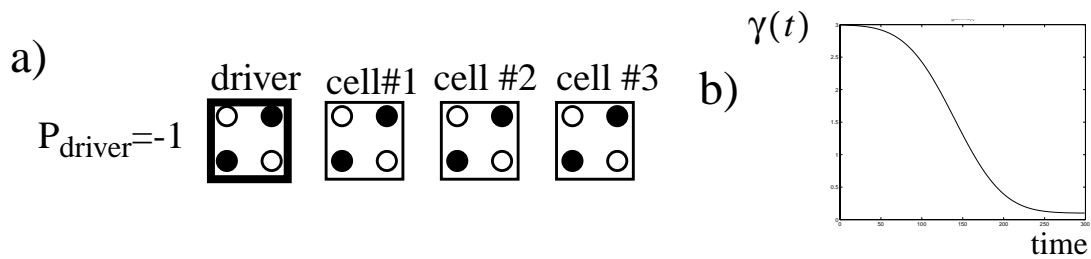
FIGURE 6.3. Adiabatic switching of three cells. The barriers are gradually lowered while the driver has constant -1 polarization. The three cells follow the polarization of the driver. (a) The arrangement of the three cells and a driver, (b) the dynamics of the interdot tunneling energy, (c) the elements of the three coherence vectors as the function of time for the PC, (d) $\lambda_y(2)$ as the function of time for the Hartree-Fock approximation (dotted), NNPC (solid), PC (solid) and the exact model (solid), (e) $\lambda_z(2)$ as the function of time for the Hartree-Fock approximation (dotted), NNPC (solid), PC (solid) and the exact model solid).

146

Figs. 6.4(a-d) show the pair correlation tensor proper elements for PC and the exact model. PC is a qualitative improvement comparing to the Hartree-Fock approximation since the Hartree-Fock approximation does not model intercell correlations at all.

The second simulation example is the adiabatic switching of a line of five cells. Fig. 6.5 shows the structure, the time dependence of the tunneling energy and the dynamics of the coherence vector elements. In Fig. 6.6 the dynamics of the nearest neighbor two-point correlations are presented computed with NNPC and the exact model.

PC does not seem to have an obvious superiority over NNPC in spite of the larger quantum degrees of freedom that are kept. (It is also much harder to handle numerically because of the complicated nonlinear couplings between the state variables make the integration of the differential equation very sensitive to noise.) An intermediate model between PC and NNPC can be constructed keeping the next-to-nearest neighbor correlations and approximating the further-than-next-to-nearest neighbor correlation terms. Further improvement on NNPC could be made by including three-point correlation terms.

Table 6.1 shows the number of real variables used for state description for the different methods. With the Hartree-Fock method, describing each cell by a three element coherence vector, the number of variables scales linearly with the number of cells. With the density matrix description the quantum state is described by a 2^Nx2^N matrix, thus the number of variables scales exponentially with the number of cells. For NNPC, however, the number of variables scales linearly with the number of cells, and for PC the number of variable scale with the square of the number of cells
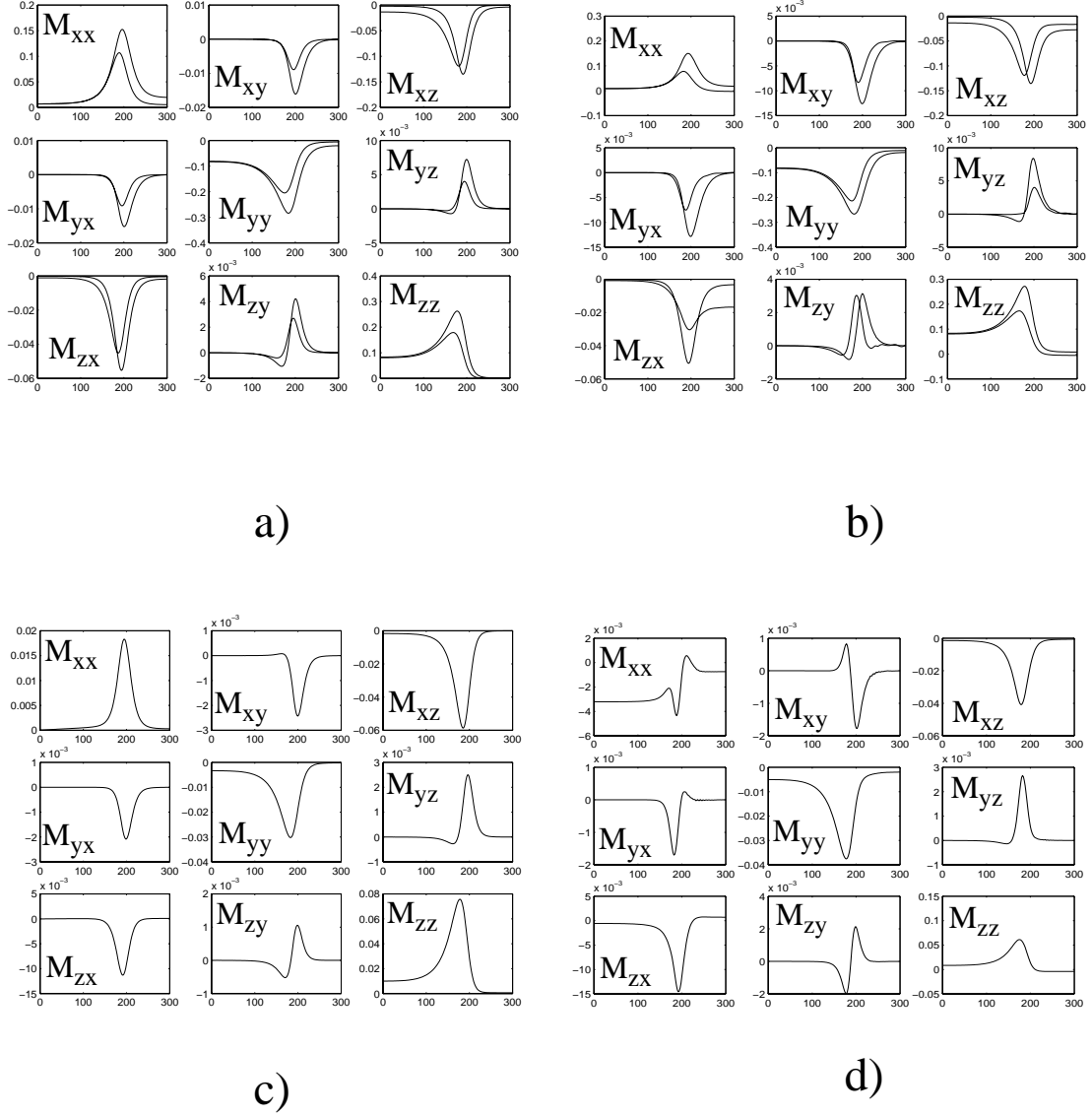
FIGURE 6.4. Adiabatic switching of three cells. The barriers are gradually raised while the driver has constant -1 polarization. The nearest neighbor correlation tensor proper elements for the (a) exact model and (b) PC. The next to nearest neighbor correlation tensor proper elements for the (c) exact model and (d) PC. Notice that the peak of the absolute value of the nearest neighbor pair correlations are usually bigger than that of the next to nearest neighbor pair correlations.
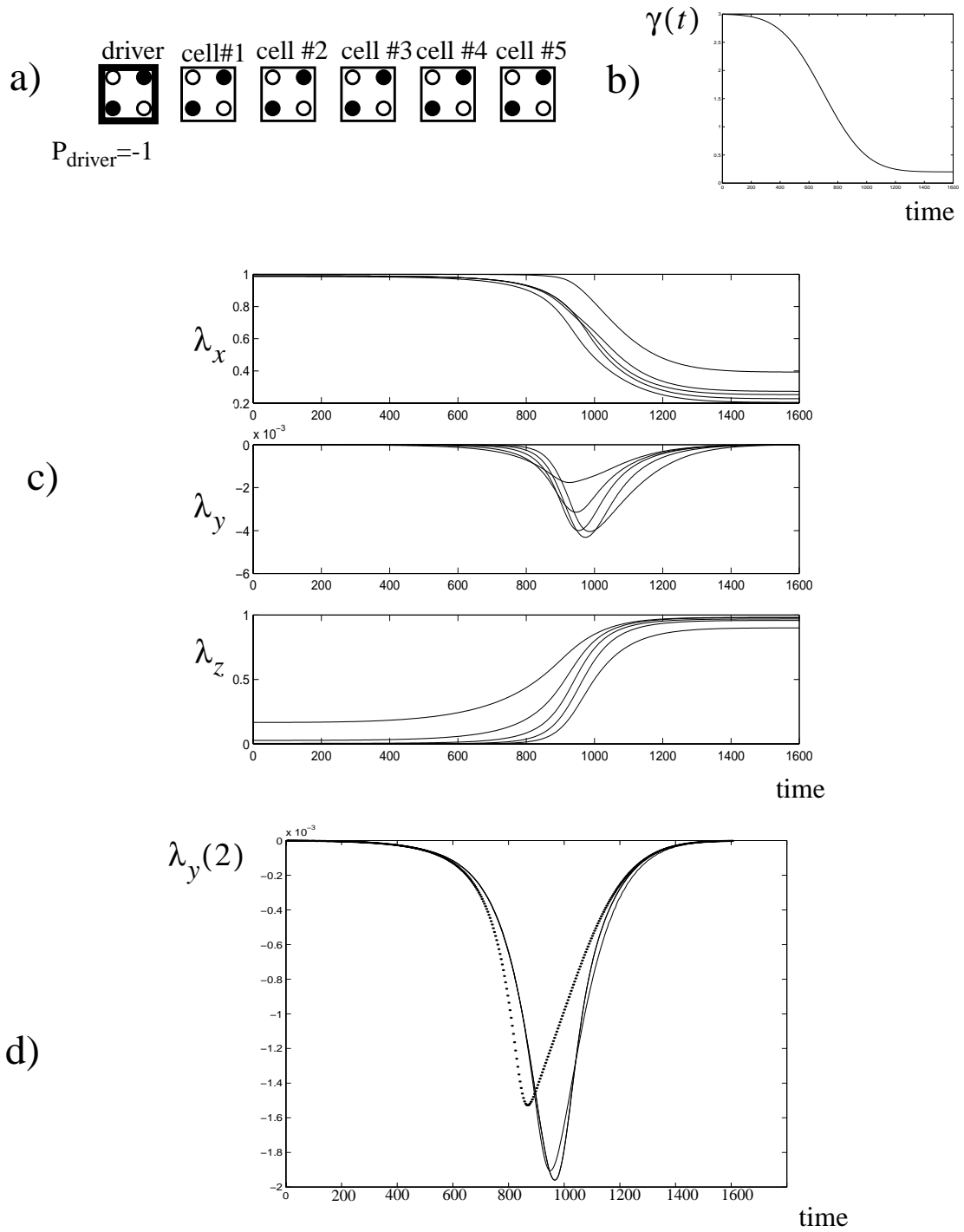
FIGURE 6.5. Adiabatic switching of a line of five cells. The barriers are gradually lowered while the driver has constant -1 polarization. The five cells follow the polarization of the driver. (a) The arrangement of the five cells and a driver, (b) the dynamics of the interdot tunneling energy, (c) the elements of the three coherence vectors as the function of time for the PC, (d) $\lambda_y(2)$ as the function of time for the Hartree-Fock approximation (dotted), NNPC (solid), PC (solid) and the exact model
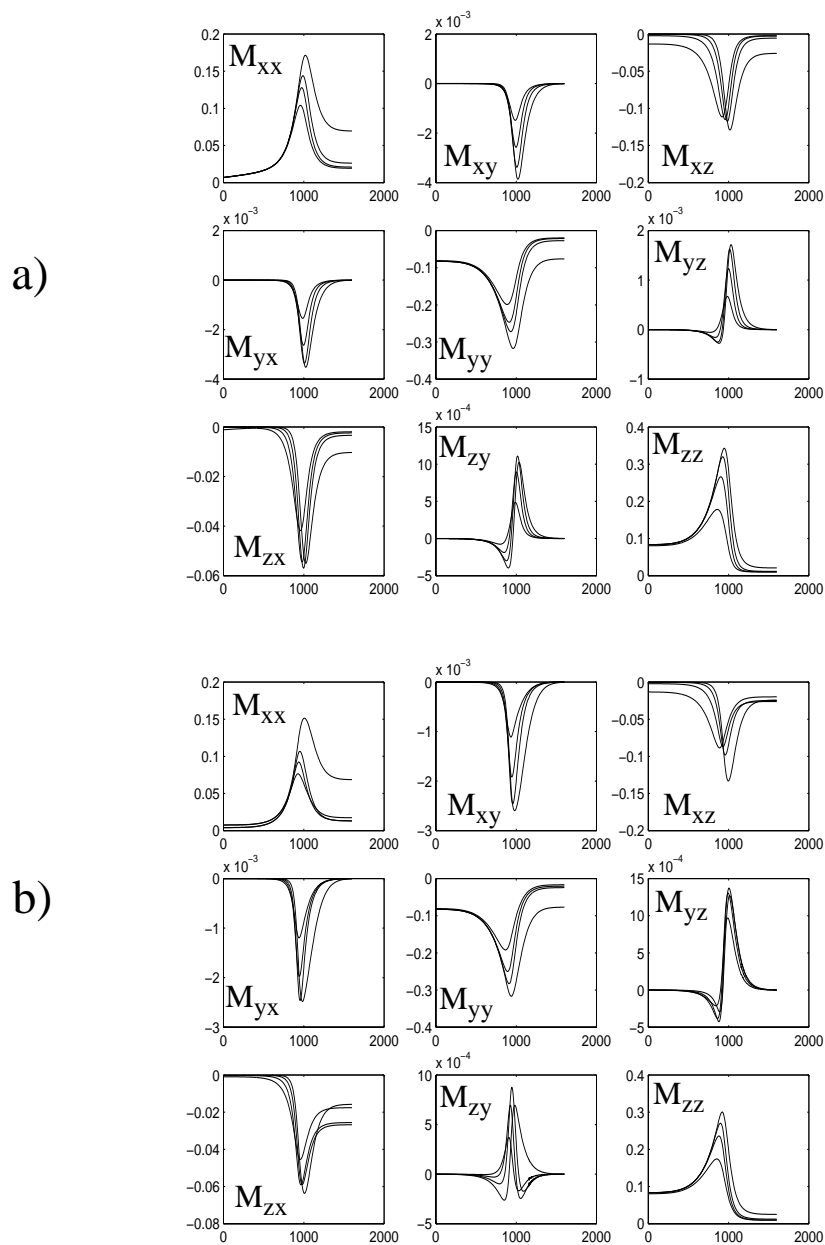
FIGURE 6.6. Adiabatic switching of five cells. The barriers are gradually raised while the driver has constant -1 polarization. The nearest neighbor correlation tensor proper elements for the (a) the exact model, and for (b) NNPC.

Table 6.1. Number of (real) state variables as the functions of the number of QCA cells for the Hartree-Fock model, the nearest neighbor pair correlations only model (NNPC), the pair correlations only model (NNPC), and the density matrix description.

# of cells	Hartree-Fock approximation	NN pair correlations only approximation	Pair correlations only approximation	Exact model (twice the # of elements in the density matrix)
1	3	3	3	8
2	6	15	15	32
3	9	27	36	128
5	15	51	105	2048
10	30	111	435	2097152
15	45	172	990	2.147×10^9
...	...	...	...	...
N	3N	3N+ 9(N-1)= 12N-9	3N+ 9N(N-1)/2= $4.5N^2$-1.5N	2^{2N+1}

The simulations were done by solving the (5.32-5.35) differential equations numerically. Stiff ODE solvers must have been used. The best choice seemed to be the *ode15s* solver of MATLAB, restricting the maximum order of the method to 1 and restricting the maximum time step to 0.2. The initial state was generated from the stationary state coming from the exact model with the many body Hamiltonian. It had to be refined to make all the time derivatives of PC/NNPC zero. In other words, the stationary states from the exact model and for the PC/NNPC are numerically slightly different. Starting the simulation from the stationary state of the exact model can cause

oscillations. For the refinement a minimization algorithm was used trying to make the derivatives zero.

6.1.2 The validity of the approximations

It is important to check whether the assumptions used for the approximation for PC and NNPC are valid. PC approximates the three-point correlations supposing that the elements of the three-point correlation tensors proper are zero. NNPC approximates even the next-to-nearest neighbor two-point correlations based on the assumption that the elements of the next-to-nearest neighbor two-point correlation tensors proper are zero. In this subsection it will be examined through a concrete simulation example whether these assumptions are fulfilled or no.

The simulation example for which the validity of the approximations will be checked is the adiabatic switching of a line of five cells. The simulation results have already been presented in Fig. 6.5 and Fig 6.6. First it will be checked whether the elements of the three-point correlation tensors proper are sufficiently small. Not all of them must be checked since not all of the correlations were approximated by PC, only the 14 of the possible 3x3x3=27 three-point correlations. The absolute maxima of these are summarized in Table 6.2(a). (E.g., zzx refers to the maximum of $abs(M_{zzx}(i, i + 1, i + 2))$ during the whole time evolution.) Table 6.2(b) shows the maxima of the 10 correlation tensor proper elements which are assumed to be zero by NNPC. For comparison, the absolute maxima of the two-point correlation tensor proper elements are shown in Table 6.2.(c). (E.g., zz refers to the maximum of $abs(M_{zz}(i, i + 1))$ during the whole time evolution.)

Table 6.2. (a) The maxima of the largest elements of the three-point correlation tensor propers for the three-point correlations approximated by PC. (b) The same for NNPC. (c) The maxima of the elements of the two-point correlation tensor proper for comparison.

	Abs. Max.			Abs. Max.			Abs. Max.
zzx	0.081		zyy	0.071		zz	0.342
zyy	0.071		zxz	0.068		yy	0.317
zxz	0.068		zxx	0.034		xx	0.167
zxx	0.034		yyz	0.026		xz	0.132
yyz	0.026		xxz	0.020		zx	0.061

<div align="center">(a)   (b)   (c)</div>

Next it will be checked whether the elements of the further-than-nearest neighbor pair correlation tensors proper are small. Fig. 6.7 shows the absolute maxima of the elements of the two-point correlation tensors proper $\hat{M}(i, i + dist)$ as the function of the *dist* intercell distance. *dist*=1 and *dist*=2 correspond to nearest neighbor and next-to-nearest neighbor correlations, respectively. According to the figure, the pair correlations decrease rapidly with the distance.

In summary, in the simulation example presented above, the assumptions on which the approximation were based, seem to be valid.

.

distance
between cells
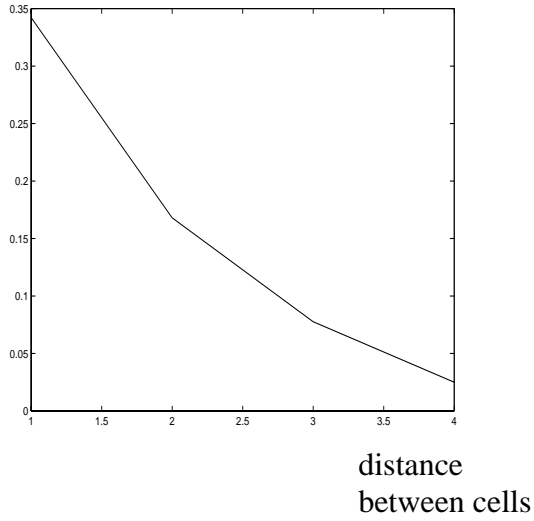
FIGURE 6.7. Absolute maximum of the elements of the *M(i,i+dist)* pair correlation tensor proper as the function of intercellular distance.

6.1.3 Stationary solution of the dynamical equations

The stationary states of PC/NNPC can be obtained taking all the time derivatives zero in the dynamical equations and solving for the coherence vector and correlation tensor elements. The dynamics of the system can be written in the general form:

$$\frac{d}{dt}\vec{\Lambda} = F(\vec{\Lambda}). \tag{6.7}$$

Here $\vec{\Lambda}$ is a column vector containing coherence vector and correlation tensor elements and $F(\vec{\Lambda})$ is a vector-valued function of the vector variable $\vec{\Lambda}$. The stationary solution can be obtained from

$$0 = F(\vec{\Lambda}_{stat}). \tag{6.8}$$

154

Several numerical techniques can be used to find $\vec{\Lambda}_{stat}$. It can be found through the minimization of $\|F(\vec{\Lambda})\|$. Other possibility is the generalized Newton-Raphson method. It converges very fast since $F(\vec{\Lambda})$ contains mostly linear terms, except for the terms approximating the three-point correlations.

The generalized Newton-Raphson method is based on the linearization of $F(\vec{\Lambda})$ around an initial guess, $\vec{\Lambda}_{ini}$. The next guess, $\vec{\Lambda}_{next}$, will be the vector that makes the linearized function zero. The linearization of $F(\vec{\Lambda})$ is

$$F(\vec{\Lambda}) - F(\vec{\Lambda}_{ini}) \approx J(\vec{\Lambda}_{ini})(\vec{\Lambda} - \vec{\Lambda}_{ini}). \qquad (6.9)$$

Here $J(\vec{\Lambda}_{ini})$ is the Jacobian of $F(\vec{\Lambda})$ at $\vec{\Lambda}_{ini}$. Since we are looking for the zero of $F(\vec{\Lambda})$, the following equation must be solved for $\vec{\Lambda}_{next}$:

$$-F(\vec{\Lambda}_{ini}) = J(\vec{\Lambda}_{ini})(\vec{\Lambda}_{next} - \vec{\Lambda}_{ini}). \qquad (6.10)$$

The solution is

$$\vec{\Lambda}_{next} = \vec{\Lambda}_{ini} - J^{-1}(\vec{\Lambda}_{ini})F(\vec{\Lambda}_{ini}). \qquad (6.11)$$

This gives the next guess from the previous guess. Notice that the Jacobian must be invertible since (6.11) explicitly contains its inverse. The Jacobian is singular if there is no dissipation, thus adding (even very small) decoherence terms to the equations (See Section 5.1.7.) is necessary to find the stationary states. It is reasonable to determine the Jacobian analytically instead of using numerical differentiation in order to increase the computation speed and the accuracy as well.

6.1.4 Conclusions

A method was shown how to truncate the system of dynamical equations obtained from the coherence vector formalism. The Pair Correlation ("PC") model kept all the two-point correlations while approximation the three-point correlations. The Nearest Neighbor Pair Correlation ("NNPC") model approximated even the non-nearest neighbor pair correlations. The usefulness of these models can be summarized as follows. (1) They *quantitatively* improve the dynamics of the coherence vectors comparing to the mean-field (Hartree-Fock) model. (2) They represent also a *qualitative* improvement since they give the (approximate) dynamics of the correlation while mean-field models do not give information on correlation. (3) These approximate models help understating which quantum degrees of freedom are important from the point of view of the dynamics.

6.2 Modeling the majority gate with unequal input legs

Self-consistent mean-field type (self-consistent Hartree-Fock) methods usually give even quantitatively good results in determining the instantaneous ground state of adiabatically switched QCA circuits. In this section a counter example, the so-called majority logic gate with unequal input legs is presented. For this gate the results of the mean-field type approximation are qualitatively wrong. An improved version of the self-consistent mean-field approximation is presented which by including correlation effects determines the ground state correctly.

The basis of the self-consistent mean-field method is the self-consistent iteration of the single-cell time-independent Scrödinger equations:

$$\hat{H}_i \Psi_i = E_i \Psi_i. \tag{6.12}$$

The Ψ_i cell state can be expressed as the linear combination of the polarization +1 and -1 states:

$$\Psi_i = \alpha_i |1\rangle + \beta_i |-1\rangle = \begin{bmatrix} \alpha_i \\ \beta_i \end{bmatrix}. \tag{6.13}$$

The Hamiltonian is

$$\hat{H}_i = -\gamma \hat{\sigma}_{xi} + \frac{1}{2}\hat{\sigma}_{zi} E_{\Sigma i}. \tag{6.14}$$

Here γ is the interdot tunneling energy. The single cell Hamiltonian is coupled to the neighboring cells through $E_{\Sigma i}$ which is the weighted sum:

$$E_{\Sigma i} = -\sum_j E_{ij} \langle \hat{\sigma}_{zi} \rangle. \tag{6.15}$$

The E_{ij} electrostatic intercell coupling is E_0 for horizontal and vertical nearest neighbors, -$0.18 E_0$ for diagonal neighbors and zero for others. (The minus sign is used for consistency reasons.)

It is convenient to define a new quantity, the charge polarization of a cell, as

$$P_i = |\alpha_i|^2 - |\beta_i|^2. \tag{6.16}$$

Equivalently, it can be written as well as the expectation value of the $\hat{\sigma}_{zi}$ Pauli spin matrix:

$$P_i = -\langle \hat{\sigma}_{zi} \rangle. \tag{6.17}$$

With the polarizations of the neighbors (6.15) can be rewritten as

$$E_{\Sigma i} = \sum_j E_{ij} P_j. \tag{6.18}$$

It can be proved[52] that to compute the polarization corresponding to the lowest energy eigenstate of the single-cell Hamiltonian is equivalent to

$$P_i = \frac{\dfrac{E_{\Sigma i}}{2\gamma}}{\sqrt{1 + \left(\dfrac{E_{\Sigma i}}{2\gamma}\right)^2}}, \tag{6.19}$$

which gives the steady-state polarization of a cell as the function of the polarizations of its neighbors. (See Sec. 4.1.2) Thus this formula will be iterated instead of the single cell time-independent Scrödinger equation. In this section a concrete example will be considered for which the self-consistent mean field method gives qualitatively wrong results.

6.2.1 Posing the problem

The circuit under consideration can be seen in Fig. 6.8. It is a majority gate with unequal input legs. One of the input legs is only one cell long and coupled to a driver cell ($P_{driver3}$) with polarization -1. The other two input legs are longer (their length will be denoted by L) and they are coupled to drivers ($P_{driver1}$, $P_{driver2}$) with polarization +1.

When the gate is adiabatically switched, starting out from ground state, the interdot barriers are raised gradually. Due to the adiabatic theorem the system stays constantly in its ground state. When the barriers are high (the tunneling energy is low), the ground polarization of the output of the majority gate is the majority of the polarizations of the input drivers. The results of the self-consistent method for a seven-cell majority gate (L=2) can be seen in Fig. 6.9. The interdot tunneling barriers are gradually raised (the gamma tunneling energy is gradually decreased) as shown in Fig. 6.9(a). At the end the output cell has +1 polarization as can be seen from the dynamics of the cell polarizations shown in Fig. 6.9(b). For comparison, the cell polarizations of the exact instantaneous
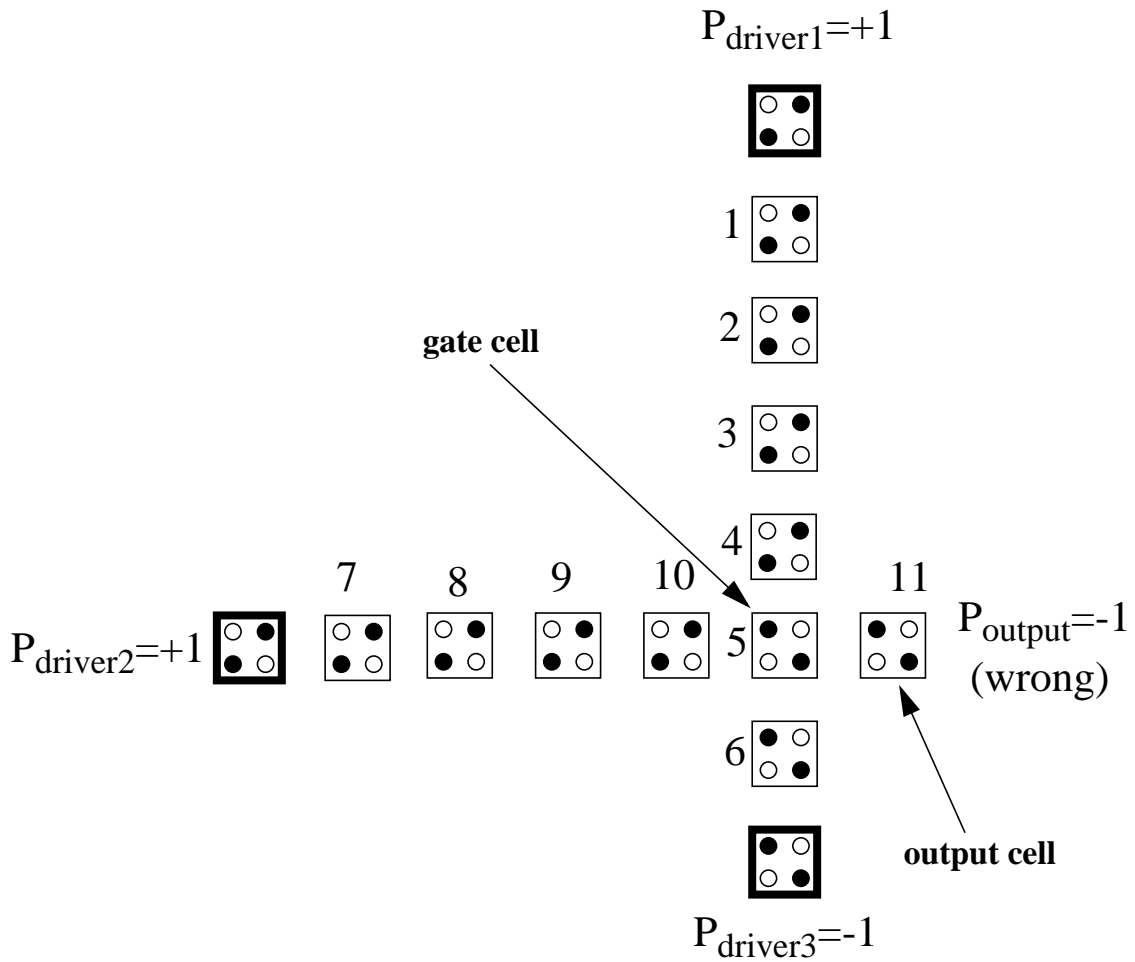
FIGURE 6.8. 11-cell majority gate with unequal input legs. At the end of the adiabatic switching process, when the barriers are high, the output polarization of the majority gate should be the majority polarization of the inputs. The self-consistent mean-field calculation gives a qualitatively wrong answer predicting -1 for the output polarization.

ground state are also shown in Fig 6.9(c). It can be seen in Fig 6.9(b-c), that at the end all the cells have +1 polarization except for the bottom neighbor of the gate cell which settles in the polarization -1 state.
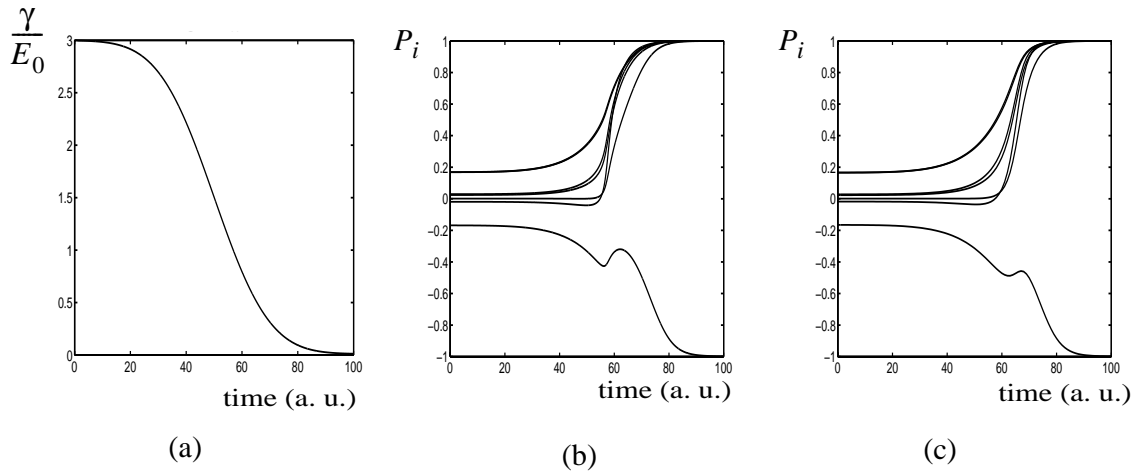
FIGURE 6.9. Adiabatic switching of a 7-cell majority gate (L=2). (a) The time dependence of the tunneling energy. The barriers are gradually raised. (b) The cell polarizations as the function of time for the self-consistent mean field method and (c) for the exact model.

If a cell is added to the long input legs (*L*=3) then the self-consistent method gives qualitatively wrong answer since at the end of the adiabatic switching process the output polarization is -1. Fig. 6.10(a) and (b) show the instantaneous ground state cell polarizations computed with the self-consistent method and obtained from the exact solution of the time-independent Scrödinger equation of the whole system, respectively. As it can be seen in Fig. 6.10(a), three of the nine cells settle in the -1 polarization state. (These are the gate cell, the bottom neighbor of the gate cell, and the output cell.)

FIGURE 6.10. Adiabatic switching of a 9-cell majority gate (L=3). (a) The cell polarizations as the function of time for the self-consistent mean field method and (b) for the exact model.

Up to now it was not explained exactly how the starting guess of the self-consistent solution is obtained. At a time instant $t+\Delta t$, the polarizations computed for time t are used as initial guess. It seems to be reasonable to check whether there is another stationary state of the self-consistent algorithm with lower energy, using another initial guess at each time instant. The results are shown in Fig 6.11(a) using P_i=+1 as initial guess. The polarization of the output cell is now P=+1, as it is expected in case of correct operation.

FIGURE 6.11. Adiabatic switching of a 9-cell majority gate (L=3). (a) The cell polarizations as the function of time for the self-consistent mean field method when the P_i=+1 initial guess is used for iterations. (b) The polarization of the gate cell for the self-consistent mean field using the two different initial guesses for iteration. (c) Energies of the majority gate for the two cases. For t<60 the polarizations and the energies they are the same for both cases.

In order to determine which of the two methods give the ground state, it is necessary to compute their energies. The energy is computed as

$$ E = \sum_{i \notin C_D} -\gamma \langle \hat{\sigma}_{xi} \rangle - \frac{1}{2} \sum_i \sum_{j < i} E_{ij} \langle \hat{\sigma}_{zi} \rangle \langle \hat{\sigma}_{zj} \rangle \text{, where} \tag{6.20} $$

in ground state

$$ \langle \hat{\sigma}_{xi} \rangle = \sqrt{1 - P_i^2}, \ \langle \hat{\sigma}_{yi} \rangle = 0 \text{, and } \langle \hat{\sigma}_{zi} \rangle = -P_i. \tag{6.21} $$

In (6.20) the driver cells are also included in the second sum although they are unnumbered in Fig. 6.8. The drivers are not included in the first sum since their barriers are high. C_D denotes the set of drivers.

The dynamics of the gate cell polarization and the energies of the instantaneous ground state is shown for the two methods in Fig 6.11(b) and (c). For t<60 they give the same results. At t=60 there is an abrupt jump in the ground state given by the method

162

using P_i=+1 as initial guess. For t>60 it gives a qualitatively correct ground state unlike the case when the previous cell polarizations were used as initial guess. (Notice, that except for one all the cells have +1 polarization in Fig 6.11(a), as it is expected for the true ground state.). Thus the self-consistent method has a stationary state which could be a qualitatively correct ground state, however, it cannot find it if the cell polarization in the previous time instant is used as the starting point of the iteration. At about t=80 this stationary becomes the ground state and the "old" ground state becomes an excited state as can be seen in Fig. 6.11(c).

Intuitively, the reason for the failure of the self-consistent method in modeling the majority gate with unequal input legs can be understood as follows. The effect of the driver of the short leg reaches the gate cell before the effect of the drivers of the long legs. It sets the polarization of the gate cell and the output cell to -1. Later when the effect of the other two drivers reaches the gate cell, they will be not able to flip it into +1 polarization. Notice that at this moment two of the neighbors of the gate cell has +1 polarization, the other two has -1.

6.2.2 Solution

Our goal is to construct an intermediate model between the self-consistent mean field method and the exact model solving the time independent Scrödinger equation of the whole system. (Modeling the whole gate with one many-body Hamiltonian would require so many state variables that above 10-15 cells it is not feasible.) In order to do that it must be examined which cell of the majority gate could still be modeled with the mean-field approach and which should be modeled by a better method. The mean-field method

assumes that the system is in a product state and the cells are uncorrelated. Thus it seems to be reasonable to check how large the two-point, three-point, etc. correlations are in different part of a, let say, 11-cell (L=3) majority gate.

The two-point correlation of cells i and j can be characterized by the two-point correlation tensor with elements:

$$M_{ab}(1, 2) = \left\langle \left[\hat{\sigma}_a(1) - \langle \hat{\sigma}_b(1) \rangle \right] \left[\hat{\sigma}_b(2) - \langle \hat{\sigma}_b(2) \rangle \right] \right\rangle; \qquad a, b = x, y, z. \quad (6.22)$$

All the nine elements of this tensor are zero if the two cells are uncorrelated.

Our examinations show that the correlations are large in the "cross" region around the gate cell. Fig. 6.12 shows the time dependence of $M_{zz}(1,2)$, $M_{zz}(4,5)$ and $M_{zz}(5,11)$. It can be seen that the latter two (corresponding to correlation in the cross region) are much larger. Thus it seems to be reasonable to model the five cells of the cross with a five-cell
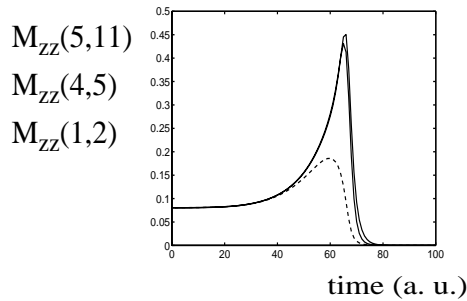
FIGURE 6.12. Dynamics of the two-point correlations during the adiabatic switching of a 11-cell majority gate (L=4). $M_{zz}(1,2)$ (dashed), $M_{zz}(4,5)$ (solid) and $M_{zz}(5,11)$ (solid) are shown. The correlations are much larger in the cross region than away from it.

Hamiltonian. The genuflection with the lowest energy would give the five cell ground state. The remaining cells can be modeled by self consistent mean-field. The two regions are connected also in a self-consistent manner.

Simulation show that this approximation give the correct output for L<40. (Notice the large improvement comparing to the self-consistent mean-field method that worked correctly for L<2.) Fig. 6.13 shows the results for the 11-cell gate (L=4) comparing it to that of the exact model and of the self-consistent mean field.
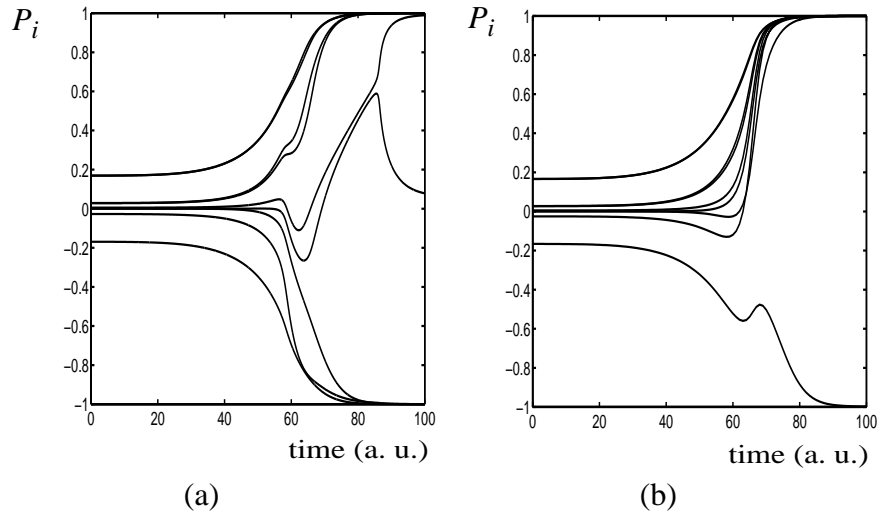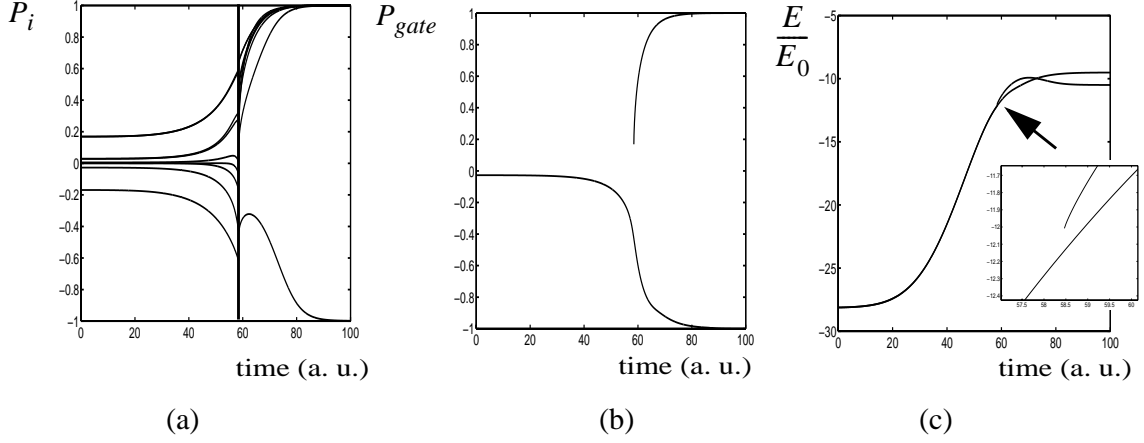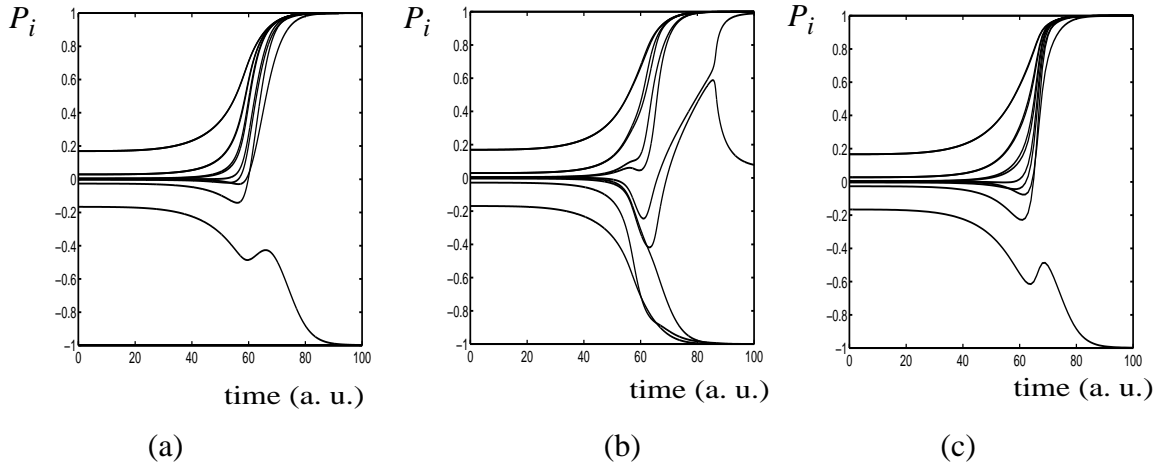

FIGURE 6.13. Adiabatic switching of a 11-cell majority gate (L=4). (a) The cell polarizations as the function of time. The cross region is modeled with a five-cell Hamiltonian while the remaining cells are modeled with self-consistent mean-field. (b)The same for the self-consistent mean-field method and (c) for the exact model.

It is also interesting to see how much the correlations are restored in the cross region by our approximation. Fig. 6.14(a) shows some of the two-point correlations in the cross region. (Compare with the solid curves of Fig. 6.12.) For example, if the seven-cell cross (obtained by attaching one cell from the top and one cell from the left to the five-cell cross) is modeled with a many-cell Hamiltonian then the level of restoration is even better as can be seen in Fig. 6.14(b).

$M_{zz}(5,11)$

$M_{zz}(4,5)$

$M_{zz}(5,11)$

$M_{zz}(4,5)$

time (a. u.)

time (a. u.)

(a)

(b)
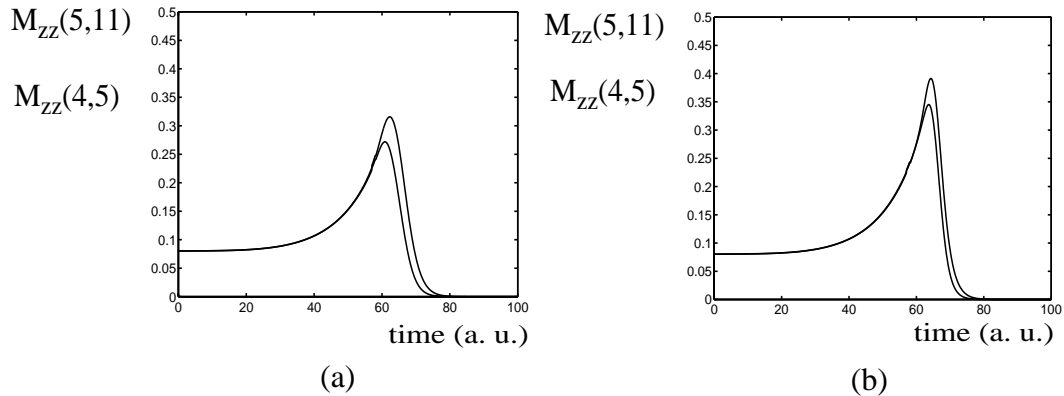
FIGURE 6.14. Dynamics of the two-point correlations during the adiabatic switching of a 11-cell majority gate (L=4) when the cross region is simulated with a many-cell Hamiltonian. $M_{zz}(4,5)$ and $M_{zz}(5,11)$ are shown using (a) a five-cell cross and (b) a seven-cell Hamiltonian for the cross. Compare with the solid lines of Fig. 6.12.

The number of output cells can be increased adding new cells to the cross and modeling these cells together with the cross with one many-cell Hamiltonian. One might try to attach output cells modeled with self-consistent mean-field, however, more than two or three additional cells cause the method to fail to give the right output. Another solution could be to attach a line of output cell to the cross which are modeled by a separate many cell Hamiltonian as shown. The advantage of using two separate many-cell Hamiltonian instead of one is the large decrease in the number of state variables. For example, a 5-cell cross with two extra output cells is modeled with a many-cell Hamiltonian, and 5 additional output cells are attached to it modeled by a separate many-cell Hamiltonian then the method gives the correct output for L<36.

Originally it was thought that the self-consistent mean-field approach fails for the majority gate since, because of the inequality of the input legs, the effect of one of the drivers reaches the gate cell before the other two. The findings of this section support the

idea that what caused the self-consistent mean-field approach to fail was its inability of modeling the correlations in the cross region. The different length of the input legs is not the main reason for the failure, since even with the new method they are modeled by self-consistent mean-field. In summary, the competing inputs lead to failure of finding the ground state only because of neglecting quantum correlation in the cross regions. As a consequence, long-range quantum correlations and entanglement, at least in the (possibly relatively long) input legs, are not necessary for the correct operation of the majority gate.

Originally it was thought that the self-consistent mean-field approach fails for the majority gate since, because of the inequality of the input legs, the effect of one of the drivers reaches the gate cell before the other two. The findings of this section support the idea that what caused the self-consistent mean-field approach to fail was its inability of modeling the correlations in the cross region. The different length of the input legs is not the main reason for the failure, since even with the new method they are modeled by self-consistent mean-field. In summary, the competing inputs lead to failure of finding the ground state only because of neglecting quantum correlation in the cross regions. As a consequence, long-range quantum correlations and entanglement, at least in the (possibly relatively long) input legs, are not necessary for the correct operation of the majority gate.

6.2.3 Delayed-gate approximation

When simulating the behavior of an adiabatically switched QCA circuit, it may be cumbersome to divide the cells into groups in order to provide that the simulations give the correct result. A very simple *ad hoc* method will be proposed which, by applying it to

the self-consistent mean-field approach, leading to the qualitatively correct modeling of

the majority gate.

As it was seen, it can lead to wrong results for the self-consistent mean-field

method, if the effect of one input reaches the gate cell much earlier than the others. The

problem of the competing inputs can be solved if the polarization of the gate cell is fixed

to zero until at least three of its four neighbors has a sufficiently large (e. g., $|P_i|>0.35$)

polarization. Thus the driver with the shortest input leg cannot flip the gate cell and the

output cell just because it is closer. Fig. 6.15 shows the results of an 11-cell gate (L=4)

with four extra output cells.
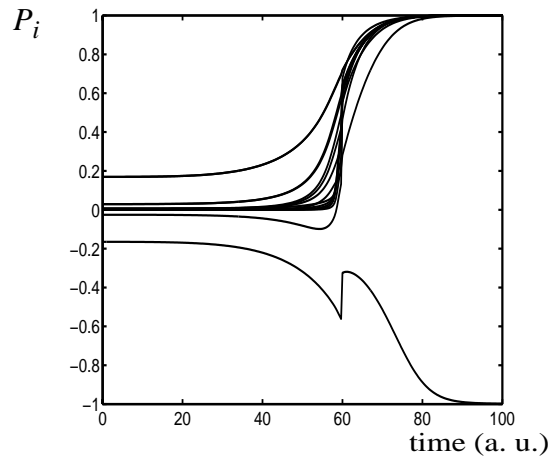
FIGURE 6.15. Adiabatic switching of a 11-cell majority gate (L=4) with four output cells. The cell polarization as the function of time for the delayed gate mean-field approximation.

6.2.4 Conclusions

A method was presented for modeling the majority gate of Quantum-dot Cellular

Automata cells with unequal input legs. The self-consistent mean-field type

approximation fails to determine the ground state correctly when the gate is adiabatically

switched. It was found that if the five-cell cross region of the majority gate is modeled with a many-body Hamiltonian while all the other cells are still modeled by the mean-field method, the ground state of the system is determined qualitatively correctly up to a very large difference in the length of the input legs. After the theoretical analysis, an *ad-hoc* method, the delayed-gate approximation was proposed to provide the qualitatively correct ground state not only for a majority gate, but even for more complicated QCA circuits.

APPENDIX A

DYNAMICS OF THE CORRELATIONS FOR TWO QCA CELLS

The correlation of two QCA cells is described by the 9 element correlation tensor which has the elements of the form:

$$K_{ij} = \langle \hat{\sigma}_i(1)\hat{\sigma}_j(2)\rangle; \qquad\qquad i, j = x, y, z. \qquad (A.1)$$

In order to get the dynamics of the K_{ij}'s, first the dynamics of the dynamics of the $\hat{\sigma}_i(1)\hat{\sigma}_j(2)$ terms must be computed then the expectation values will give the dynamics for the elements of the correlation tensor. The computations will be given in full detail for one element of the correlation tensor (K_{yz}), while for the other elements only the final result is presented.

The dynamics of the $\hat{\sigma}_i(1)\hat{\sigma}_j(2)$ terms can be obtained from the equation giving the time dependence of an operator in the Heisenberg picture:

$$i\hbar\frac{\partial}{\partial t}\hat{O} = [\hat{O}, \hat{H}], \qquad (A.2)$$

where Hamiltonian for the two-cell system is:

$$\hat{H} = -\gamma_1\hat{\sigma}_x(1) - \gamma_2\hat{\sigma}_x(2) + \frac{E_k}{2}\hat{\sigma}_z(1)\hat{\sigma}_z(2). \qquad (A.3)$$

To get the time dependence of K_{yz}, the time dependence of $\hat{\sigma}_y(1)\hat{\sigma}_z(2)$ must be obtained with (A.2):

$$\frac{d}{dt}(\hat{\sigma}_y(1)\hat{\sigma}_z(2)) = \frac{i}{\hbar}\left[-\gamma_1\hat{\sigma}_x(1) - \gamma_2\hat{\sigma}_x(2) - \frac{E_k}{2}\hat{\sigma}_z(1)\hat{\sigma}_z(2), \hat{\sigma}_y(1)\hat{\sigma}_z(2)\right]. \qquad (A.4)$$

170

The commutator relations for the relevant terms are:

$$[-\gamma_1\hat{\sigma}_x(1), \hat{\sigma}_y(1)\hat{\sigma}_z(2)] = -\gamma_1[\hat{\sigma}_x(1), \hat{\sigma}_y(1)]\hat{\sigma}_z(2) = \quad\quad (A.5)$$
$$-\gamma_1(2i\hat{\sigma}_z(1))\hat{\sigma}_z(2) = -2i\gamma_1\hat{\sigma}_z(1)\hat{\sigma}_z(2),$$

$$[-\gamma_2\hat{\sigma}_x(2), \hat{\sigma}_y(1)\hat{\sigma}_z(2)] = -\gamma_2\hat{\sigma}_y(1)[\hat{\sigma}_x(2), \hat{\sigma}_z(2)] = \quad\quad (A.6)$$
$$-\gamma_2\hat{\sigma}_y(1)(-2i\hat{\sigma}_y(2)) = 2i\gamma_2\hat{\sigma}_y(1)\hat{\sigma}_y(2),$$

$$\left[-\frac{E_k}{2}\hat{\sigma}_z(1)\hat{\sigma}_z(2), \hat{\sigma}_y(1)\hat{\sigma}_z(2)\right] = -\frac{E_k}{2}[\hat{\sigma}_z(1), \hat{\sigma}_y(1)](\hat{\sigma}_z(2))^2 = \quad\quad (A.7)$$
$$-\frac{E_k}{2}(-2i\hat{\sigma}_x(1)) = iE_k\hat{\sigma}_x(1).$$

After substituting (A.5-A.7) into (A.4), the following equation is obtained:

$$\hbar\frac{d}{dt}(\hat{\sigma}_y(1)\hat{\sigma}_z(2)) = 2\gamma_1\hat{\sigma}_z(1)\hat{\sigma}_z(2) - 2\gamma_2\hat{\sigma}_y(1)\hat{\sigma}_y(2) - E_k\hat{\sigma}_x(1). \quad\quad (A.8)$$

Taking the expectation values one gets:

$$\hbar\frac{d}{dt}\langle\hat{\sigma}_y(1)\hat{\sigma}_z(2)\rangle = 2\gamma_1\langle\hat{\sigma}_z(1)\hat{\sigma}_z(2)\rangle - 2\gamma_2\langle\hat{\sigma}_y(1)\hat{\sigma}_y(2)\rangle - E_k\langle\hat{\sigma}_x(1)\rangle. \quad (A.9)$$

Substituting the coherence vector and correlation tensor elements in the place of expectation values the dynamics of K_{yz} is given as:

$$\hbar\frac{dK_{yz}}{dt} = 2\gamma_1 K_{zz} - 2\gamma_2 K_{yy} - E_k\lambda_x(1). \quad\quad (A.10)$$

For the other eight elements the computations are very similar. The time dependence of the nine elements of the correlation tensor can be given as:

$$\hbar\frac{d}{dt}\begin{bmatrix} K_{xx} \\ K_{xy} \\ K_{xz} \\ K_{yx} \\ K_{yy} \\ K_{yz} \\ K_{zx} \\ K_{zy} \\ K_{zz} \end{bmatrix} = \begin{bmatrix} 0 & 0 & 0 & 0 & 0 & 0 & 0 & 0 & 0 \\ 0 & 0 & 2\gamma_2 & 0 & 0 & 0 & 0 & 0 & 0 \\ 0 & -2\gamma_2 & 0 & 0 & 0 & 0 & 0 & 0 & 0 \\ 0 & 0 & 0 & 0 & 0 & 0 & 2\gamma_1 & 0 & 0 \\ 0 & 0 & 0 & 0 & 0 & 2\gamma_2 & 0 & 2\gamma_1 & 0 \\ 0 & 0 & 0 & 0 & -2\gamma_2 & 0 & 0 & 0 & 2\gamma_1 \\ 0 & 0 & 0 & -2\gamma_1 & 0 & 0 & 0 & 0 & 0 \\ 0 & 0 & 0 & 0 & -2\gamma_1 & 0 & 0 & 0 & -2\gamma_2 \\ 0 & 0 & 0 & 0 & 0 & -2\gamma_1 & 0 & -2\gamma_2 & 0 \end{bmatrix}\begin{bmatrix} K_{xx} \\ K_{xy} \\ K_{xz} \\ K_{yx} \\ K_{yy} \\ K_{yz} \\ K_{zx} \\ K_{zy} \\ K_{zz} \end{bmatrix} + E_k \begin{bmatrix} 0 \\ 0 \\ \lambda_y(1) \\ 0 \\ 0 \\ -\lambda_x(1) \\ \lambda_y(2) \\ -\lambda_x(2) \\ 0 \end{bmatrix}$$

To check the manual symbolical computations, an object oriented program was written in

MATLAB handling Pauli spin matrices symbolically. Its output is given in Fig. A.1.

```
>> CorrDynTwoCells
**********************************************************
Dynamical equation for the correlation tensor of two cells
   computed from the two-cell Hamiltonian symbolically
**********************************************************

   The form of the equation is:

        dKvector
hbar * ---------- = CoeffMatrix*Kvector+Ek*<RemVector>
           dt

   where

CoeffMatrix =

[    0,    0,    0,    0,    0,    0,    0,    0,    0]
[    0,    0,  ga2,    0,    0,    0,    0,    0,    0]
[    0, -ga2,    0,    0,    0,    0,    0,    0,    0]
[    0,    0,    0,    0,    0,    0,  ga1,    0,    0]
[    0,    0,    0,    0,    0,  ga2,    0,  ga1,    0]
[    0,    0,    0,    0, -ga2,    0,    0,    0,  ga1]
[    0,    0,    0, -ga1,    0,    0,    0,    0,    0]
[    0,    0,    0,    0, -ga1,    0,    0,    0,  ga2]
[    0,    0,    0,    0,    0, -ga1,    0, -ga2,    0]

   and

RemVector =

    '0'
    '0'
    'y1'
    '0'
    '0'
    '(-1)*x1'
    'y2'
    '(-1)*x2'
    '0'


Here the correlation is described by Kvector that
is a 9 element column vector:
                                          T
Kvector=[<x1x2> <x1y2> <x1z2> ... <z1z2>]


>>
```

FIGURE A.1.Output of the MATLAB program computing the dynamics of the correlation tensor symbolically for two coupled cells. *ga1*, *ga2* stand for γ_1 and γ_2. *xn*, *yn* and *zn* (*n*=1,2) are shorthand notations for $\hat{\sigma}_x(n)$, $\hat{\sigma}_y(n)$ and $\hat{\sigma}_z(n)$.

```
>> CorrDyn
***********************************************************
Dynamical equation for the correlation tensor of cells#2/3
   computed from the four-cell Hamiltonian symbolically
***********************************************************

    The form of the equation is:

         dKvector23
hbar * ---------- = CoeffMatrix*Kvector+Ek*<RemVector>
             dt

    where

CoeffMatrix =

[    0,    0,    0,    0,    0,    0,    0,    0,    0]
[    0,    0,  ga3,    0,    0,    0,    0,    0,    0]
[    0, -ga3,    0,    0,    0,    0,    0,    0,    0]
[    0,    0,    0,    0,    0,    0,  ga2,    0,    0]
[    0,    0,    0,    0,    0,  ga3,    0,  ga2,    0]
[    0,    0,    0,    0, -ga3,    0,    0,    0,  ga2]
[    0,    0,    0, -ga2,    0,    0,    0,    0,    0]
[    0,    0,    0,    0, -ga2,    0,    0,    0,  ga3]
[    0,    0,    0,    0,    0, -ga2,    0, -ga3,    0]

    and

RemVector =

    'z1*y2*x3+x2*y3*z4'
    'z1*y2*y3+(-1)*x2*x3*z4'
    'z1*y2*z3+y2'
    '(-1)*z1*x2*x3+y2*y3*z4'
    '(-1)*z1*x2*y3+(-1)*y2*x3*z4'
    '(-1)*z1*x2*z3+(-1)*x2'
    'y3+z2*y3*z4'
    '(-1)*x3+(-1)*z2*x3*z4'
    '0'


Here the correlation is described by Kvector23 that
is a 9 element column vector:
                                              T
Kvector23=[<x2x3> <x2y3> <x2z3> ... <z2z3>]
```

FIGURE B.1. Output of the MATLAB program computing the dynamics of the correlation tensor symbolically for cell #2 and #3 of a line of cells. *ga2*, *ga3* stand for γ_2 and γ_3. *xn*, *yn* and *zn* (*n*=1,2,..) are shorthand notations for $\hat{\sigma}_x(n)$, $\hat{\sigma}_y(n)$ and $\hat{\sigma}_z(n)$.

```
>> CorrDyn2
***********************************************************
Dynamical equation for the correlation tensor of cells#2/4
   computed from the five-cell Hamiltonian symbolically
***********************************************************

    The form of the equation is:

        dKvector24
hbar * ---------- = CoeffMatrix*Kvector+Ek*<RemVector>
            dt

    where

CoeffMatrix =

[    0,    0,    0,    0,    0,    0,    0,    0,    0]
[    0,    0,  ga4,    0,    0,    0,    0,    0,    0]
[    0, -ga4,    0,    0,    0,    0,    0,    0,    0]
[    0,    0,    0,    0,    0,    0,  ga2,    0,    0]
[    0,    0,    0,    0,    0,  ga4,    0,  ga2,    0]
[    0,    0,    0,    0, -ga4,    0,    0,    0,  ga2]
[    0,    0,    0, -ga2,    0,    0,    0,    0,    0]
[    0,    0,    0,    0, -ga2,    0,    0,    0,  ga4]
[    0,    0,    0,    0,    0, -ga2,    0, -ga4,    0]

    and

RemVector =

    'z1*y2*x4+y2*z3*x4+x2*z3*y4+x2*y4*z5'
    'z1*y2*y4+y2*z3*y4+(-1)*x2*z3*x4+(-1)*x2*x4*z5'
    'z1*y2*z4+y2*z3*z4'
    '(-1)*z1*x2*x4+(-1)*x2*z3*x4+y2*z3*y4+y2*y4*z5'
    '(-1)*z1*x2*y4+(-1)*x2*z3*y4+(-1)*y2*z3*x4+(-1)*y2*x4*z5'
    '(-1)*z1*x2*z4+(-1)*x2*z3*z4'
    'z2*z3*y4+z2*y4*z5'
    '(-1)*z2*z3*x4+(-1)*z2*x4*z5'
    '0'


Here the correlation is described by Kvector24 that
is a 9 element column vector:
                                              T
Kvector24=[<x2x4> <x2y4> <x2z4> ... <z2z4>]
```

FIGURE B.2. Output of the MATLAB program computing the dynamics of the correlation tensor symbolically for cell #2 and #4 of a line of cells. *ga2*, *ga4* stand for γ_2 and γ_4. *xn*, *yn* and *zn* (*n*=1,2,..) are shorthand notations for $\hat{\sigma}_x(n)$, $\hat{\sigma}_y(n)$ and $\hat{\sigma}_z(n)$.

```
>> CorrDyn3
***********************************************************
Dynamical equation for the correlation tensor of cells#2/5
   computed from the six-cell Hamiltonian symbolically
***********************************************************

    The form of the equation is:

        dKvector25
hbar * ---------- = CoeffMatrix*Kvector+Ek*<RemVector>
            dt

    where

CoeffMatrix =

[    0,    0,    0,    0,    0,    0,    0,    0,    0]
[    0,    0,  ga5,    0,    0,    0,    0,    0,    0]
[    0, -ga5,    0,    0,    0,    0,    0,    0,    0]
[    0,    0,    0,    0,    0,    0,  ga2,    0,    0]
[    0,    0,    0,    0,    0,  ga5,    0,  ga2,    0]
[    0,    0,    0,    0, -ga5,    0,    0,    0,  ga2]
[    0,    0,    0, -ga2,    0,    0,    0,    0,    0]
[    0,    0,    0,    0, -ga2,    0,    0,    0,  ga5]
[    0,    0,    0,    0,    0, -ga2,    0, -ga5,    0]

    and

RemVector =

    'z1*y2*x5+y2*z3*x5+x2*z4*y5+x2*y5*z6'
    'z1*y2*y5+y2*z3*y5+(-1)*x2*z4*x5+(-1)*x2*x5*z6'
    'z1*y2*z5+y2*z3*z5'
    '(-1)*z1*x2*x5+(-1)*x2*z3*x5+y2*z4*y5+y2*y5*z6'
    '(-1)*z1*x2*y5+(-1)*x2*z3*y5+(-1)*y2*z4*x5+(-1)*y2*x5*z6'
    '(-1)*z1*x2*z5+(-1)*x2*z3*z5'
    'z2*z4*y5+z2*y5*z6'
    '(-1)*z2*z4*x5+(-1)*z2*x5*z6'
    '0'


Here the correlation is described by Kvector25 that
is a 9 element column vector:
                                              T
Kvector25=[<x2x5> <x2y5> <x2z5> ... <z2z5>]
```

FIGURE B.3. Output of the MATLAB program computing the dynamics of the correlation tensor symbolically for cell #2 and #5 of a line of cells. *ga2*, *ga5* stand for γ_2 and γ_5. *xn*, *yn* and *zn* (*n*=1,2,..) are shorthand notations for $\hat{\sigma}_x(n)$, $\hat{\sigma}_y(n)$ and $\hat{\sigma}_z(n)$.

APPENDIX C

APPROXIMATE DYNAMICAL EQUATIONS FOR THE TWO-POINT CORRELATIONS

In Sec. 6.1 it was shown how to eliminate the three-point correlations from the equations of the two point correlations assuming that the three-point correlation propers are zero. In this Appendix the approximate dynamical equations for the two-point correlations for a cell inside a cell line are given explicitly.

The exact equations of the two-point correlations (rewriting (5.33-5.35))are

$$\hbar \frac{d}{dt}\hat{K}(i, j) \ = \ \hat{\Omega}_j\hat{K}(i, j) - \hat{K}(i, j)\hat{\Omega}_i + E_k\hat{C}(i, j) \,, \tag{C.1}$$

where for nearest neighbors ($j = i+1$)

$$\hat{C}(i, i+1) \ = \ \begin{bmatrix} 0 & 0 & \lambda_y(i) \\ 0 & 0 & -\lambda_x(i) \\ \lambda_y(i+1) & -\lambda_x(i+1) & 0 \end{bmatrix} + \tag{C.2}$$

$$\langle \begin{bmatrix} \sigma_x(i)\sigma_y(i+1) & -\sigma_x(i)\sigma_x(i+1) & 0 \\ \sigma_y(i)\sigma_y(i+1) & -\sigma_y(i)\sigma_x(i+1) & 0 \\ \sigma_z(i)\sigma_y(i+1) & -\sigma_z(i)\sigma_x(i+1) & 0 \end{bmatrix} \sigma_z(i+2)\rangle +$$

$$\langle \begin{bmatrix} \sigma_y(i)\sigma_x(i+1) & -\sigma_x(i)\sigma_x(i+1) & 0 \\ \sigma_y(i)\sigma_y(i+1) & -\sigma_x(i)\sigma_y(i+1) & 0 \\ \sigma_y(i)\sigma_z(i+1) & -\sigma_x(i)\sigma_z(i+1) & 0 \end{bmatrix}^T \sigma_z(i-1)\rangle,$$

and for further than nearest neighbors

$$\hat{C}(i,j) = \left\langle \begin{bmatrix} \sigma_x(i)\sigma_y(j) & -\sigma_x(i)\sigma_x(j) & 0 \\ \sigma_y(i)\sigma_y(j) & -\sigma_y(i)\sigma_x(j) & 0 \\ \sigma_z(i)\sigma_y(j) & -\sigma_z(i)\sigma_x(j) & 0 \end{bmatrix} (\sigma_z(j-1) + \sigma_z(j+1)) \right\rangle + \tag{C.3}$$

$$\left\langle \begin{bmatrix} \sigma_y(i)\sigma_x(j) & -\sigma_x(i)\sigma_x(j) & 0 \\ \sigma_y(i)\sigma_y(j) & -\sigma_x(i)\sigma_y(j) & 0 \\ \sigma_y(i)\sigma_z(j) & -\sigma_x(i)\sigma_z(j) & 0 \end{bmatrix}^T (\sigma_z(i-1) + \sigma_z(i+1)) \right\rangle.$$

Let us consider the dynamics of a single nearest neighbor correlation tensor element:

$$\hbar \frac{d}{dt} K_{xx}(i, i+1) = E_k \left\langle \sigma_x(i)\sigma_y(i+1)\sigma_z(i+2) \right\rangle + E_k \left\langle \sigma_y(i)\sigma_x(i+1)\sigma_z(i-1) \right\rangle . \tag{C.4}$$

This equation can be obtained from (C.1) and (C.2), considering the xx element of the $\hat{K}$ correlation tensor. Notice that on the right hand side of (C.4) $\left\langle \sigma_x(i)\sigma_y(i+1)\sigma_z(i+2) \right\rangle$ and $\left\langle \sigma_y(i)\sigma_x(i+1)\sigma_z(i-1) \right\rangle$ are three-point correlations.

The approximate dynamical equation for the two-point correlation can be obtained using

$$\langle ABC \rangle \approx \langle AB \rangle \langle C \rangle + \langle BC \rangle \langle A \rangle + \langle AC \rangle \langle B \rangle - 2 \langle A \rangle \langle B \rangle \langle C \rangle \tag{C.5}$$

for the three-point correlations. Substituting (C.5) into (C.4) one obtains:

$$\tag{C.6}$$

$$\begin{aligned}
\hbar \frac{d}{dt} K_{xx}(i, i+1) = E_k \{ & K_{xy}(i, i+1)\lambda_z(i+2) + K_{yz}(i+1, i+2)\lambda_x(i) + \\
& K_{xz}(i, i+2)\lambda_y(i+1) - 2\lambda_x(i)\lambda_y(i+1)\lambda_z(i+2) + \\
& K_{yx}(i, i+1)\lambda_z(i-1) + K_{xz}(i+1, i-1)\lambda_y(i) + \\
& K_{yz}(i, i-1)\lambda_x(i+1) - 2\lambda_y(i)\lambda_x(i+1)\lambda_z(i-1) \} .
\end{aligned}$$

Notice that now on the right hand side there are only two-point correlations (e. g., $K_{xy}(i, i+1)$) and coherence vector elements (e. g., $\lambda_z(i+2)$), but there are no three-point correlations.

Similar transformations can be made with all the dynamical equations for the two-point correlations, eliminating the three-point correlations from the equations. The model obtained this way considers only the two-point correlations and neglects higher order correlations. (It was called "PC" referring to pair correlation.)

Further simplification can be done by approximating the next-to-nearest neighbor correlations by the multiplication of two coherence vector elements, e.g., $K_{xz}(i, i + 2) = \lambda_x(i)\lambda_z(i + 2)$. Changing (C.6) according to this results in

$$
\hbar\frac{d}{dt}K_{xx}(i, i + 1) = E_k\{K_{xy}(i, i + 1)\lambda_z(i + 2) + K_{yz}(i + 1, i + 2)\lambda_x(i) + \\
-\lambda_x(i)\lambda_y(i + 1)\lambda_z(i + 2) + \\
K_{yx}(i, i + 1)\lambda_z(i - 1) + K_{yz}(i, i - 1)\lambda_x(i + 1) + \\
-\lambda_y(i)\lambda_x(i + 1)\lambda_z(i - 1)\}
$$

$$(C.7)$$

Notice that the $K_{xz}(i, i + 2)$ and $K_{xz}(i + 1, i - 1)$ next to nearest neighbor correlations which could be found in (C.6) are not in (C.7). In a similar fashion the further than nearest neighbor correlation terms can be eliminated from the dynamical equation of the nearest neighbor correlations. The model obtained this way considers only the nearest neighbor two-point correlations and neglects higher order correlations. (It was called "NNPC" referring to nearest neighbor pair correlation.)

At the end of this appendix we summarize the dynamical equations used to model an inner cell of a line with the "NNPC" approximation:

$$\hbar\frac{d}{dt}\hat{\vec{\lambda}}(i) = \hat{\Omega}_i\hat{\vec{\lambda}}(i) + E_k\begin{bmatrix} K_{zy}(i-1,i) + K_{yz}(i,i+1) \\ -K_{zx}(i-1,i) - K_{xz}(i,i+1) \\ 0 \end{bmatrix},\qquad\text{(C.8)}$$

$$\hbar\frac{d}{dt}\hat{K}(i,i+1) = \hat{\Omega}_{i+1}\hat{K}(i,i+1) - \hat{K}(i,i+1)\hat{\Omega}_i + E_k\hat{C}(i,i+1),\qquad\text{(C.9)}$$

$$\hat{C}(i,i+1) = \begin{bmatrix} 0 & 0 & \lambda_y(i) \\ 0 & 0 & -\lambda_x(i) \\ \lambda_y(i+1) & -\lambda_x(i+1) & 0 \end{bmatrix} + \qquad\text{(C.10)}$$

$$\langle\begin{bmatrix} \sigma_x(i)\sigma_y(i+1) & -\sigma_x(i)\sigma_x(i+1) & 0 \\ \sigma_y(i)\sigma_y(i+1) & -\sigma_y(i)\sigma_x(i+1) & 0 \\ \sigma_z(i)\sigma_y(i+1) & -\sigma_z(i)\sigma_x(i+1) & 0 \end{bmatrix}\sigma_z(i+2)\rangle +$$

$$\langle\begin{bmatrix} \sigma_y(i)\sigma_x(i+1) & -\sigma_x(i)\sigma_x(i+1) & 0 \\ \sigma_y(i)\sigma_y(i+1) & -\sigma_x(i)\sigma_y(i+1) & 0 \\ \sigma_y(i)\sigma_z(i+1) & -\sigma_x(i)\sigma_z(i+1) & 0 \end{bmatrix}^T\sigma_z(i-1)\rangle,$$

using the following approximation for the three-point correlations:

$$\begin{aligned} K_{abc}(i,i+1,i+2) = \langle\hat{\sigma}_a(i)\hat{\sigma}_b(i+1)\hat{\sigma}_c(i+2)\rangle &\approx K_{ab}(i,i+1)\lambda_c(i+2) + \\ &\quad K_{bc}(i,i+2)\lambda_a(i+1) - \\ &\quad \lambda_a(i)\lambda_b(i+1)\lambda_c(i+2), \\ &\quad a,b,c = x,y,z. \end{aligned}\qquad\text{(C.11)}$$

The "PC" equations can be summarized as

$$\hbar \frac{d}{dt} \hat{\vec{\lambda}}(i) = \hat{\Omega}_i \hat{\vec{\lambda}}(i) + E_k \begin{bmatrix} K_{zy}(i-1,i) + K_{yz}(i,i+1) \\ -K_{zx}(i-1,i) - K_{xz}(i,i+1) \\ 0 \end{bmatrix}, \tag{C.12}$$

$$\hbar \frac{d}{dt} \hat{K}(i,j) = \hat{\Omega}_j \hat{K}(i,j) - \hat{K}(i,j)\hat{\Omega}_i + E_k \hat{C}(i,j), \tag{C.13}$$

where for nearest neighbors ($j=i+1$)

$$\hat{C}(i,i+1) = \begin{bmatrix} 0 & 0 & \lambda_y(i) \\ 0 & 0 & -\lambda_x(i) \\ \lambda_y(i+1) & -\lambda_x(i+1) & 0 \end{bmatrix} + \tag{C.14}$$

$$\left\langle \begin{bmatrix} \sigma_x(i)\sigma_y(i+1) & -\sigma_x(i)\sigma_x(i+1) & 0 \\ \sigma_y(i)\sigma_y(i+1) & -\sigma_y(i)\sigma_x(i+1) & 0 \\ \sigma_z(i)\sigma_y(i+1) & -\sigma_z(i)\sigma_x(i+1) & 0 \end{bmatrix} \sigma_z(i+2) \right\rangle +$$

$$\left\langle \begin{bmatrix} \sigma_y(i)\sigma_x(i+1) & -\sigma_x(i)\sigma_x(i+1) & 0 \\ \sigma_y(i)\sigma_y(i+1) & -\sigma_x(i)\sigma_y(i+1) & 0 \\ \sigma_y(i)\sigma_z(i+1) & -\sigma_x(i)\sigma_z(i+1) & 0 \end{bmatrix}^T \sigma_z(i-1) \right\rangle,$$

and for further than nearest neighbors ($j>i+1$)

$$\hat{C}(i,j) = \left\langle \begin{bmatrix} \sigma_x(i)\sigma_y(j) & -\sigma_x(i)\sigma_x(j) & 0 \\ \sigma_y(i)\sigma_y(j) & -\sigma_y(i)\sigma_x(j) & 0 \\ \sigma_z(i)\sigma_y(j) & -\sigma_z(i)\sigma_x(j) & 0 \end{bmatrix} (\sigma_z(j-1) + \sigma_z(j+1)) \right\rangle + \tag{C.15}$$

$$\left\langle \begin{bmatrix} \sigma_y(i)\sigma_x(j) & -\sigma_x(i)\sigma_x(j) & 0 \\ \sigma_y(i)\sigma_y(j) & -\sigma_x(i)\sigma_y(j) & 0 \\ \sigma_y(i)\sigma_z(j) & -\sigma_x(i)\sigma_z(j) & 0 \end{bmatrix}^T (\sigma_z(i-1) + \sigma_z(i+1)) \right\rangle.$$

The following approximation for the three-point correlations is used:

$$K_{abc}(i,j,k) = \langle \hat{\sigma}_a(i)\hat{\sigma}_b(j)\hat{\sigma}_c(k) \rangle \approx K_{ab}(i,j)\lambda_c(k) + K_{bc}(i,k)\lambda_a(j) + \tag{C.16}$$

$$K_{ac}(i,k)\lambda_b(j) - 2\lambda_a(i)\lambda_b(j)\lambda_c(k),$$

$$a,b,c = x,y,z.$$

REFERENCES

QCA papers

[1] C. S. Lent, P. D. Tougaw, W. Porod and G. H. Bernstein, *Nanotechnolog*y **4**, 49 (1993).

[2] C. S. Lent, P. D. Tougaw, and W. Porod, *Appl. Phys. Lett.* **62**, 714 (1993).

[3] C. S. Lent and P. Douglas Tougaw, *J. Appl. Phys.* **74**, 6227 (1993).

[4] P. Douglas Tougaw and C. S. Lent, *J. Appl. Phys*. **75**, 1818 (1994).

[5] C. S. Lent and P. D. Tougaw, *J. Appl. Phys*. **75**, 4077 (1994).

[6] C. S. Lent, P. Tougaw and W. Porod, PhysComp '94: Proc. Workshop Phys. Comp. *(*IEEE Computer Society Press, 1994).

[7] C. S. Lent, P. Tougaw and W. Porod, J. Appl. Phys. **80,** 4722 (1996).

[8] C. S. Lent and P. D. Tougaw, *Proc. IEEE*, **85**, 541 (1997).

[9] G. Tóth, C. S. Lent, *J. Appl. Phy*s **85**, No. 5, 2977-2984(1999); cond-mat/0004457.

About the semiconductor realization

[10] G. Tóth, Yu. Brazhnik, unpublished.

[11] Y. Fu, M. Willander, *J. Appl. Phys*. **83**, 3186 (1998).

[12] I. I. Yakimenko, I. V. Zozoulenko, C.-K. Wang, K.-F. Berggen, *J. Appl. Phys.* **85**, 6571 (1999).

[13] H. Wu, D. W. L. Sprung, *J. Appl. Phys*. **84**, 4000 (1998).

[14] M. Governale, M. Macucci, G. Iannaccone, C. Ungarelli, J. Martonell, *J. Appl. Phys.* **85**, 2962 (1999).

Single Electronics Review

[15] Hermann Grabert and Michel H. Devoret, *Single Charge Tunneling, Coulomb Blockade Phenomena in Nanostructures* (Plenum Press, New York, 1992).

[16] D. K. Ferry, S. M. Goodnick, *Transport in Nanostructures* (Cambridge University Press, 1997).

[17] T. Dittrich, P. Hänggi, G.-L. Ingold, B. Kramer, G. Schön, W. Zweger, *Quantum Transport and Dissipation* (WILEY-VCH Verlag GmbH, Weinheim, Germany, 1998).

[18] K. K. Likharev, *IBM J. RES. Develop.* **32**, 144(1988).

Single Electronics Papers

[19] K. K. Likharev and A.N. Korotkov, *Science* **273**, 763(1996).

[20] K. K. Likharev, N. S. Bakhalov, G. S. Kazacha, and S. I. Serdyukova, *IEEE Trans. Magn.* **25**, 1436 (1989).

[21] D. V. Averin and A. A. Odinstov, *Phys. Letters A* **140**, 251(1989).

[22] D. V. Averin, and Yu. Nazarov, *Phys. Rev. Lett.* **65**, 2446(1990).

[23] D. V. Averin, A. N. Korotkov, K. K. Likharev, *Phys. Rev. B* **44**, 6199(1991).

[24] D. V. Averin, A. N. Korotkov, Yu. V. Nazarov, *Phys. Rev. B* **66**, 2818 (1991).

[25] P. Delsing, T. Claeson, K. K. Likharev, and L. S. Kuzmin, *Phys. Rev. B* **42**, 7439 (1990).

[26] P. Delsing, J.Pettersson, P. Wahlgren, D. B. Haviland, N. Rorsman, H. Zirath, P. Davidsson, and T. Claeson, *Proc. 1st Int. Symposium on Advanced Physical Fiel*ds, Tsukuba, Japan, 1996.

[27] P. Delsing, D. B. Haviland and P. Davidsson, *Czech J. Phys.* **46**, 2359 (1996).

[28] I. P. Kouwenhoven, N. C. van der Vaart, A. T. Johnson, W. Kool, C. J. P. M. Harmans, I. G. Williamson, A. A. M. Staring, and C. T. Foxon, Z. Phys. B **85**, 367 (1991).

[29] L. P. Kouwenhoven, A. T. Johnson, N.C. van der Vaart, A. van der Enden, and C. J. P. M. Harmans, *Phys. Rev. Lett.* **67**, 1626 (1991).

[30] L. J. Geerligs, D. V. Averin, and J E. Mooij, *Phys. Rev. Lett.* **65**, 3037 (1990).

[31] D. C. Glattli, C. Pasquier, U. Meirav, F. I. B. Williams, Y. Jin, and E. Etienne, *Z. Phys. B* **85**, 375 (1991).

[32] L. R. C. Fonseca, A. N. Korotkov, K. K. Likharev, and A. A. Odintsov, *J. Appl. Phys.* **78**, 5 (1995).

[33] F. Hofmann, T. Heinzel, D. A. Wharam, and J. P. Kotthaus, G. Böhm, W. Klein, G. Tränkle, and G. Weimann, *Phys. Rev. B*, **51**, 13872 (1995).

[34] H. Pothier, P. Lafrage, C. Urbina, D. Esteve, and M. H. Devoret, *Europhys. Lett.* **17**, 249 (1992).

[35] Shingo Katsumoto, Naokatsu Sano, and Shun-ichi Kobayashi, *Jpn. J. Appl. Phys.* **31**, 759 (1992).

[36] M. Matters, J. J. Versluys, and J. E. Mooij, *Phys. Rev. Lett.* **78**, 2469 (1997).

[37] K. A. Matsuoka, K. K. Likharev, P. Dresselhaus, L. Ji, S. Han, and J. Lukens, xxx.lanl.gov/archive/cond-mat/9609273.

[38] Sangchul Oh, Kyung Wan Park, Mincheol Shin, Seongjae Lee, and El-Hang Lee, Phys. Rev. B **57**, 2368 (1998).

[39] E. S. Snow, P. M. Campbell, R.W. Rendell, F. A. Buot, D. Park, C. R. K. Marrian and R. Magno, *Appl. Phys. Lett.* **72**, 3071(1998).

[40] Oriza Triznyák, *Példaképem: Mekk Elek*, Móra könyvkiadó, Budapest, 1995.

[41] MOSES 1.0, Monte-Carlo Single-Electronics Simulator, 1995, developed by Ruby Chen with contributions from A. M. Matsuoka, A. N. Korotkov, B. Harris, P. Shevchenko and K. K. Likharev, available from Rubi Chen, e-mail: rchen@max.physics.sunysb.edu.

[42] SIMON, Single Electron Device and Circuit Simulator, available from Dr. Christoph Wasshuber, http://home1.gte.net/kittypaw/simon.htm.

NOTRE DAME METAL-ISLAND QCA EXPERIMENTS AND RELATED PAPERS

[43] A. O. Orlov, I. Amlani, G. H. Bernstein, C. S. Lent and G. L. Snider, *Science* **277**, 928 (1997).

[44] A. O. Orlov, I. Amlani, G. Tóth, C. S. Lent, G. H. Bernstein and G. L. Snider, *Appl. Phys. Lett.* **73**, 2787 (1998).

[45] G. Tóth, A. Orlov, I. Amlani, C. S. Lent, G. H. Bernstein, G. L. Snider, *Phys. Rev. B* **60**, 16906-16912 (1999); cond-mat/9911173.

[46] T. A. Fulton and G.H. Dolan, *Phys. Rev. Lett.* **58**, 109 (1987).

[47] C. Livermore, C. H. Crouch, R. M. Westervelt, K. L. Campman and A. C. Gossard, *Science* **20**, 1332 (1996).

[48] G. L. Snider, A. O. Orlov, I. Amlani, G. H. Bernstein, C. S. Lent, J. L. Merz and W. Porod, *Solid State Electronics* **42**, 1335 (1998).

Misc. Remarks

[49] The experimental setup of Ref. 36 is similar to that of this paper. The major difference is that Ref. 21 examines the system in the Coulomb blockade regime when tunneling is suppressed and the current comes from co-tunneling, while the goal of our paper is to investigate the behavior of two capacitively coupled double-dots when the Coulomb blockade is lifted and the current is due to sequential correlated tunneling events.

[50] For a subsequent experimental setup the conductance lowering reached 50%. The computed transition frequency was 200 MHz.

[51] The actual electron temperature of the device is 70mK. This is due to extra heating of electron subsystem and commonly seen in transport experiment. To infer the temperature we used the method described in Single Electron Tunneling, edited by H. Gabert and M. H. Devoret (Plenum Press, NY 1992, Chapter 5, p. 181).

Quantum Cellular Neural Networks

[52] G. Tóth, C. S. Lent, P. D. Tougaw, Y. Brazhnik, W. Weng, W. Porod, R. Liu and Y. Huang, *Superlattices and Microstructures* **20**, 463 (1996); cond-mat/0005038.

Cellular Neural Networks

[53] L. O. Chua and L. Yang, *IEEE Trans. Circuits. Syst.* **35,**1257 and 1273 (1988).

[54] L. O. Chua and T. Roska, *IEEE Trans. Circuits. Syst.-I* **40**, 147 (1993).

[55] T. Roska and L. O. Chua, *IEEE Trans. Circuits. Syst.-II* **40**, 163 (1993).

[56] L. O. Chua, M. Hasler, G. Moschytz, J. Neirynck, I*EEE Trans. Circuits Syst.*, 1996.

Coherence Vector Formalism

[57] G. Mahler and V. A. Weberruβ, *Quantum Networks* (Springer, 2nd Edition, 1998).

Quantum Computing

[58] C. P. Williams and Scott H. Clearwater, *Explorations in Quantum Computing* (Springer, 1998).

[59] A. Steane, xxx.lanl.gov/archive/quant-ph/9708022.

[60] R. P. Feynman, *Int. J. Theoretical Phys.* **21**, 467 (1982).

[61] D. Deutsch, *Proc. R. Soc. Lond. A* **400**, 97 (1985).

[62] D. Deutsch, *Proc. R. Soc. Lond. A* **425**, 73 (1989).

[63] S. Lloyd, *Science* **261**, 1569 (1993).

[64] L. K. Grover, *Phys. Rev. Lett.* **79**, 325 (1997).

[65] D. P. DiVincenzo, *Phys. Rev. A* **51**,1015 (1995).

[66] D. P. DiVincenzo, *Nature* **393**,113 (1998).

[67] N. Gershenfeld and I. L. Chuang, *Scientific American*, 66 (June 1998).

[68] I. L. Chuang, N. Gershenfeld and M. Kubinec, *Phys. Rev. Lett.* **80**, 3408 (1998).

[69] I. L. Chuang, L. M. K. Vandersypen, X. Zhou, D. W. Leung and S. Loyd, *Nature* **393**, 143 (1998).

[70] B. E. Kane, *Nature* **393**,133 (1998).

[71] A. Barenco, D. Deutsch, A. Ekert, J, Jozsa, *Phys. Rev. Lett.* **74**, 4083 (1995).

[72] A. Barenco, B. Benett, R. Cleve, D. P. DiVincenzo, N. Margolus, P. Shor, T. Sleator, J. A. Smolin, H. Weinfurter, *Phys. Rev. A* **52**, 3457 (1995).

[73] A. Barenco, xxx.lanl.gov/archive/quant-ph/9505016.

[74] T. Sleator, Harald Weinfurther, *Phys. Rev. Lett.* **74**, 4087(1995).

[75] J. A. Jones, M. Mosca, and R. H. Hansen, *Nature* **393**, 344-346 (1998).

[76] R. Marx, A. F. Fahmy, J. M. Myers, W. Bermel, S. J. Glaser, xxx.lanl.gov/archive/ quant-ph/9905087.

[77] L. A. Openov, http://xxx.lanl.gov/archive/cond-mat/9906390.

[78] G. Burkhard, D. Loss, D. P. DiVincenzo, *Phys. Rev. B* **59**, 2070 (1999).

[79] P. Zanardi, F. Rossi, *Phys. Rev. Lett.* **81,** 4752 (1998).

[80] G. D. Sanders, K. W. Kim, W. C. Holton, *Phys. Rev. A* **60**, 4146 (1999).

[81] T. Tanamoto, http://xxx.lanl.gov/archive/quant-ph/990231.

[82] D. Loss, D. P. Vincenzo, *Phys. Rev. A* **57**, 120 (1998).

[83] P. Shor, "Algorithms for quantum computation: Discrete Logarithms and Factoring," *Proceedings 35th Annual Symposium on Foundations of Computer Science*, 124-134(1994),

[84] J. Cirac, P. Zoller, *Phys. Rev. Lett.* **74**, 4091(1995).

[85] Q. Turchette, C. Hood, W. Lange, H. Mabuchi, H. Kimble, *Phys. Rev. Lett.* **75**, 4710(1995).

[86] L. Grover, A Fast Quantum Mechanical Algorithm for Database Search, Proceedings of the 28th Annual ACM Symposium on the Theory of Computing, 212(1996).

[87] Y. Nakamura, YuA. Pashkin, J. S. Tsai, *Nature* **398**, 786(1999).

[88] L. B. Ioffe, V. B. Geshkenbein, M. V. Feigel'man, A. L. Fauchere, G. Blatter, *Nature* **398**, 679 (1999).

[89] Y. Makhlin, G. Schön, A. Shnirman, *Nature*. **398**, 305 (1999).

[90] A. Shnirman, G. Schön, *Phys. Rev. B* **57**, 15400 (1998).

[91] R. R. Ernst, G. Bodenhausen and A. Wokaun, *Principles of Nuclear Magnetic resonance in One and Two Dimension* (Clarendon Press, Oxford, 1987).

[92] G. Tóth, J. Timler and C. S. Lent, "Quantum Computing with Quantum-dot Cellular Automata using Coherence Vector Formalism" , *Proceedings of the IEEE International Workshop on Computational Electronics (IWCE-6)*, Osaka, 1998.